Doctorate Dissertation

博士論文

Provenance changes and depositional process of the sediments in the Yangtze Delta during the late Holocene: Application to reconstruct spatial pattern of summer precipitation in South China

（後期完新世における揚子江河口部堆積物の供給源変動と堆積プロセス：南中国における夏季降水分布復元の可能性）

A Dissertation Submitted for Degree of Doctor of Philosophy

02/2017

平成 29 年 2 月博士（理学）申請

Department of Earth and Planetary Science, Graduate School of Science,

The University of Tokyo

東京大学大学院理学系研究科地球惑星科学専攻

Keita Saito

齋藤　京太

Abstract

The Asian summer monsoon (ASM) controls the climate over Asia and strongly influence the hydrological cycle there. The East Asian summer monsoon (EASM) is one of the important components of the ASM and characterized by a seasonally northwest-southeastward migrating precipitation front. It exerts a significant influence on the East China especially, because the most part of annual precipitation there is brought by the EASM.

Since it could bring the flood and drought hazards in addition to the annual precipitation, it is important to understand the behavior of the EASM, and reconstruction of the paleo-monsoon behavior is necessarily to understand the long-term variability of the EASM. According to the meteorological observation during the late 20th century, change in the intensity of the EASM, which represents the strength of atmospheric circulation over the East Asia, is accompanied by changes in the position of the rain front. So, it is effective to reconstruct changes in the distribution of paleo-precipitation, in order to reconstruct the pale-monsoon intensity

The Yangtze River drains a large part of the South China and is one of the largest river in the world in respect both of the water discharge and its drainage area. Precipitation in the Yangtze drainage basin is significantly affected by the EASM and the changes in the

EASM intensity are reflected in the distribution of the precipitation in its drainage basin. Namely, when the EASM becomes stronger, the precipitation front penetrates to the northwestern part of the Yangtze drainage basin, whereas when the EASM becomes weaker, the precipitation front remains in the southeastern part of its drainage basin. Since there are positive correlations among the precipitation, water discharge, and sediment discharge, respectively, the sediments derived from the heavy precipitation area in the Yangtze drainage basin should occupy a large part of the sediments discharged from the Yangtze rivermouth. Thus, the reconstruction of provenance of sediments at the Yangtze rivermouth should enable me to reconstruct the past changes in the heavy precipitation area in the Yangtze drainage basin.

In Part 1 of this study, I established proxies for distinguishing sediments from the different area of the Yangtze River basin, because proxies are necessary in order to reconstruct past changes in the provenance of sediments at the Yangtze rivermouth, The electron spin resonance (ESR) signal intensity and crystallinity index (CI) of quartz are used as proxies, because quartz is the most common mineral among detrital materials and is resistant to physical and chemical weathering. The ESR signal intensity of quartz increases with the age when the mineral was formed, whereas CI reflects the process of the mineral forming. To reveal the characteristic of sediments discharged from individual area of the Yangtze

drainage basin, riverbed sediments were collected at the site along the mainstream and major tributaries of the Yangtze River. The ESR signal intensity and CI of the riverbed sediments show distinct difference among the groups of major tributaries; the upper Jinshajiang, western tributaries, northern tributaries, and southeastern tributaries. Especially, the ESR signal intensity of the tributaries tend to increase southeastward, from 0 of the western tributaries to 20 of the southeastern tributaries.

The effectiveness of the ESR signal intensity as the proxy to distinguish the provenance of sediments within the Yangtze drainage basin was verified by two steps. First, the ESR signal intensity below the junction with specific tributary were predicted using the sediment budget and the analyzed ESR signal intensity of the mainstream and tributary above the junction. The predicted ESR signal intensity at the every junction with the major tributaries were consistent with the analyzed ESR signal intensity of riverbed sediments at the corresponding site, indicating that the ESR signal intensity properly reflect the mixing ratio of the sediments. Second, using the similar calculations, the change of the ESR signal intensity along the mainstream was predicted using the sediment budget within the Yangtze drainage basin. Comparing the predicted and analyzed ESR signal intensity at the every junction with the major tributaries, the predicted values dropped within the error of the analyzed values, showing that it is possible to predict the

ESR signal intensity at the rivermouth based on the sediment budget in the drainage basin.

In Part 2 of this study, I tried to reconstruct history of the provenance changes for the sediments at the Yangtze rivermouth during the middle to late Holocene. To attain this objective, drilling was conducted at the subaqueous Yangtze Delta, and cores were recovered at YD13 site in July 2013 at the depth around 35 m. YD13 cores are mainly composed of silt to sandy silt and many coarse-silt to sand layers are detected by the Soft-X ray radio photographs. These coarse-silt to sand layers are used for the definition of the lithological units. Correlation among the different holes of YD13 are established based on correlations of the lithological units and the occurrence of coarse-silt to sand layers ,which was supplemented by the vertical variation pattern of water content. The sediments of YD13 sediments during the last 6 ky were categorized into three sedimentary unit based on the frequency and structure of the coarse–silt to sand layers; namely, Unit 3 deposited before 5.1 ka, Unit 2 deposited during 5.1 to 2.3 ka, and Unit 1 deposited after 2.3 ka.

The age model of YD13 was established on the basis of the radiocarbon dating of shell fossils, which revealed that the top 10 m of YD13 cores corresponds to the last 5.1 ky. In addition, the radiocarbon dating of the benthic foraminifera was carried out and compared with the OSL dating of quartz in the fine–silt fraction by Sugisaki et al. (2015). Both in

Unit 2 and 1, the foraminifera and OSL of quartz showed older ages compared to all of the shell fossils, indicating the contribution from the reworked sediments. In Unit 2, judging from the ages of foraminifera, the source of the reworked sediments were estimated to be the late transgressive system tract which were originally deposited during 1.2–0.7 ka during the continuous rise of sea level. The contribution ratio of the reworked sediments were estimated under the assumption that the radiocarbon ages of shell fossils, radiocarbon ages of foraminifera, and OSL ages of quartz in the fine–silt fraction represent the age of the riverine sediments, the reworked materials, and the mixture of the former two materials, respectively. The results revealed that 20–70 % of sediments in Unit 2 are the reworked materials. On the other hand, the source of the reworked materials in Unit 1 was estimated as either of the Jiangsu coastal sediments or the late transgression system tract same as Unit 2. In the same calculation as Unit 2, the contribution of the reworked materials in Unit1 was also estimated, and the results revealed that up to 40 % of sediments in Unit 1 are the reworked materials.

In order to reveal the millennial changes in the provenance of sediments at the Yangtze rivermouth, the ESR signal intensity and CI of the background sediments, which exclude the coarse–silt and sand layers, were analyzed for the last 5.1 ka. The ESR signal intensity and CI effected by the reworked materials are corrected using the estimated contribution

ratios. The temporal changes of the ESR signal intensity and CI values in the background sediments revealed that the contribution from the southeastern area was larger compared to that observed during the late 20th century during intervals from 5.1 to 4.1, 2.3 to 2.1, 1.2–1.0, and 0.7–0.2 ka, suggesting that the precipitation front remained within the southeastern area of the Yangtze basin during these intervals. On the other hand, the contribution from the northwestern area was comparable with that observed during the late 20th century intervals from 4.1 to 2.3 and 2.0 to 1.3 ka, indicating that the precipitation front penetrated into the northwestern area of the Yangtze basin during these intervals. These results indicate the millennial–scale fluctuations of monsoon intensity during the middle to late Holocene, under the assumption that the position of the precipitation front reflects the intensity of the EASM.

In addition to the background sediments, the ESR signal intensity, CI value, and frequency of the coarse-silt to sand layers, which were assumed to represent the occurrence of floods within the Yangtze basin, were also examined. The ESR signal intensity of the flood layers tend to be comparable with those of the background sediments except in the period from 2.0 to 1.3 ka.

Contents

General introduction

The Asian summer monsoon (ASM) controls the climate over Asia and strongly influence on the hydrological cycle there. The East Asian summer monsoon (EASM) is one of the important components of the ASM and characterized by a seasonally migrating precipitation front. It exerts a significant influence on the water resources in the East China, because the most part of annual precipitation there is brought by the EASM. In addition, the migration of precipitation front could induce floods and droughts, which strongly influence on the human activities. Although there were observational records since the late 20th century, it is important to reconstruct the paleo-monsoon fluctuation and its impact on human activities to understand the centennial to millennial behavior of the EASM.

Based on the meteorological observation after the late 20th century, the intensity EASM has been defined by the intensity of convection, the atmospheric pressure gradient at the representative points, the intensity of wind speed, and so on (Wang et al., 2008; Ding et al., 2008; Zhang et al., 2008). Since the monsoon is driven by the heat contrast between the continent and ocean, these indexes basically represent the strength of circulation over the East Asia. In the late 20th century, it is found that the circulation over the East Asia became weaker since mid-1970s, equal to the weakening of the EASM (Ding et al., 2008;

Zhang et al., 2008). This weakening of circulation was accompanied with the southward migration of the position of upward atmospheric current, followed by the synchronous migration of the precipitation front (Ding et al., 2008). Thus, the position of the precipitation front could be a useful index of the intensity of EASM.

The intensity of EASM through the Holocene has been studied during the last few decades (e.g. An et al., 2000; Dykoski et al., 2005; Wang et al., 2008; Zhang et al., 2011). Since the data on the strength of the atmospheric circulation were not available before the meteorological observation period, the proxies which were assumed to represent the amount of precipitation have been used as the proxy of the paleo-monsoon intensity such as the oxygen isotope in the stalagmites and lake sediments, the carbon isotope in peats, and tree-rings. However, it is now pointed out that the oxygen isotope ratio of the stalagmites and lake sediments, which were mainly used, do not necessarily represent the paleo-precipitation but that they may likely represent changes in the source of water vapors (Maher et al., 2012; Wang et al., 2012). Other proxies could also indicate the effects of local precipitation.

The Yangtze drainage basin drains a large part of the South China, where the most of the annual precipitation is brought by the EASM (Ding et al., 2008). In addition, the migration of the precipitation front since the late 20th century shows that the position of

the precipitation front within the Yangtze drainage basin is sensitive to the intensity of the EASM. Namely, the precipitation front was located around the northwestern part of the Yangtze drainage basin when the EASM became stronger, whereas the precipitation front was located around the southeastern part when the EASM became weaker (e.g. Zhang et al., 2008; Ding et al., 2008). Since there are positive relationship among the precipitation, water discharge, and sediment discharge in the Yangtze drainage basin (Chen et al., 2001; Xu et al., 2010), the sediment discharge from the area where the precipitation front is located should increase. Those sediments from heavy precipitation area are expect to occupy the larger contribution ratio in sediments at the Yangtze rivermouth, where majority of sediments from the whole drainage basin were deposited (Li et al., 2007). Thus, the reconstruction of provenance changes of sediments at the Yangtze rivermouth in the past should reveal migration history of the precipitation front in the Yangtze drainage basin.

So, the final objective of this thesis is to reconstruct the intensity of the EASM through changes in the position of the precipitation front during the last 5 ka. In Part 1 of this study, the proxies to distinguish the sediment provenance within the Yangtze drainage basin are established. Next in Part 2, reconstruction of provenance changes of the sediments at the Yangtze rivermouth is attempted by applying the proxies which are

established in Part 1 for the core sediments recovered from the subaqueous Yangtze delta.

Chapter 1: ESR signal intensity of quartz in the fine-silt fraction of the riverbed sediments of the Yangtze River: a provenance tracer for suspended particle matter

1.1 Introduction

The Yangtze River is the longest river in Asia, with a length of more than 6300 km and a drainage area of 1.81×10^6 km^2 (Hu et al. 2009). Its water discharge is 910 km^3/yr, which is fifth the largest in the world (Yang et al. 2002). More than 400 million people live in its drainage basin, and many large cities are situated along its mainstream (Zong and Chen 2000). According to historical records of the area during the last 2000 years, large floods that occurred more than 200 times severely affected the economy and lives of people in that region (Dai et al. 2010). Since its drainage basin occupies main part of South China, which is under a temperate climate, more than 60% of the total precipitation within the drainage basin is discharged through the Yangtze River (Xu et al. 2010). Also, a positive correlation exists between annual or monthly precipitation and the water discharge of the Yangtze River (Xu et al. 2010). The water discharge of the Yangtze River during summer accounts for 71 % of its annual water discharge (Chen et al. 2001). Since precipitation in the Yangtze drainage basin is affected by East Asian Summer Monsoon (EASM) in its

middle to lower part of the Yangtze River basin, while summer precipitation in the uppermost part of the Yangtze River basin is sourced from Indian Summer Monsoon (ISM) whose front position is connected to the EASM front (Wang and Lin 2002), it is reasonable to consider that water discharge of the Yangtze River during summer reflects the amount of precipitation brought by these monsoons. EASM is characterized by a seasonal northwestward migration of its precipitation front, and the timing and extent of its migration is associated with the migration of the westerly jet axis (Tada et al. 2016). Zhang et al. (2008) reported that inter-annual changes in the intensity of EASM, which is defined as the strength of northward wind around China, are associated with spatial changes in the high-precipitation area, with its northwestward penetration occurring during the time of stronger EASM convection. Thus, it is important to reconstruct the past spatio-temporal changes in the heavy precipitation and flood-causing areas within the Yangtze drainage basin to understand the long-term behavior of EASM and ISM.

Suspended particle matter (SPM) occupies more than 95% of the sediments discharged from the Yangtze River (Chen et al. 2001). Because the water discharge of the Yangtze River reflects precipitation in the drainage basin (Xu et al. 2010), and a strong positive relationship exists between its water discharge and sediment load (Chen et al. 2001), it is reasonable to consider that changes in SPM provenance reflect changes in the high-

precipitation area. Therefore, the changes of the provenance in the sedimentary records at the Yangtze rivermouth could enable me to specify the spatio-temporal variabilities of the heavy-precipitation area within the Yangtze drainage basin. Application of such technique to the sediment archives collected from an area immediately outside the rivermouth is my ultimate goal.

To specify the provenance of SPM, I analyze the electron spin resonance (ESR) signal intensity and the crystallinity index (CI) of detrital quartz in three size fractions of riverbed sediments: 4–16 μm, 16–63 μm, and >63 μm, respectively. ESR signal intensity and CI values have been used to distinguish the sources of sediments such as eolian dusts from various deserts in western China (e.g. Sun et al. 2007; Nagashima et al. 2007). I focus on quartz because it is the most common mineral in detrital materials and it is resistant to physical and chemical weathering. Moreover, its specific gravity is close to the average of detrital materials; thus, the size-sorting effect is minimal. The objectives of this chapter are i) to characterize quartz in the sediments discharged from each tributary based on ESR signal intensity and CI values, and ii) to test whether the relative contribution of detrital material derived from different tributaries is properly reflected in the ESR signal intensity and CI values of quartz in the sediments deposited along the mainstream and discharged from the rivermouth.

1.1.1 Geographical setting

The Yangtze River is the largest river in Asia. Its headwater region lies in the Tibetan Plateau at an altitude in excess of 6000 m, and it runs through the Sichuan Basin, Three Gorges, and Jianghan Plain before draining into the East China Sea. In this chapter, I use a modified definition of Chen et al. (2001) to subdivide the mainstream of the Yangtze into four parts including the uppermost, upper, middle, and lower parts (Figure 1.1).

The uppermost part is defined as the mainstream between the headwater and Yibin, the latter of which is located at the entrance of the Sichuan Basin. The uppermost part is a major contributor of SPM to the Yangtze River and is characterized by a steeper slope of the riverbed and deep and steep valleys (Yang et al. 2006). The length of the uppermost part is approximately 3100 km (Liu et al. 2011; Wu et al. 2009), and its drainage area is 4.6×10^5 km^2 (Hu et al. 2009), occupying 25% of the entire drainage basin of the Yangtze River. The difference in altitude from the headwater to the outlet of the uppermost part is more than 4000 m (USGS 2004), and the average riverbed slope is calculated as more than 1‰. The depth of the valley sometimes reaches 2000 m. A major tributary, the Yalongjiang, flows into the mainstream from the north at the lower part of the uppermost part (Figure 1.1). The “Big Bend” in Yunnan Province is situated where the mainstream

turns from southeastward to northeastward (Figure 1.1).

The upper part, or the Chuanjiang, is defined as the mainstream between Yibin and Yichang, the latter of which is located just below the outlet of the Three Gorges. In the upper part, the mainstream runs through the southern part of the Sichuan Basin, then cuts into the Three Gorges (Figure 1.1). The length of the upper part is approximately 800 km, and its own drainage area is 5.2×10^5 km^2 (Hu et al. 2009), occupying 29% of the entire drainage basin of the Yangtze River. In the Sichuan Basin, the riverbed slope is about 0.1–0.2‰, and the depth of valley is 200–300 m; both are smaller than those in the uppermost part. In the Three Gorges, the riverbed slope and valley depth increase to 0.4‰ and 1000 m at the maximum, respectively (Chen et al. 2001; USGS 2004). The channel width in the upper part is 0.5–1.5 km, and its water depth is 5–20 m (Chen et al. 2001). In the Sichuan Basin part of the upper part, two major tributaries, the Minjiang and Jialingjiang, flow into the mainstream from the north, and one major tributary, the Wujiang, flows in from the south. Construction of the Three Gorges Dam (TGD) was completed in 2003 on the mainstream at the outlet of the Three Gorges to the upstream of Yichang.

The middle part, or the middle Yangtze, is defined as the mainstream between Yichang and Hukou, the latter of which is located just downstream of the Poyang Lake outlet. The length of the middle part is 950 km, and its own drainage area is 6.8×10^5 km^2, occupying

38% of the entire drainage basin of the Yangtze River (Chen et al. 2001). Running through Jianghan Plain, the mainstream is characterized by 10 km-scale meandering; the area includes many lakes that originated from old channels. The riverbed slope of the mainstream dramatically decreases to 0.02–0.03 ‰, and the channel widens to 1–2 km with a depth of 6-15 m (Chen et al. 2001). Three major tributaries flow into the mainstream in the middle part; the Hanjiang from the north and Dongting and Poyang lakes from the south (Figure 1.1). Dongting Lake has its own drainage area of 2.7×10^5 km^2 (Hayashi et al. 2008), gathering waters from four major tributaries. In addition, three natural channels flow from the mainstream into Dongting Lake and are known as "Three Channels" or "Three Outlets" (Dai et al. 2005; Yin et al. 2007). Parts of water and SPM in the upper part of the mainstream flow into Dongting Lake through these three channels (Dai et al. 2005). Poyang Lake has a drainage area of 1.6×10^5 km^2, and its largest tributary is the Ganjiang (Hu et al. 2007).

The lower part, or the lower Yangtze, is defined as the mainstream between Hukou and the rivermouth. Its length is 930 km, and its own drainage area is 1.2×10^5 km^2 (Chen et al. 2001), occupying 7% of the entire drainage basin of the Yangtze River. The mainstream in this part runs through flat plains and low hills and is characterized by many braid bars (Chen et al. 2001). The riverbed slope of the mainstream decreases further to

0.01‰, and the channel width widens to 2–4 km on average, reaching 15 km in the estuary region. The channel depth also increases to 10–20 m (Chen et al. 2001). Although many lakes are situated near the mainstream, no large tributary exists in the lower part.

1.1.2 Geological setting

A geological map within the Yangtze drainage basin is shown in Figure 1.2.

In the headwater region of the uppermost Yangtze drainage basin, the mainstream flows through the Northern Qamdo Block, which is composed mainly of Triassic–Jurassic shallow marine carbonate rocks, basaltic rocks, and fluvial sedimentary rocks (Yin and Harrison 2000; Xia et al. 2011). The mainstream then flows into the Songpan-Garze terrane, which is composed of Triassic turbiditic sedimentary rocks that were deposited in the Paleo-Tethys Ocean and folded during the Late Triassic (Roger et al. 2008; Enkelmann et al. 2007). The major tributary, the Yalongjiang, also flows mainly through the Songpan-Garze terrane. The southwestern part of the uppermost Yangtze drainage basin, where the Jinshajiang flows southward parallel with the Lancanjiang (Mekong River) and Nujiang (Salween River), includes Paleozoic carbonates, mafic volcanics, and Permian to Paleogene shale and sandstones (Reid et al. 2005a). In the lower part of the uppermost basin below Big Bend, Permian to Triassic mafic igneous rocks known as the

Emeishan Large Igneous Province are distributed extensively in association with Jurassic sandstones and mudstones (Ali et al. 2005; Liu et al. 2011).

The northwestern part of the upper Yangtze drainage basin, where the Daduhe (the largest tributary of the Minjiang; Figure 1.1) drains, also belongs to the Songpan-Garze terrane and is composed mainly of Triassic turbiditic rocks that are partly intruded by Late Triassic or Early Jurassic granites (Reid et al. 2005a; Roger et al. 2008). The upper part of the Jialingjiang drainage basin belongs to the South Qinling orogenic belt, consisting of Meso–Neoproterozoic basements that were weakly metamorphosed during the Neoproterozoic, shallow-marine deposits of Neoproterozoic–Devonian age, and Triassic granitoids (Meng and Zhang, 2000; Qin et al. 2010; Dong et al. 2011). The central to southeastern Sichuan Basin, where the middle to lower part of the Jialingjiang and the lower part of the Wujiang drain, is widely covered by thick terrestrial mudstone and sandstone deposited during the Jurassic–Cretaceous (Hao et al. 2008; Ma et al. 2008). In the upper part of the Wujiang drainage basin, Permian–Triassic limestones and dolomitic limestones with minor basalts are exposed. Cambrian and Ordovician carbonate rocks and Silurian sandstones are exposed mainly in the lower part of this basin (Han et al. 2004; Wang et al. 2010).

In the middle Yangtze drainage basin, Quaternary sediments carried by the Yangtze are

widely deposited along the mainstream, particularly in Jianghan Plain situated between the mainstream and the Hanjiang. The upper part of the Hanjiang drainage basin belongs to the Qinling orogenic belt and is composed of Neoproterozoic basements and Neoproterozoic–Devonian sediments (Qin et al. 2010). Quaternary loess are also deposited in some part of the upper Hanjiang drainage basin (Zhang et al. 2012). The middle to lower part of the Hanjiang drainage basin belongs to Jianghan Plain. Most parts of the Dongting Lake drainage basin belong to the eastern part of Yangtze Block. The Proterozoic basement of Yangtze Block exhibits evidence of low-grade metamorphism. Cambrian and Ordovician carbonate rocks, Devonian sandstone and shale, and Cretaceous red-colored sandstone are mainly exposed in this region (Chen and Jahn 1998; Wang et al. 2010; Wang et al. 2013). The drainage basin of Poyang Lake and the easternmost part of the Dongting Lake drainage basin belong to Cathaysia Block, which is composed of Neoproterozoic conglomerate and sandstone, lower Paleozoic siliciclastics, Jurassic granites, and Cretaceous red-colored sandstone (Wang et al. 2007a; Wang et al. 2013).

In the lower Yangtze drainage basin, Quaternary sediments derived from the upper and middle Yangtze were deposited along the mainstream. The southern part of the lower Yangtze drainage basin belongs to the Cathaysia Block (Wang et al. 2007a; Wang et al.

2013).

In summary, the bedrock of the uppermost and upper Yangtze drainage basin are relatively young and are composed mainly of Mesozoic strata; the northernmost and southern parts of the upper Yangtze drainage basin are composed mainly of Paleozoic strata; and the middle and lower Yangtze drainage basins are composed mainly of Paleozoic–Proterozoic strata (Figure 1.2). Thus, the strata within the Yangtze drainage basin have a trend of increasing age toward downstream. As to the rock types, sedimentary and low-grade metasedimentary rocks are exposed mainly in the uppermost and upper parts, whereas crystalline plutonic rocks are more common in the middle and lower parts.

1.1.3 Hydrological setting

In the Yangtze, hydrological observation of its water discharge and sediment load began in the 1870s and 1950s, respectively (Chen et al. 2001). Measurements of its water flow speed and cross-sectional area are conducted daily by ships at major gauge stations along the mainstream and major tributaries (Wang et al. 2007b; Hassan et al. 2010). At each station, the sediment load is calculated as a product of suspended sediment concentration and water discharge daily, used as a basis of the monthly to annual sediment load (Yang et al. 2006). Figure 1.3 shows the annual sediment budget for the entire drainage basin

averaged during 1950–2002, before the operation of TGD, whereas Figure 1.4 shows that for 2003-2012, after its operation began (Dai et al. 2005; Hu et al. 2009; Yang et al. 2006; Yang et al. 2014).

Dongting Lake, which drains into the middle part of the mainstream, has played an important role in the sediment budget of the Yangtze (Dai et al. 2005). In particular, below the Three Gorges, turbid water from the upper part flows not only into the mainstream of the Yangtze but into channels flowing into Dongting Lake known as Three Outlets (Dai et al. 2005; Yin et al. 2007). Therefore, Dongting Lake receives part of the sediments from the mainstream above the Three Gorges through Three Outlets in addition to those originating from its own tributaries. Thus, the sediments discharged from Dongting Lake to the mainstream are a mixture of sediments from the upper part of the mainstream and from tributaries of Dongting Lake itself. According to the sediment budget based on observational data, the volume of sediments accumulated in Dongting Lake is proportional to the inflow amount from Three Outlets; 87% of sediments from Three Outlets are estimated to have been deposited within the Dongting Lake area during 1950–2002 (Dai et al. 2005).

Since the 1950s, when observation of sediment load began, the sediment discharge from the mainstream at Datong has shown a decreasing trend owing to the reservoir

construction and the national soil conservation project, particularly in the Jialingjiang drainage basin (Yang et al. 2006; Hu et al. 2011). Moreover, the operation of TGD in 2003 significantly changed the sediment budget of the mainstream below it (Figure s. 3 and 4). Before TGD operation began, the total sediment input into the Three Gorges area was 489 Mt/yr, which is nearly balanced with the sediment load of 492 Mt/yr at Yichang (Yang et al. 2007). However, since the operation of TGD, 80.3% (188 Mt/yr) of the sediments input into the Three Gorges area (234 Mt/yr) have become trapped within the TGD (Yang et al. 2014). The sediment budget in the middle and lower parts were also changed after 2003 because the sediment load from the upper part to the middle and lower parts decreased due to TGD construction (Chang et al. 2010). Specifically, erosion of 63 Mt/yr occurred in the middle and lower parts since the TGD operation, while the net sediment accumulation of 36.1 Mt/yr occurred before 2003, prior to its operation (Dai et al. 2005; Yang et al. 2014). In 2010s, more than ten hydropower reservoirs in the uppermost part have been proposed. Five dams were constructed by 2012 including the Xiangjiaba and Xiluodu dams between Yibin and its junction with the Yalongjiang, and the Longkaikou, Jiangqiao, and Ahai dams between the junction with the Yalongjiang and Big Bend (Hennig et al. 2013). At least the Jiangqiao Dam began operation prior to 2010 and the other dams began their construction in the early 2010s. These dams are expected to

influence the sediment budget in the uppermost Yangtze in the near future.

1.2 Methods

1.2.1 Samples

Riverbed sediments were sampled mainly from the riverside of the mainstream and major tributaries of the Yangtze River in July and September 2011 and in February and October 2012. Sediments from the mainstream were sampled at locations a few hundred meters to a few kilometers above and below the junctions with major tributaries in order to evaluate the effect of sediment mixing between the mainstream and these major tributaries. Sediment from the tributaries were sampled at locations several kilometers upstream of the junction with the mainstream so as to prevent contamination of sediments from the mainstream. According to the observation, SPM consists of fine-silt particles with the mean diameter of about 10 μm in the lower part throughout the year (Hassan et al. 2010; Mao et al. 2011). Furthermore, SPM accounts for 98% of the sediment discharge from the Yangtze rivermouth (Yang et al. 2002). For these reasons, I sampled silty sediments when possible; otherwise, sandy sediments were sampled.

Additionally, I also analyzed three SPM samples (JSJ-GLS, JSJ110701, and YZ110703-03) taken at the same locations on the same days as riverbed samples were taken. Then, I

examined if the fine-silt fraction of riverbed samples could represent the SPM.

1.2.2 Sample preparation

Samples were pretreated prior to grain size separation, based on the method in Rea and Janecek (1981) and Tada et al. (2000). Approximately 3 g of a dry sample was placed into two plastic centrifuge tubes. As the first step, carbonates were removed by soaking in 50 ml of 20% acetic acid at room temperature for 8 h. After removing carbonates, the supernatants were drained. Approximately 50 ml of deionized water was added, and the tubes were centrifuged twice at 3000 rpm to remove any remaining acetic acid. As the second step, organic matter was removed by soaking in approximately 50 ml of 10% hydrogen peroxide at 60 °C for more than 20 h until the bubbling ceased. After the supernatants were drained, approximately 50 ml of deionized water was added, and the tubes were centrifuged twice at 3000 rpm. As the third step, Fe and Mn oxides were removed by using a mixture of 0.3 mol/l sodium citric acid and 0.1 mol/l sodium hydrogen carbonate at a ratio of 8:1. Three grams of sodium hydrosulfite was then added. The tubes were heated at 80 °C for 8 h. Then, the supernatants were removed, 50 ml of deionized water was added, and the tubes were centrifuged twice.

These pretreated samples were kept wet before grain size separation. Grain size separation

of pre-treated samples was conducted by the settling method based on Stokes' law at 4 μm and 16 μm. Separation at 63 μm for the fraction of > 16 μm was also conducted using a sieve. Although I did not sieve the upper limit of >63 μm fraction, the grain size in the sand fraction are 2–3 mm at largest based on macroscopic observation. The riverbed sediments were grain-separated into four size fractions of <4 μm (clay), 4–16 μm (fine-silt), 16–63 μm (coarse-silt), and >63 μm (sand); the latter three fractions were subject to analysis. The SPM samples were grain-separated into two size fractions, <4 μm and >4 μm, and the latter was analyzed. The <4 μm (clay) fraction was not analyzed neither for the riverbed sediments nor SPM. After the separation procedures were completed, each fraction was dried and weighed.

1.2.3 ESR analysis

In this chapter, ESR signal intensity of quartz was used to constrain the provenance of quartz in the sediments. ESR signal intensity of the E_1' center of quartz reflects the amount of unpaired electrons accompanied by oxygen vacancy (Feigl et al. 1974; Toyoda and Naruse 2002). Since these oxygen vacancies in quartz are formed mainly by natural radiation of radioactive elements contained in the host rock, ESR signal intensity increases with an increase in age of the host rock (Toyoda and Naruse 2002). A typical

peak of the E1’ center measured by an ESR spectrometer is shown in Figure 1.5(a).

Because quartz is the most common mineral in detrital materials and it is resistant to physical and chemical weathering, it is easy to adopt the ESR signal intensity of quartz as the proxy of detrital grains. In addition, the ESR signal intensity is adoptable to the silt-sized grains, which require short time scale to be transported compared to the sand-sized grains, Thus, it is appropriate to apply the ESR signal intensity of quartz for the river sediments to reveal changes in a short time scale.

Prior to ESR signal intensity measurement, the grain-size separated and dried samples were irradiated by 2.5 kGy ^{60}Co γ-ray under room temperature at Takasaki Advanced Radiation Research Institute, National Institutes for Quantum and Radiological Science and Technology to produce electron holes according to the method of Toyoda and Hattori (2000). Then, samples of approximately 0.1 g were heated at 300 °C for 15 min to convert the oxygen vacancy of quartz to the E_1' center. ESR measurement was conducted by using an ESR spectrometer (FA-100, JEOL) at the Department of Earth and Planetary Science, University of Tokyo. The measurement conditions include 0.01 mW of microwave strength, 5 × 1 mT of measurement range, 2 min of measurement time at room temperature, and sample weight of 0.1 ± 0.001 g. ESR signal intensity of the bulk sample was normalized by the weight percent of quartz in a sample to obtain ESR signal intensity

of the quartz, whose unit is 1.3×10^{15} spins/g (Toyoda and Hattori 2000).

ESR signal intensity is calculated by normalizing the peak height of E_1' center of the sample by the weight of quartz in the sample and the standard as shown in the formula below.

$P_{sample} = PH_{E1', sample} / (W_{sample} * C_{sample} * PH_{Mn, sample})$

$P_{std} = PH_{E1', std} / (W_{std} * C_{std} * PH_{Mn, std})$

ESR signal intensity = $(P_{sample} / P_{std}) * F$

Where $PH_{E1'}$ is the peak height of E_1' center of quartz measured by an ESR spectrometer, W is weight of the sample, C is the quartz content measured by the XRD (described latter section in detail), PH_{Mn} is the peak height of Mn center of quartz measured by an ESR spectrometer, and F is a constant value for an individual spectrometer. The suffix of $_{sample}$ and $_{std}$ indicated the measured sample and the standard sample. The peak height of E_1' center of quartz is indicated in Figure 1.5(a).

To evaluate reproducibility of ESR signal intensity,I selected two γ-ray irradiated samples (the fine-silt fraction of YZ1210-4 and YZ110703-04m2), split each into three sub-samples, packed each sub-sample into a discrete holders, and measured their ESR signal intensity of quartz. Then, the standard error (95 %) for each sample were calculated based on 3 times measurements for 3 subsamples (= 9 measurements in total). Reproducibility

of ESR signal intensity of the two γ-ray irradiated samples are 1.3 for YZ110703-04m2 and 3.0 for YZ1210-4, respectively. I adopt the average of these standard error, 2.2 as the reproducibility of ESR signal intensity in this thesis.

1.2.4 X-Ray powder diffraction analysis

The quartz content (QC) was determined by using X-ray power diffraction (XRD) to calculate ESR signal intensity of quartz. CI was also determined by XRD to correct the crystallinity effect on the quartz peak height. CI is an index of the degree of crystallization of quartz, which reflects the condition of crystallization such as cooling speed or crystallization temperature (Murata and Norman 1976). CI values were calculated as the degree of quartz peak split at 67.74°2θ based on the definition of Murata and Norman (1976) (Figure 1.5(b)). CI was also used to constrain the provenance of the quartz. Prior to XRD measurement, two fractions, 16–63 μm and >63 μm, were ground by using an agate mortar for about 15 min. Since samples of the fine-silt fraction (4–16 μm) were regarded to be small enough for XRD analysis, they were not grounded. To measure QC, 10.0 wt% of silicon powder was added to the samples as an internal standard. XRD measurement (X'pert Plus, PANalitical) was conducted at Department of Earth and Planetary Science, the University of Tokyo. XRD measurements were repeated three

times with repacking, conducted each time by using CuKα X-ray, 45 kV of voltage, and 40 mA of current, and result were averaged for each sample. The divergence and anti-scatter slits were 1.52 mm and 3 mm in width, respectively. The measurement ranges were 20–30°2θ for QC and 66–71°2θ for CI. QC was calculated by the ratio of the silicon and quartz peak heights at 27.9°2θ and 20.9°2θ, respectively. QC was also corrected for the effect of crystallinity based on Isozaki (2009).

Reproducibility of CI values was evaluated for two γ-ray irradiated samples (the fine-silt fraction of YZ1210-4 and YZ110703-04m2). I took three subsamples from each of two irradiated samples. Each subsamples were split and packed into three XRD holders, and measured by XRD. CI value for each subsample were calculated as the average of three measurements. Therefore, there are nine CI measurements for each irradiated sample and the standard error for each irradiated sample was calculated based on three CI measurements of subsamples. The standard error is 0.23 for YZ1210-4 and 0.34 for YZ110703-04m2, respectively. I adopt the average of these standard error, 0.29 as the reproducibility of CI in this thesis.

1.3 Results

1.3.1 ESR signal intensity of quartz in the riverbed sediments

1.3.1.1 The fine-silt (4–16 μm) fraction

Figure 1.6 (a) shows the geographical distribution of ESR signal intensity of quartz in the fine-silt fraction within the Yangtze drainage basin.

Samples collected from the mainstream show ESR signal intensity from 0.0 to 9.4 with an average of 3.9. ESR signal intensity of samples collected from the mainstream show an increasing trend from 0.0–2.3 in the uppermost part to 3.1–5.7 in the lower part toward the downstream, except in the uppermost part above Big Bend with values around 8. Samples collected from the Yalongjiang and Minjiang show ESR signal intensity from 0.0 to 5.5 with an average of 2.2, similar to those from the upper part of the mainstream, while samples collected from the Jialingjiang and Wujiang show ESR signal intensity from 1.5 to 15.5 with an average of 10.3, higher than those from the upper part of the mainstream. Samples collected from the tributaries in the middle part show wide range of ESR signal intensity from 0.0 to 23.4 with an average of 9.2, higher than those from the middle part of the mainstream.

1.3.1.2 The coarse-silt (16–63 μm) fraction

Figure 1.5(b) shows the geographical distribution of ESR signal intensity of quartz in the

coarse-silt fraction within the Yangtze drainage basin.

Samples collected from the mainstream show ESR signal intensity from 0.0 to 5.8 with an average of 2.6. Samples collected from the Yalongjiang and Minjiang show ESR signal intensity from 0.0 to 2.4 with an average of 1.2, similar to those from the upper part of the mainstream, while samples collected from the Jialingjiang and Wujiang show ESR signal intensity from 3.4 to 9.5 with an average of 5.2, higher than those from the upper part of the mainstream. Samples collected from the tributaries in the middle part show wide range of ESR signal intensity from 0.0 to 30.2 with an average of 11.2, higher than those from the middle part of the mainstream.

1.3.1.3 The sand (>63 μm) fraction

Figure 1.5(c) shows the geographical distribution of ESR signal intensity of quartz in the sand fraction of riverbed samples within the Yangtze drainage basin.

Samples collected from the mainstream show ESR signal intensity from 0.0 to 6.9 with an average of 1.6. ESR signal intensity of samples collected from the mainstream show an increasing trend from 0.0–0.9 in the uppermost part to 1.8–4.8 in the lower part toward the downstream, except in the uppermost part above Big Bend with values of 2.2–6.9. Samples collected from the tributaries in the uppermost and upper parts show low ESR signal intensity from 0.0 to 2.9 with an average of 1.1, comparable to those from the

uppermost and upper parts of the mainstream. Samples collected from the tributaries in the middle part show wide range of ESR signal intensity from 0.0 to 15.6 with an average of 5.4, higher than those from the middle and lower parts of the mainstream.

1.3.2 CI of quartz in riverbed sediments

1.3.1 The fine-silt fraction (4–16 μm)

Figure 1.7(a) shows the geographical distribution of CI values of quartz in the fine-silt fraction, which range from 6.8 to 9.0 with an average of 8.5 and a standard deviation of 0.4.

Samples collected from the mainstream show CI values from 6.8 to 9.0 with an average of 8.4, no obvious trend toward downstream. In the uppermost and upper parts, samples collected from the Yalongjiang and Daduhe show low CI values from 8.2 to 8.3, while samples collected from the Minjiang, Jialingjiang, and Wujiang show relatively high CI values from 8.6 to 8.9 with an average of 8.7. Samples collected from the tributaries in the middle part show wide range of CI values from 8.0 to 8.9 with an average of 8.5. Among the tributaries, some samples from the Minjiang, the Wujiang, Dongting Lake tributaries, and Poyang Lake tributaries show relatively high CI values around 9.

1.3.2 The coarse-silt fraction (16–63 μm)

Figure 1.7(b) shows the geographical distribution of CI values of quartz in the coarse-silt fraction within the Yangtze drainage basin.

Samples collected from the mainstream show CI values from 7.9 to 8.6 with an average of 8.4, and there is no clear trend downstream. Samples collected from the tributaries in the uppermost and upper parts show wide range of CI values from 7.9 to 8.7 with an average of 8.4. Samples from the tributaries in the middle part also show wide range of CI values from 7.9 to 9.1 with an average of 8.3. Among the tributaries, a sample from the Hanjiang is characterized by relatively high CI values around 9, while samples from Dongting Lake tributaries and Poyang Lake tributaries are characterized by low CI values around 8.

1.3.3 The sand (>63 μm) fraction

Figure 1.7(c) shows the geographical distribution of CI values of quartz in the sand fraction within the Yangtze drainage basin.

Samples collected from the mainstream show CI values from 8.2 to 8.8 with an average of 8.4, slightly increasing trend with scatter from 8.3 to 8.7. Samples collected from the tributaries in the uppermost and upper parts show wide range of CI values from 7.8 to 8.9 with an average of 8.5. Samples from the tributaries in the middle part also show wide range of CI values from 8.1 to 9.5 with an average of 8.7. Among the tributaries, some

samples from the Minjiang, Dongting Lake tributaries, the Hanjiang, and Poyang Lake tributaries are characterized by relatively high CI values around 9.

1.3.3 Comparison of ESR signal intensity among the three size fractions

Figure 1.8 shows ESR signal intensity difference for the various size fractions in the same sample collected from the major tributaries. A comparison of ESR signal intensity in the fine-silt and sand fractions revealed that samples taken from the Jinshajiang, Minjiang, and Hanjiang show similar values, whereas some of samples from the Jialingjiang, Wujiang, Dongting Lake tributaries, and Poyang Lake tributaries show higher ESR signal intensity in the fine-silt fraction than those in the sand fraction (Figure 1.8a). Similarly, a comparison of ESR signal intensity in the fine-silt and the coarse-silt fractions in samples from the Jinshajiang and Minjiang revealed similar values. Samples from the Jialingjiang and Wujiang show larger ESR signal intensity in the fine-silt fraction than those in the coarse-silt fraction. Many of the samples from the Hanjiang, Dongting Lake tributaries, and Poyang Lake tributaries show similar values between the fine-silt and coarse-silt fractions. However, some samples taken from the Dongting Lake drainage basin show larger ESR signal intensity in the fine-silt fraction, while some samples collected from the Hanjiang, Dongting Lake drainage basin, and Poyang Lake drainage basin show larger

ESR signal intensity in the coarse-silt fraction (Figure 1.8b). The different ESR signal intensity among the three size fractions suggest origins of different sources. Thus, grain size should be considered when discussing the provenance of sediments.

1.3.4 Comparison of ESR signal intensity between the fine-silt fraction of riverbed samples and SPM samples

Although the mode diameter of SPM is within the range of the fine-silt (4–16 μm) fraction, the coarse-silt (16–63 μm) and very fine sand (63–125 μm) fractions are also transported as suspension in addition to the clay (<4 μm) and fine-silt (4–16 μm) fractions (Mao et al., 2010; Gao et al., 2015). Therefore, it is necessary to check if the fine-silt fraction of riverbed samples could represent SPM by the comparison of ESR signal intensity between them.

Three SPM samples (JSJ-GLS, JSJ110701, and YZ110703-03) are analyzed for comparing with the riverbed sediments which are collected at the same locality in the same day. ESR signal intensity of these SPM samples (JSJ-GLS, JSJ110701, and YZ110703-03) are 7.9, 5.6, and 3.4, respectively, which agree within errors with ESR signal intensity of 8.7, 2.3, and 3.9 for corresponding riverbed samples (UYZ110911-01m, YZ110701-01c, and YZ110703-04m). Thus, ESR signal intensity of quartz in the fine-

silt (4–16 μm) of the riverbed sediments basically represent that of the SPMs.

1.3.5 Seasonal variation in ESR signal intensity of the riverbed sediments

To examine the seasonal variation in ESR signal intensity of the riverbed sediments, three places where samples were collected in both summer and winter are selected: the Jinshajiang above the junction with the Minjiang, the Yangtze below the junction with the Minjiang, and the Jialingjiang. In these three places, the samples in summer and winter were collected in the exact same sites. ESR signal intensity of the fine–silt fraction at the Jinshajiang above the junction with the Minjiang are 2.3 in a sample that was collected in summer, and 3.2 and 0.0 in samples that were collected in winter. ESR signal intensity of the fine–silt fraction at the Yangtze below the junction with the Minjiang are 1.6 in a sample that was collected in summer, and 1.6 in a sample that was collected in winter. ESR signal intensity of the fine–silt fraction at the Jialingjiang are 1.4 and 11.0 in a sample that were collected in summer, and 5.5 in a sample that was corrected in winter. In summary, the difference of ESR signal intensity among samples at the sites above and below the junction with the Minjiang are small regardless of seasons, while those among samples at the Jialingjiang are large even in the same season.

1.4 Discussion

1.4.1 Relationship between ESR signal intensity and CI values of riverbed sediments and ages and types of bedrocks in their tributaries

In this section, I summarize ESR and CI values of the sediments collected from each tributary and examine their relation with ages and types of bedrocks exposed in the drainage basin. Figure 1.9 shows ESR signal intensity and CI values of samples from tributaries. Since the basement rocks in each geological block are generally considered as the source of younger detrital sediments on the block, each sample is categorized with respect to the geological block(s) exposed in its drainage basin (Figure 1.9). The geological blocks that compose the basement rocks in the Yangtze River drainage are classified into 5 types. Namely, Qamdo Block and Yidun Arc (QY), Songpan-Garze terrane (SG), Qinling orogenic belt (QL), Yangtze Block (YZ), and Cathaysia Block (CX). In addition, Quaternary sediments distribute in the middle to lower parts are classified as sixth type (Q). Mesozoic terrestrial sediments in Sichuan Basin, which unconformably cover the basement, is considered as derived from both Songpan-Garze Terrane (SG) and Qinling orogenic belt (QL), although the basement of Sichuan Basin belongs to Yangtze Block (YZ; Wang et al. 2013; Luo et al. 2014).

ESR signal intensity increases with an increase in age of the host rock (Toyoda and Naruse

2002). According to Toyoda (1992), the Cenozoic granites show E_1' center density of less than 1.3×10^{15} spins/g, while the Proterozoic granites show E_1' center density of more than 1.3×10^{16} spins/g. Since the unit of ESR signal intensity is defined as 1.3×10^{15} spins/g, ESR signal intensity of the Cenozoic rocks is below ~1, that of the Mesozoic rocks is between ~1 and ~3, that of the upper Paleozoic rock is between ~3 and ~10, and that of Proterozoic rocks is over ~10 (Toyoda and Hattori 2000). Based on this general tendency, I categorize ESR signal intensity into three classes; low (<3; roughly corresponding to Cenozoic and Mesozoic), medium (between 3 and 10; roughly corresponding to Paleozoic), and high (>10; roughly corresponding to Proterozoic), although I have to take into account a rock type dependency of ESR signal intensity due to the difference in radionuclides activity.

I also categorize CI values into three classes based on 1st quartile (8.2) and 3rd quartile (8.7) of all fractions; low CI values means below 8.2, medium CI values means between 8.2 to 8.7, and high CI values means above 8.7.

1.4.1.1 Correlation between ESR signal intensity and CI values of the fine-silt (4–16 μm) fraction of sediments from tributaries and the geological blocks of their drainage basin

Quartz grains in the riverbed sediments could be the mixture from different source rocks within each geological block, and ESR signal intensity and CI values of the riverbed sediments do not necessarily represent those of a single source. In the discussion below, yet, it is assumed that the range of ESR signal intensity and CI values in the riverbed samples collected from each geological block represent the minimum range of those values in the various source rocks within that geological block.

Figure 1.9a shows ESR signal intensity and CI values of quartz in the fine-silt fraction where symbols are categorized based on the geological block(s) exposed in the drainage basin of each sample. As shown in results section, the fine-silt fraction could well represent the composition of SPM of the Yangtze River. Here I discuss feature of ESR and CI in the fine-silt fraction as SPM provenance proxies.

Songpan-Garze terrane (SG): Samples derived from SG have low to medium ESR signal intensity of 0.0 to 5.3, and medium CI values of 8.2 to 8.8. SG is mainly composed of Mesozoic shallow marine sediments including sandstone and carbonates (Enkelmann et al. 2007; Liu et al. 2011), which is consistent with low ESR signal intensity.

Qamdo Block and Yidun Arc (QY): Samples derived from QY have medium ESR signal intensity around 8 and low CI values of 7.8 to 8.2. Yidun arc, which occupies large part of QY, is composed of Paleozoic melange and Permian to Tertiary shale and

sandstones that yield Upper Paleozoic to Proterozoic zircon ages (Wang et al. 2000; Reid et al. 2005b; Deng et al. 2014), which are consistent with medium ESR signal intensity around 8.

Qinling orogenic belt (QL): Samples derived from QL have medium ESR signal intensity around 9 and medium CI values around 8.4. QL is mainly composed of Neoproterozoic turbidite, phyllite, and sandstone; Silurian slate and sandstone; Devonian schist; and Triassic granite (Meng and Zhang 2000; Dong et al. 2011; Dong et al. 2016). Since QL block in the Yangtze drainage basin did not suffer metamorphism after Neoproterozoic (Dong et al. 2011; Dong et al. 2016), the rocks in QL are assumed to yield quartz with the original age of Upper Paleozoic to Proterozoic. This age does not contradict with ESR signal intensity of 8.

Yangtze Block (YZ): Samples derived from YZ have high ESR signal intensity of 12 to 23 and medium to high CI values of 8.3 to 9.0. YZ is mainly composed of Proterozoic basement that suffered low-grade metamorphism by Neoproterozoic, and lower Paleozoic sandstone, mudstone, and carbonates (Chen and Jahn 1998; Wang et al. 2010; Wang et al. 2013). Since Lower Paleozoic sandstones in YZ are assumed to be derived from Proterozoic basement and/or granites in Cathaysia Block (Wang et al. 2010), both Proterozoic basement and Paleozoic clastic rocks seems to have source rock age of

Proterozoic period. This is consistent with high ESR signal intensity over 10.

Cathaysia Block (CX): A sample derived from CX has high ESR signal intensity of 12.2 and medium CI value of 8.6. CX is mainly composed of Proterozoic basement, lower Paleozoic siliciclastics, and Cretaceous red-colored sandstone (Wang et al. 2007a; Wang et al. 2013). Cretaceous sandstones were probably derived from YZ basement, which have the source rock of Proterozoic ages as mentioned above, which is consistent with ESR signal intensity over 10.

Quaternary sediments in the middle to lower parts (Q): This type of sediments is thought to have been brought by the Yangtze mainstream (Dai et al. 2010; Yin et al. 2007). Therefore, sediments of Quaternary (Q) around the middle and lower parts could be represented by the riverbed sediments deposited in the middle part of the mainstream, where ESR signal intensity is low around 3 and CI values is medium around 8.4.

Mixing of various source rocks: Samples derived from QY+SG (from the Jinshajiang) have low to medium ESR signal intensity from 0.0 to 3.2 and medium to high CI values from 8.3 to 9.0, which are close to the values of SG. Because 80% of sediments discharged from the Jinshajiang are derived from SG region around the lower part of the Jinshajiang (Liu et al. 2011), it is reasonable that ESR signal intensity and CI values of samples derived from QY+SG are strongly affected by SG. Samples derived from QL+SG (from

the Jialingjiang) have a wide range of ESR signal intensity of 1.4 to 10.9 and medium CI values around 8.6. These values lie between those of SG and QL, supporting the idea that the sediments of QL+SG are mixtures of sediments yielded from QL and SG. A sample derived from QL+Q (from the Hanjiang) has medium ESR signal intensity of 3.3 and medium CI values of 8.4. Samples derived from YZ+Q taken from the Dongting Lake tributaries have low to high ESR signal intensity from 0 to 14. Samples derived from CX+Q taken in the Poyang Lake tributaries have low to medium ESR signal intensity from 0 to 6. Because sediments of Q have similar ESR signal intensity and CI values of samples from the middle part of the mainstream, ESR signal intensity and CI values of QL+Q, YZ+Q, and CX+Q lie along the mixing lines between QL and Q, YZ and Q, and CX and Q, respectively. Therefore, it can be said that the ESR and CI values of these samples can be explained by the mixture of each geological block.

Wang et al. (2007) studied Sr and Nd isotope ratio in the riverbed sediments and SPM along the mainstream and tributaries in the Yangtze River. Their result showed that $^{87}Sr/^{86}Sr$ ratio in the riverbed sediments and SPM in the Yangtze River tend to increase toward the lower reaches, reflecting the increase of $^{87}Sr/^{86}Sr$ ratio in the bedrocks that were exposed in each reaches, and that $^{87}Sr/^{86}Sr$ ratio of the tributaries in the middle reaches were highest value within the whole basin (Figure 1.10). In addition, those isotope

ratios reflect the difference in the isotope ratios of the bedrocks which are exposed in the basin, which also increase toward the lower part of the basin. He et al. (2015), which also studied the geochemistry of the riverbed sediment within the Yangtze basin, reported that $^{143}Nd/^{144}Nd$ and $^{87}Sr/^{86}Sr$ isotope ratios were different among each part of the Yangtze depending on the geological block(s), and $^{87}Sr/^{86}Sr$ ratio is especially high in the tributaries in the middle part of the Yangtze Basin, They also reported that the riverbed sediments in the middle to lower parts of the mainstream were mainly derived from Songpan-Garze Terrane and Yangtze Block, based on those isotope ratios. Both of their results are consistent with my results that the ESR signal intensity and CI value reflect the difference in the geological block(s) which are exposed within each part of the Yangtze River.

On the other hand, because detrital particles in the sediment rocks could be eroded and transported from other older rocks, the ESR signal intensity of quartz in the sediment rocks could show a high (older) value compared to the ESR signal intensity expected based on the depositional age of the sediment rocks. Actually, in the Songpan-Garze Terrane in the upper to uppermost basins of the Yangtze, the zircon ages in the sandstones have peaks around 345, 749, and 1855 Ma, which are mostly older than the depositional ages of the Songpan-Garze Terrance around 230-200 Ma (Enkelmann et al., 2007;

Weislogel et al., 2010; Figure 1.11a) However, the mica ages, which are reset at 350 ℃, show similar ages to the depositional ages of the terrane around 230 Ma (Enkelmann et al., 2007; Figure 1.11b). In addition, it was reported that the E_1' center of quartz were decayed by heated over 400 ℃ (Toyoda, 1991), suggesting that the E_1' center of quartz were also decayed and that the ESR signal intensity of quartz are reset around 200-230 Ma. Thus, the low ESR signal intensity in the upper to uppermost basins do not contradict with the ages based on other proxies. In the middle to lower basins, the zircon ages in the eastern Yangtze Block and the Cathaysia Block have peaks before 800 Ma which tend to be older than those in the upper to uppermost basins; namely, 855, 1088, 1493, 1825, 2556 Ma in the eastern Yangtze Block and 468, 762, 891, 1097, 1847 Ma in the Cathaysia Block (Figure 1.11b and 1.11c). In addition, compared to the upper to uppermost basins, where are tectonically active due to the Tibet-Himalayan uplift, the middle to lower basins are relatively stable since the Proterozoic, suggesting that the ESR signal intensity in the middle to lower basins preserve high values corresponding the Proterozoic to Paleozoic ages.

In summary, it is demonstrated that, ESR signal intensity of the fine-silt fraction (4–16 μm) extracted from riverbed samples in each geological block are consistent with the age of dominant rock types there.

1.4.1.2 The difference in ESR signal intensity and CI values among three size fractions in each geological blocks

As is shown in Figure 1.8, there are clear differences in ESR signal intensity and CI values among three size fractions, and the nature of differences changes depending on the geological blocks. Thus, in this subsection, the difference in ESR signal intensity and CI values among three size fractions for each geological block are discussed below.

Qamdo Block and Yidun Arc (QY): The sand fraction of samples from QY show lower to similar ESR signal intensity between 2.2 and 6.9 and slightly higher CI values around 8.3 compared to those of the fine-silt fraction, while the coarse-silt fraction show intermediate values between the sand fraction and the fine-silt fractions (Figure 1.9a–c). Clastic sediments in QY block yield Proterozoic to Upper Paleozoic zircon ages (Wang et al. 2000; Deng et al. 2014), which is consistent with medium ESR signal intensity in the fine-silt fraction. On the contrary, coarse clastic sediments or Mesozoic granite-granodiorite may have contributed to low ESR signal intensity in the sand fraction, although it is difficult to specify the source rock of each fraction due to the complex structure of QY block (Reid et al. 2005a).

Songpan-Garze terrane (SG): The coarse-silt fractions of samples derived from SG show low ESR signal intensity of 0.0 to 2.4 and low to medium CI values of 8.0 to 8.7 in

the coarse-silt fraction, and the sand fraction of those samples show low ESR signal intensity of 0.0 to 2.9 and wide range of CI values of 7.8 to 8.9 (Figure 1.9b, 1.9c). Since samples derived from SG show similar ESR signal intensity and CI values among the three size fractions, the three size fractions of SG seems to be derived from the same rocks.

Qinling orogenic belt (QL): The coarse-silt fraction of samples derived from QL show similar to higher ESR signal intensity of 7.8 to 19.3 and lower to similar CI values of 7.8 to 8.4 compared to those of the fine-silt fraction, whereas the sand fraction of those samples show similar to higher ESR signal intensity of 5.9 to 9.8 and higher CI values of 9.2 to 9.5 compared to those of the fine-silt fraction (Figure 1.9a–c). Considering high CI values of the sand and coarse-silt fractions, Neoproterozoic and Triassic granite in South Qinling area or Quaternary loess within Hanjiang drainage basin may have contributed to the coarse-silt and sand fractions (Meng and Zhang 2000; Dong et al. 2011; Zhang et al. 2012; Dong et al. 2016).

Yangtze Block (YZ): The sand and coarse-silt fractions of samples derived from YZ show lower to similar ESR signal intensity of 3.4 to 30.0 and lower to similar CI values of 8.1 to 8.6 compared to those of the fine-silt fractions (Figure 1.9a–c). Silicate rocks within YZ are dominantly composed of Proterozoic basement that were metamorphosed during Neoproterozoic, lower Paleozoic slate and sandstone, Mesozoic sandstone, and

Mesozoic granite (Wang et al. 2013). Based on high ESR signal intensity and medium to high CI values, the fine-silt fraction seems to be derived from Proterozoic basement. In YZ area, lower Paleozoic sandstones seem to be derived from Proterozoic basements of Cathaysia Block (CX), and are considered to have high ESR signal intensity and low CI values, while Mesozoic granites are considered to have low ESR signal intensity and high CI values (Wang et al. 2010; Wang et al. 2013). Therefore, lower ESR signal intensity and CI of the coarse-silt and sand fractions than those of the fine-silt fraction in YZ could be explained by some contribution from Mesozoic granite in addition to Paleozoic sandstones.

Cathaysia Block (CX): The sand fraction of samples derived from CX shows lower ESR signal intensity of 4.8 to 6.6 and higher CI values of 9.0 to 9.2 compared to those of the fine-silt fractions. Since granites intermittently intruded into CX during Neoproterozoic to Jurassic (Wang et al. 2013), higher CI values in the coarser fractions might be explained by these granites.

It is suggested that the detrital quartz grains of different grain size are derived from different sources. To test the possible explanation for difference in ESR signal intensity and CI values as mentioned above, ESR analysis of quartz combined with petrological observation of quartz grain size in all kinds of the potential source rocks within each

geological block are necessary.

1.4.1.3 Classification of tributaries based on ESR and CI values of the fine-silt fraction of sediments discharged from each tributary

As to the fine-silt fraction, the major tributaries can be categorized into four groups based on the geological block(s) exposed in each drainage basin (Figure 1.12); 1) the upper part of the Jinshajiang, including the Jinshajiang above Big Bend, 2) western tributaries, including the lower parts of the Jinshajiang, Yalongjiang, and Minjiang, 3) northeastern tributaries, including the Jialingjiang and Hanjiang, and 4) southeastern tributaries, including the Wujiang, Dongting Lake tributaries, and Poyang Lake tributaries.

The upper part of the Jinshajiang are characterized by medium ESR signal intensity of 7.5–8.7 and low CI values of 7.9–8.2, reflecting clastic sediments with Upper Paleozoic to Proterozoic ages. This groups is nearly equivalent to QY. The western tributaries are characterized by low ESR values of 0.0 to 3.2 and a wide range of CI values from 7.8 to 9.0, reflecting Mesozoic shallow marine sediments including sandstone and carbonates. This groups is characterized by a dominant contribution from SG. The northeastern tributaries are characterized by a wide range of ESR values of 1.5–11.0 and medium CI values of 8.3–8.7. This group reflects both Mesozoic shallow marine sediments derived from SG and Upper Paleozoic clastic rocks and Proterozoic basement in QL block. The

southeastern tributaries are characterized by high ESR values of 11.3–23.4 and low-medium CI values of 8.4–8.9. This block represents Proterozoic basement in YZ and CX blocks. Because the contribution from the lower part is negligible, it will not be discussed here.

1.4.2 Prediction of change in ESR signal intensity of the modern Yangtze mainstream below the junction with the major tributaries

To evaluate whether ESR signal intensity of the sediments in the mainstream just below the junction with the tributary properly reflects the observed mixing ratios of the sediments disharged from the mainstream and tributary above the junction, I calculated the theoretical (predicted) ESR signal intensity of quartz in the fine-silt fraction of the sediments immediately below the junctions with the major tributaries and compare them with the analyzed values. I used the sediment (SPM) budget at the junctions in the modern (post-TGD) condition based on observational data (Figure 1.4) in addition to the analyzed ESR signal intensity of quartz in the fine-silt fraction of the sediments from each tributary and from sites along the mainstream immediately above the junctions with the tributaries as end members for mixing and calculate the predicted ESR signal intensity of quartz

after the mixing. The results are compared with the analyzed ESR signal intensity for the fine-silt fraction of samples collected from the site along the mainstream immediately below the junction.

ESR signal intensity and CI values of quartz in the fine fraction of the sediments from each tributary were assumed, as listed in Table 1. As is previously mentioned, ESR signal intensity and CI values of the sediments collected from Yibin, the outlet of the Jinshajiang, appears to be strongly affected by the sediments supplied from the lower part of the Jinshajiang. Therefore, in the calculation of the average ESR signal intensity and CI values of the fine-silt fraction of the sediments from the Jinshajiang, only samples in the lower part of the Jinshajiang were used. For the Hanjiang, Dongting Lake, and Poyang Lake, samples collected from the middle part of the Hanjiang, the middle part of tributaries of Dongting Lake, and the tributary of Poyang Lake were used, because other samples from the lower part of each drainage basin and along the shoreline of the lakes are likely contaminated by sediments from the mainstream during floods.

ESR signal intensity and CI values below the junction with the tributary are calculated as the weighted average of those of the mainstream immediately above the junction and of the tributary based on the ratio of fine-silt sized quartz load from the mainstream and the tributary, respectively.

In the calculation below, the assumption that sediments from the mainstream and the tributaries are sufficiently mixed below the junction is made to conduct the calculation. Underlined variables in the following equations indicate observed or analyzed data.

First, I calculated the fine-silt-sized quartz load from the mainstream (Q_{main}; Mt/yr) and the tributary (Q_{tri}; Mt/yr) as

$$Q_{main(aj)} = \underline{S}_{main(aj)} \times \underline{f}_{fs} \times \underline{C}_{main(aj)}, \quad (1)$$

$$Q_{tri} = \underline{S}_{tri} \times \underline{f}_{fs} \times \underline{C}_{tri}, \quad (2)$$

where $\underline{S}_{main(aj)}$ is the observed sediment load of the mainstream just above the junction with the tributary of interest (Mt/yr), $\underline{f}_{fs}$ is the ratio of the fine-silt fraction in the whole SPM, and $\underline{C}_{main(aj)}$ is the analyzed quartz content in the fine-silt fraction of the sediments collected from the site of the mainstream just above the junction with tributary of interest. Similarly, $\underline{S}_{tri}$ is the observed sediment load from the tributary of interest (Mt/yr), and $\underline{C}_{tri}$ is the analyzed quartz content in the fine-silt fraction of the sediments collected from the tributary of interest. The average annual sediment load from the mainstream and each tributary shown in Figure 1.4 (after TGD operation) is used as $\underline{S}_{main(aj)}$ and $\underline{S}_{tri}$, because my samples were collected after the operation of the TGD.

Since the grain size distribution of SPM changes seasonally and among the different parts (Mao et al. 2010), the value of $\underline{f}_{fs}$ could also change depending on the seasons and parts.

I estimated the value of f_{fs} as below.

As to the seasonal variation, it is assumed that f_{fs} during the summer can be regarded as the annual average, since roughly 90% of the annual sediment yield from the Yangtze River occurs during the summer (Hu et al. 2011). To evaluate the value of f_{fs}, I analyzed the grain size distribution of SPM samples taken at Yichang and Nanjing at the same season and year as my riverbed sampling. The value of f_{fs} at Yichang and Nanjing are 32% and 34%, respectively. These ratios of the fine-silt fraction in SPM is consistent with those at Yichang and Datong in Gao et al. (2015), respectively. Since f_{fs} at Yichang and Nanjing are close, I adopt the average of f_{fs} at Yichang and Nanjing, 33%, as f_{fs} in equation (1) and (2).

Next, I calculated the fine-silt-sized quartz load of the mainstream below the junction ($Q_{main(bj)}$; Mt/yr) as

$$Q_{main(bj)} = Q_{main(aj)} + Q_{tri}, \quad (3)$$

Next, I calculated the contribution ratio of the fine-silt-sized quartz load of the mainstream above the junction to that of the mainstream below the junction ($r_{Q,main}$) in addition to the contribution ratio of the fine-silt-sized quartz load from the tributary of interest to that of the mainstream below junction (r_{Qtri}) by using equations (4) and (5), respectively.

$$r_{Q,main} = Q_{main(aj)} / Q_{main(bj)}, \quad (4)$$

$$r_{Q,tri} = Q_{tri} / Q_{main(bj)}, \quad (5)$$

Finally, I calculated ESR signal intensity of quartz in the fine-silt fraction of the sediment from the mainstream below the junction ($ESR_{main(bj)}$) as

$$ESR_{main(bj)} = \underline{ESR}_{main(aj)} \times r_{Q,main} + \underline{ESR}_{tri} \times r_{Q,tri}, \quad (6)$$

where $\underline{ESR}_{main(aj)}$ is the analyzed ESR signal intensity of quartz in the fine-silt fraction of the sediments from the mainstream above the junction and $\underline{ESR}_{tri}$ is the analyzed ESR value of quartz in the fine-silt fraction of the sediments from the tributary. $\underline{ESR}_{tri}$ is assumed to change between the minimum and maximum ESR signal intensity shown in Table 1.

Using the equation (1) to (6), ESR signal intensity below the junction are predicted at the junction with the Minjiang, Jialingjiang, Wujiang, and Poyang Lake. The junction with the Yalongjiang and Dongting Lake are excluded, because the riverbed sediments of the mainstream lacks above the junction with these tributaries. The junction with the Hanjiang is also excluded, since the sample collected from the mainstream above the junction with the Hanjiang show an exceptional ESR signal intensity of 0.0. Since this sample was collected from the meter-scale bedded sediments exposed above the river surface, this sample could represent the past sediments deposited during a flood, and show

low ESR signal intensity reflecting a specific source area, such as SG block.

The result of calculation is shown in Table 2. Figure 1.13 shows the correlation between the predicted and analyzed ESR signal intensity at the mainstream below the junction with each major tributary. The analyzed ESR signal intensity agree with the predicted values within the reproducibility of the analyzed ESR values (±2.2) below the junction with the Minjiang, the Jialingjiang, and Poyang Lake, indicating the analyzed ESR signal intensity properly reflect the sediment contribution from the mainstream and the tributary above the junction.

On the contrary, the analyzed ESR signal intensity below the junction with the Wujiang is larger than the predicted values beyond the analytical error. The sampling site is located 40 km below the junction with the Wujiang (LYZ120212-01a), and a local river called the Longhe drained into the mainstream from the side same as the Wujiang at the location less than 1 km above the sampling site. Since geology of the drainage basin of the Longhe is similar to that of the Wujiang, it is likely that detrital material from Longhe is characterized by high ESR value, which may have affected the ESR value of sample LYZ120212-01a due to the proximity of the Longhe to the sampling site. Thus, because of the effect from the high ESR signal intensity of sediments from the Longhe, the analyzed ESR signal intensity LYZ120212-01a seems to become higher than predicted.

1.4.3 Estimation of ESR signal intensity and CI values of quartz in the fine-silt fraction of modern sediments along the mainstream of the Yangtze

As is shown in the previous section, it can be assumed that the analyzed ESR signal intensity of samples collected from the site below the junction with the major tributaries reflect the sediment contribution from the mainstream and tributary above the junction. Using the similar calculation, I can estimate the changes in ESR signal intensity of the fine-silt fraction of the sediments along the mainstream from the uppermost part to the rivermouth. This could test whether ESR signal intensity in the fine-silt fraction of the sediments at the rivermouth can be predicted by the similar calculation based on the sediment budget of the whole Yangtze drainage basin in the past.

The following assumptions are made to conduct the calculation: (a) sediments from the mainstream and the tributaries are sufficiently mixed below the junction; (b) sediment input from small tributaries are negligible; and (c) the quartz content do not change during transportation as SPM along the mainstream.

First, the calculation starts from the junction of the Jinshajiang and Minjiang, and ESR signal intensity below that junction is predicted using equations (1) to (6) in the previous section. Due to the Jiangqiao Dam on the mainstream of the Jinshajiang at the time of the

sampling, the sediments derived from the upper Jinshajiang area are assumed to be trapped in the dam and prevented from flowing into the downstream, including all the junction with the major tributaries shown in Figure 1.2. Because the uppermost part of the Jinshajiang mainly are occupied by the geological blocks formed during the Mesozoic (Songpan-Garze Terrane) except the upper Jinshajiang area, the sediments discharged from the uppermost part of the Yangtze are expected to be homogeneous and assumed to be represented by the sample at the outlet of the uppermost part, namely above the junction with the Minjiang. Thus, the ESR signal intensity of sediments above the junction with the Minjiang is used the initial value in the calculations in this section. Next, the calculation is conducted at the junction of the Yangtze mainstream and the Jialingjiang using the same equations, but ESR signal intensity of the mainstream above the junction is assumed to be the same as the predicted value below the previous junction, namely the junction of the Jinshajiang and Minjiang. Then, the similar calculation are repeated at every junction with the major tributaries; the Wujiang, Dongting Lake, the Hanjiang, and Poyang Lake.

In addition to the sediment input from the tributaries, the amount of eroded sediments between the mainstream from Yichang to Hankou is assumed as 47 Mt/yr, and from Hankou to Datong as 17 Mt/yr (Figure 1.4). In my calculation, erosion between Yichang

and Hankou are split into two parts equally; from Yichang to Yueyang (outlet of DTL) and from Yueyang to Hankou. ESR signal intensity and CI values for the eroded sediments between Yichang and Yueyang, Yueyang and Hankou, and Hankou and Datong are assumed to be the same with the sediments passing through Yichang, Yueyang, and Hankou before TGD construction, respectively, because the sediments were deposited along the middle to lower part of the mainstream before TGD construction (Figure 1.3). ESR signal intensity and CI values at Yichang, Yueyang, and Hankou before TGD are estimated by the same calculation using equation (1) to (6) and the sediment budget shown in Figure 1.3.

It is assumed that 80.3% of the sediment flowing into TGD area between the junction with Wujiang and the dam body is trapped in the TGD as

$$Q_{TGD,output} = (1-0.803) \times Q_{TGD,input} \quad (7)$$

where $Q_{TGD,input}$ is the quartz load of the mainstream below the junction with Wujiang, and $Q_{TGD,output}$ is the quartz load of the mainstream below TGD, Yichang.

Similar to equation (7), it is assumed that 10.0% of the sediment flowing into DTL is deposited within Dongting Lake on the basis of the sediment budget in Figure 1.4.

$$Q_{DTL,output} = 0.9 \times Q_{DTL,input} \quad (8)$$

The calculation described above was repeated at every junction from the upper part to the

lower part along the mainstream (Table 3, Figure 1.14). The results of calculation using averaged ESR signal intensity and CI values in Table 1 are shown as “predicted average” of ESR and CI for each tributary in Table 3. Similarly, the result of the calculation using maximum and minimum values of ESR and CI in Table 1 are shown as “predicted maximum” and “predicted minimum” values of ESR signal intensity and CI for each tributary in Table 3. As is described in the previous section, the sediments collected from the site below the junction with the Wujiang and the site above the junction with Hanjiang are assumed to be exceptional. Thus, these two sediments are omitted in both Table 3 and Figure 1.14.

If the sediment budget shown in Figure 1.4 is properly reflected in the sediment composition along the mainstream, it is expected that the predicted average ESR signal intensity and CI values after mixing will fall within the analytical error of the analyzed ESR signal intensity of the riverbed sediments. Figure 1.14 show that the predicted average ESR signal intensity (solid circles) agree with the analyzed ESR signal intensity within the reproducibility of ESR analysis (±2.2; open circles with errors) at eight out of ten locations, indicating that the predicted average ESR signal intensity could be used for predicting ESR signal intensity of the riverbed sediments.

Two predicted values below the junctions with Dongting Lake and Poyang Lake fall out

of the analyzed values. Lane et al. (2008) reported that several to tens of kilometers of distance are necessary for river waters to completely mix after two rivers are merged. Sampling sites below the junctions on the mainstream with Dongting Lake, which show higher ESR values than the predicted ESR values, is located on the tributary merging side of the mainstream 8 kilometers below the junction. As previously described, ESR signal intensity for Dongting Lake is characterized with higher values as those of the mainstream. Thus, it is likely that samples below the junction with Dongting Lake are influenced by the sediments derived from the lake, which have higher ESR values than those of the mainstream above the junctions. This problem could be resolved by taking samples from the sites with sufficient distance from the junctions with the tributaries.

On the other hand, the analyzed ESR signal intensity in the middle to lower parts tend to be lower compared to the predicted values. These lower values could be affected by the erosion along the middle to lower parts of the mainstream. Since the meter-scale bedded sediments above the junction with the Hanjiang which could be eroded and whose ESR signal intensity are 0.0, ESR signal intensity of eroded sediments could be very low to zero. In my present prediction of ESR signal intensity along the mainstream, it is assumed that the eroded sediments in the middle to lower parts have the average ESR signal intensity around 4 that was observed at Yichang or Yueyang. If I assume that all the eroded

sediments have ESR signal intensity of 0, the predicted average ESR signal intensity will be 4.6, very close the analyzed values. Thus, the reason why the analyzed ESR values in the middle to lower parts are lower than predicted values could be explained by the lower ESR signal intensity of eroded sediments lower than expected.

In summary, the average of the predicted ESR signal intensity of the fine-silt fraction along the modern mainstream is consistent with the analyzed values when an incomplete mixing of tributary water and eroded materials are taken into account. Therefore, ESR signal intensity of the sediments at the rivermouth would record the relative contribution of sediments discharged from each part of the Yangtze River basin.

1.4.4 Possibility to distinguish the provenance of the fine-silt fraction of the sediments within the Yangtze drainage basin using ESR signal intensity

It is probable to reconstruct the movement of the monsoon rain front based on ESR signal intensity and CI values of the fine-silt fraction of sediments at the rivermouth, if I can distinguish the contribution of sediments from two tributary groups within the Yangtze drainage basin at least; namely, the western plus northeastern tributaries, and the southeastern tributaries as shown in Figure 1.12.

Using calculation of equation (1) to (6), ESR signal intensity of sediments discharged

from the western plus northeastern tributaries and the southeastern tributaries can be calculated.

$$R_{tri} = Q_{tri} / Q_{trig} \quad (7)$$

where Q_{trig} is the total quartz load in the tributary group, R_{tri} is the contribution ratio of quartz from each tributary for the total quartz load within the tributary group. Q_{tri} is the same as equation (1).

$$ESR_{trig} = ESR_{tri1} \times R_{tri1} + ESR_{tri2} \times R_{tri2} + \ldots \quad (8)$$

where ESR_{trig} is the predicted ESR signal intensity of sediments from each tributary group, ESR_{tri1}, ESR_{tri2} … are ESR signal intensity of each tributary within the tributary group.

These calculations are done for each of the minimum, average, and maximum ESR signal intensity shown in Table 1. ESR signal intensity of sediment discharged from the western plus northeastern tributary group are 4.3 in average, 2.5 at the minimum, and 6.3 at the maximum, while those from the southeastern tributary group are 14.3 in average, 12.8 at the minimum, and 16.3 at the maximum, respectively. Thus, ESR signal intensity of the two groups do not overlapping each other. If I assume that the sediments at the rivermouth are the mixture of these two end members, I can estimate the relative contribution from the western plus northeastern tributaries and the southeastern tributaries to the sediments

at the rivermouth using ESR signal intensity.

1.5 Summary

Meteorological data suggest that changes in the strength of EASM result in changes in spatial distribution of monsoon precipitation. To reconstruct changes in the spatial distribution of precipitation caused by changes in EASM intensity in the past, it is useful to reconstruct the temporal changes in the provenance of the sediments because they may record changes in the distribution of heavy precipitation areas in the geological past.

In this chapter, riverbed sediments taken from the Yangtze mainstream and its major tributaries are analyzed on the basis of ESR signal intensity and CI values of quartz in three different size fractions to distinguish the source of sediments yielded from the Yangtze drainage basin. The results suggest that sediment from each tributary can be categorized into four groups based on the geological block(s) exposed within the drainage basin of each tributary, and that each group has a characteristic ESR signal intensity and CI values. The first group is characterized by intermediate ESR values of ~7 and low CI values of 7.9–8.2, corresponding to Yidun Arc, the southwestern margin of the Yangtze Block. The second group is characterized by lower ESR values below 5 and a wide range of CI values between 8 and 9, corresponding to the Songpan-Garze terrain. The third group is characterized by a wide range of ESR values from 1 to 10 and narrow CI values of 8.5–8.9, corresponding to the Qinling orogenic belt. The fourth group is characterized

by high ESR valued greater than 10 and CI values of 8–9 in the southeastern part of the Yangtze drainage basin, corresponding to the southeastern parts of the Yangtze and Cathaysia Blocks.

The theoretical ESR signal intensity below the junction of the mainstream and major tributary is calculated as the weighted average based on the quartz discharge of the mainstream and tributary just above the junction. These predicted ESR signal intensity are compared to the analyzed ESR signal intensity of sediments collected from the mainstream just below the junction with the tributaries. The analyzed values agree with the predicted values within the reproducibility of ESR analysis, indicating the analyzed ESR signal intensity of the sediments properly reflect the quartz contribution from the mainstream and the tributary above the junction.

In addition, by using ESR signal intensity and CI values of quartz in the fine-silt fraction discharged from the major tributaries, the changes in ESR and CI values along the mainstream are estimated assuming complete mixing of the sediments from the mainstream and from each tributary immediately below the junction. The predicted average ESR signal intensity of the riverbed samples agree with analyzed ESR signal intensity of the same sample within the reproducibility of ESR analysis, except some sample which are insufficiently mixed or affected from a small tributary. Thus, it is

concluded that ESR signal intensity and CI values can be used for estimating the mixing ratio of sediments from each tributary in the Yangtze drainage basin in the fine-silt fraction, indicating the possibility to reconstruct the spatial distribution of precipitation within the Yangtze drainage basin.

Chapter 2: Provenance of the Yangtze delta sediments and its association with heavy precipitation area during the last 5 ky: the relationship between monsoon front migration and flood occurrence

2.1 Introduction

The East Asian Monsoon (EAM) is a phenomenon driven by a thermal contrast between the Asian continent and Pacific Ocean, and is subdivided into the East Asian Summer Monsoon (EASM) and the East Asian Winter Monsoon (EAWM). The EASM is characterized by a northwestward migration of its precipitation front from April to August, and exerting a significant influence on the hydrological cycle over East Asia (e.g. Wang and Lin, 2002; Ding and Chan, 2005; Wang et al., 2005; Tada et al., 2016).

Annually, emergence and movement of the EASM precipitation front is induced and limited by the movement of the westerly jet axis (Ding and Chan, 2005; Sampe and Xie, 2010). The axis of the westerly jet remains south of the Himalaya Mountains during winter to early spring, and jumps to the north of the Tibetan Plateau during April to May, when the EASM precipitation front appeared in the Indochina Peninsula. This is followed by the northern penetration of the precipitation front during April to August (Schiemann

et al., 2009; Sampe and Xie, 2010). Then the westerly jet axis retreats to the south of the Himalaya Mountains during autumn, which is accompanied with the southward retreat of the precipitation front (Schiemann et al., 2009). It is also pointed out that the position of the westerly jet axis bounds the northern limit of the EASM precipitation front (Sampe and Xie, 2010).

Based on the meteorological observations, the intensity of EASM can be defined either by the intensity of convection, precipitation, or wind speed (Wang et al., 2008; Ding et al., 2008; Zhang et al., 2008; Yim et al., 2014). Comparison of the observed precipitation with the strength of convection over East Asia, which is considered as reflecting the intensity of EASM, indicates that the summer precipitation in the North China (north of the Huai River) increase during the period when convection over East Asia becomes stronger and that the summer precipitation in the South China (south of Huai River) increases during the period when convection in East Asia becomes weaker (Ding et al., 2008; Wang et al., 2012). Thus, the intensity of EASM is manifested as the degree of northwestward penetration of the summer precipitation front into the inland China.

Various proxies have been used to reconstruct the EASM precipitation in the past before instrumental records, because it has been considered as reflecting the intensity of EASM. Examples are the oxygen isotope of the stalagmite (e.g. Wang et al., 2005; Hu et al., 2008;

Cai et al., 2010) from South China, the oxygen isotope ratio of carbonate in lake sediments (e.g. compiled by Zhang et al., 2011), the lake level (e.g. An et al., 2000), the pollen assemblage (e.g. An et al., 2000; Chen et al., 2015), and the thickness and density of tree-ring records (e.g. Yi et al., 2012). However, since the drainage area of the sampling sites in these studies are small, these proxies tend to reflect the local precipitation, and an attempt to reconstruct the past spatial distribution of precipitation in East Asia in the geological past were limited to a few studies (e.g. An et al., 2000; Nagashima et al., 2013). In addition, the vapor source changes could affect the oxygen isotope ratios of stalagmites and lake sediments (Hu et al., 2008; Maher and Thompson, 2012).

The variability of EASM intensity is associated with changes not only in the distribution of precipitation, but also in the frequency of the heavy rain. Wang et al. (2012) pointed out that the precipitation in the northwestern part of the Yangtze drainage basin decreased in association with the weakening of EASM intensity, whereas the frequency of heavy rain increased, based on the observational precipitation records. In the Yangtze drainage basin, the occurrence of heavy rain is important because it could induce floods, and triggering the hazards. Nevertheless, the area where flood occurred in the past is not clear especially beyond 500 yrs, because of the lack or uncertainness of historical records (Jiang et al., 2006; Shen et al., 2007). In addition, the correlation between the occurrence

of floods and the movement of EASM precipitation front have never been directly examined before the meteorological observation.

In this chapter, I first (i) reconstruct the spatio-temporal variability of EASM precipitation during the last 5 ky to monitor the behavior of the EASM precipitation front, and then (ii) examine the relationship among the movement of the EASM front, frequency of floods, and changes in flood-causing area, based on the provenance study of quartz in the fine-silt fraction of the core sediments recovered from the subaqueous Yangtze delta.

2.2 Oceanographical and sedimentological settings

2.2.1 Oceanographical settings

East China Sea (ECS) is a marginal sea located on the eastern margin of Asian continent. It is surrounded by Eurasian continent, Kyusyu Island, Ryukyu island arc, and Taiwan Island (Figure 2.1). The major surface water mass in the ECS are Chinese Coastal Current (CCC), Changjiang Diluted Water (CDW), Taiwan Warm Current (TWC), and Kuroshio Current (KC) (Figure 2.1; Liu et al., 2007; Zhang et al., 2007). CCC includes Jiangsu Coastal Current (JCC) flowing southward into ECS from the Yellow Sea along the coastline of East China and Zhejiang-Fujian Coastal Current (ZFCC) flowing

southwestward along the coastline of East China to the Taiwan Strait, and transports the suspended sediments discharged from the Yangtze River to the inner shelf of ECS along the coastline (Figure 2.1; Liu et al., 2007). CDW is formed by mixing of flesh water discharged from the Yangtze River and saline sea water, and characterized by lower salinity and lower temperature compared to TWC and KC (Ichikawa and Beardsley, 2002; Zhang et al., 2007). CDW composes an eastward-flowing plume over the shelf of East China Sea during summer when the water discharge from the Yangtze increases (Naimie et al., 2001; Zhang et al., 2007).

2.2.2 Sedimentological settings

ECS has a wide continental shelf of 0.75×10^{12} m^2, and receives a large amount of terrigenous materials (Liu et al., 2007). In the 20th century, the Yangtze River and the Yellow River are two major sources of the sediments to the ECS, having supplied 480 Mt/yr and ~1000 Mt/yr, respectively (Chen et al., 2001; Yang et al., 1998). It is estimated that about a half of the sediment discharged from the Yangtze deposit around the subaqueous Yangtze delta area, while the remaining sediments are transported southwestward by ZFCC and deposited in so called Mud Belt developed along the coastal line (Liu et al., 2007).

The initiation of formation and progradation of the Yangtze delta have been studied by

many researchers (e.g. Chen and Stanley, 1993; Li et al., 2000; Saito et al., 2001; Hori et al., 2001; Liu et al., 2010; Song et al., 2013). According to these studies, the Yangtze delta has developed over the valley incised during the late Pleistocene since the end of the Last Glacial Maximum (LGM) (Li et al., 2000, Hori et al., 2001; Xu et al., 2016). The Yangtze rivermouth was located around Zhenjiang City at 7 ka, when the water level became stable after the continuous sea level rise since the LGM (Figure 2.2; Hori et al., 2001; Liu et al., 2004). Based on stratigraphy and radiocarbon dating in many subaerial boreholes, it is suggested that the subaerial Yangtze delta advanced to the southeast during the last 7 ka, which was accompanied with the movement of rivermouth sand bars (Figure 2.2; Li et al., 2000; Hori et al., 2001; Song et al., 2013). Especially, the progradation rates after 2 ka became two times faster than the rate before 2 ka due to human activity (Hori et al., 2001).

In the subaqueous Yangtze delta, the sequence of sedimentary facies since the end of the LGM were compiled by Xu et al. (2016), based on seismic profiles, sedimentary facies of subaqueous boreholes, and the radiocarbon ages of shell fossils and foraminifera (Figure 2.3 and 2.4a). The sequence is composed of the early transgressive system tract (E-TST), the late transgressive system tract (L-TST), the early highstand system tract (E-HST), and the late highstand system tract (L-HST), respectively, in ascending order

(Figure 2.4a; Xu et al., 2016). E-TST is overlying pre-LGM deposits, characterized by fluvial facies during the initial period of sea level rise from 19 ka to 12 ka (Xu et al., 2016). L-TST is characterized by tidal flat to shallow marine facies with occasional mud ridge, and deposited during 12 to ~7.5 ka (Chen et al., 2003; Xu et al., 2016). E-HST is characterized by prodelta facies and its thickness thins southeastward because sediments were supplied from the Yangtze rivermouth which was located to the northwest of the delta, and deposited during ~7.5 to ~2 ka (Xu et al., 2016). L-HST is characterized by estuary front–shallow marine facies and the increased sedimentation rates compared to those of E-HST, and deposited after 2 ka (Xu et al., 2016). The mud belt is also assumed to have been formed during the last 7 ka, following the progradation of the Yangtze delta (Liu et al., 2007).

2.3 Material and Method

2.3.1 Drilling of YD13 cores

YD13 cores were drilled in July 11 to 12, 2013 by a ship named Kan 407. The YD13 drilling site is located in the subaqueous part of the Yangtze delta about 100 km southeast of the modern Yangtze rivermouth (Figure 2.5a). Coring was conducted in three drilling

holes using the hydro-pressure drilling machine HGD-600 with an inner tube of 1.2 m in length and 74 mm in diameter. In addition, three gravity cores were taken at sites close to the drilling site in order to cover the uppermost part of the near surface sediments, using a gravity corer DYS-1 with an inner tube of 3~4 m in length and 105 mm in diameter. The coordinate, water depth, and length of the drilling cores and the gravity cores are listed in Tables 2.1, respectively. The detailed position of all the sites are shown in Figure 2.5b. The two drilling holes named Hole 1 (H1) and Hole 2 (H2) are composed of 43 and 10 cores, respectively. The drilling depth indicates the depth from which each core is recovered in each hole and is defined in each hole independently. The drilling depth of each core is based on the drilling records by drillers on ship, and the drilling depth of upper 10 cores of each hole are listed in Table 2.1. The average core recovery of Hole 1 and Hole 2 are 86.5 %, 92.3 %, respectively. The gravity core of G2 has length of 1.42 m. On the drilling ship, the recovered sediment cores were wrapped with a plastic film and a canvas cloth, sealed with wax, and put into the core liners with a wooden plug and vinyl cap. These cores were transported to Nanjing Normal University immediately after the cruise, stored in the refrigerator at 5 °C, and kept unopened by the time of sub-sampling.

2.3.2 Sub-sampling

Sub-sampling of cores from Hole 1, Hole 2, and G2 was conducted in July 20 to 23, 2013 and October 9 to October 19, 2013 at Nanjing Normal University. First, the outer canvas of each core was cut by a cutter knife, then the core sediment in a core liner was split into two halves using GEOTEK core splitter, and each split half was moved to a half cut vinyl tube. The core at the top was numbered as Core 1, then after the number of core were increased downward. Core 1 of Hole 1 to Core 10 of Hole 1 were split in the darkroom for sampling of sediments used for optically stimulated luminescence (OSL) analysis (Sugisaki et al., 2015). As to the sediments from Hole 1, and Hole 2, one of the split half of each core (a sampling half) was used for sub-sampling, while the other half (an archive half) was used for the image scanning, visual core description, and color measurement as will be described later. An archive half was put into a semi-transparent plastic tube, vacuume-sealed, and stored in the refrigerator as an archive. As to the sediments from G2, both halves of the core were used for sub-sampling.

The sampling plan for each holes is shown in Figure 2.6. Samples for OSL dating were taken from Core 1 to 10 of Hole 1, using two pairs of aluminum L-channels with 15 mm width based on LL-channels sampling method by Nakagawa and Suigetsu 2006 Project Members (2014).

Slab samples for the Soft-X ray radiographs were taken from cores of Hole 1, Hole 2, and

G2, using a plastic case of 200 mm long × 50 mm wide × 10 mm thick. Slab samples were basically taken from the center of the sampling half, except Core 1 to 10 of Hole 1 for which slab samples were taken from the center of archive half, because the center of sampling half of these cores were taken for OSL analysis.

Samples for ESR and CI analysis were taken from Holes 1 and 2, using two pairs of LL-channels with 15 mm width. For Hole 2, one pair of LL-channel sample were taken additionally for radiocarbon dating.

The remaining sediments of the sampling halves were cut into a fixed interval as sample for additional analysis. The intervals were 2 cm for Hole 1, 5 cm for Hole 2, 1 cm for the upper 50 cm of G2, and 2 cm for the rest of G2. The top 50 cm of G2 with 1 cm interval were taken for the dating using excess ^{210}Pb and ^{137}Cs method by Dr. Irino of Hokkaido University. Samples for ESR and CI analysis of G2 were taken from these backup samples.

The LL-channel and slab samples were put into an aluminum-coated bag, and vacuum-sealed. Then, all samples were transported to the University of Tokyo, and stored in the refrigerator at 5 ℃.

2.3.3 Image scanning and visual core description

Image scanning, visual core description (VCD), and color measurement were conducted

during sub-sampling at Nanjing Normal University. After the core splitting, the surface of an archive half was scanned using an image scanner EPSON GT-8500. One scanned image covers a 25 cm interval of each core, and images of each core were compiled into a single image of each core.

VCD was conducted following image scanning. The sediment type, sedimentary structure, sediment color, and occurrence of sand layers were described in VCD.

2.3.4 Water content

Water content measurements of Holes 1 and 2 samples were conducted at the University of Tokyo in May 2014 and July 2014, respectively. Before the time of water content measurement, samples were stored as LL-channel samples in a vacuum-sealed plastic tube, and put in the refrigerator to prevent degradation of organic matter and the evaporation of water from samples during the storage. Water content measurements of G2 samples were conducted at the Hokkaido University in June 2014. LL-channel samples stored in a refrigerator for ~1 year were sliced at 2 cm interval for Holes 1 and 2, and 1cm interval for G2 samples. Sliced samples of ~2 g each were weighted in wet condition, freeze-dried, and weighted again after freeze drying. Water content of each sample was calculated as the difference in weight before and after drying divided by the weight before drying, and expressed in percent. The absolute error of water content

including measurement and calculation are less than 3 % based on the repeated measurement for the same sample.

2.3.5 Soft-X ray radiograph

To observe sedimentary structures of the core sediments, Soft-X radiograph of the slab samples were taken on May 2014, using SOFTEX CMB-2 at the University of Tokyo. The X-ray irradiation condition was 30 kVp of voltage, 2 mA of current, and 1.5 minutes of exposure time. The images were captured by IP-card, read by Fuji Photo Film Co. Ltd. FLA-7000 as RAW format image on the computer. A RAW format image include Soft-X ray radiographs of three slabs, then trimmed to TIFF format images on each slab. Soft-X ray radiographs of trimmed slabs from a single core were combined into a single image on the computer.

2.3.6 Radiocarbon dating

To construct an age model of YD13 cores, AMS radiocarbon dating was conducted on shell fossils, benthic foraminifera, and particulate organic carbon (Table 2.2). After washing out the clay- to silt-sized grains through a mesh with 64 μm opening, both shell and foraminifera fossil samples were picked out one by one using a paintbrush. Then, shell and foraminifera fossil samples were washed by deionized water and dried prior to the pretreatment for the radiocarbon dating. The species of shell fossils were identified

by Prof. Sasaki, the University Museum, the University of Tokyo. The shell fossils found in YD13 cores include bivalves *Arcosis interplicata,* and snails *Zeuxis succinctus, Zeuxis castus, Pristiterebra pumilio,* a kind of Scaphopoda, and a kind of Conidae. Except Scaphopoda and Conidae whose genus could not be specified, the spicies of *Arcosis interplicata*, *Zeuxis succinctus*, *Zeuxis castus,* and *Pristiterebra pumilio* mainly live in a muddy inner bay environment.

Sample pretreatment and AMS radiocarbon dating were conducted at National Institute of Environmental Science, Japan (NIES) under the guidance of Dr. Uchida. The carbonate samples of 2~3 g, including shell and foraminifera fossils, were put into the discrete plastic centrifuge tube, soaked overnight in 10 % hydrogen peroxide to decompose the organic matter, and dried again. The dried carbonate samples were weighted so that carbon content exceeds 4 mg, and put into a stainless cup with a diameter of ~ 5 mm, which were washed by acetone beforehand. The stainless cups with samples were put into glass tubes with phosphorous acid free of water. To let samples react with phosphorous acid in a vacuum, the remaining atmosphere within the tube was vacuumed to 2 Pa, then the upper part of the tube was burn off to seal. After evacuation, the carbonate samples were reacted with phosphorous acid to form CO_2 gas. CO_2 gas from samples are isolated into another glass tube using dry ice-ethanol and liquid nitrogen to remove other gases

such as water, and burned off to seal.

2.3.7 ESR signal intensity and Crystallinity Index of quartz, and Quartz content analyses

As parameters to characterize provenance of the detrital material in YD13 cores, ESR signal intensity and Crystallinity Index (CI) of quartz, and Quartz Content (QC) in three size fractions were analyzed. One hundred sixty three samples were selected from Hole 1, Hole 2, and G2, to cover the last 6 ky based on the age model that is described later. Samples were pretreated, separated into <4 μm, 4-16μm, and >16μm fractions, and analyzed for ESR signal intensity, CI, and QC in the same ways as was described in Section 2 of Chapter 1. As was discussed in Chapter 1, the fine-silt (4–16μm) fraction is assumed as representative of the SPM discharged from the Yangtze River. Thus, in this chapter, the fine-silt fraction will be used for the provenance study of YD13 cores.

2.4 Lithological description and lithostratigraphy

2.4.1 Lithological description based on macroscopic and Soft-X ray

radiograph observations

During macroscopic observation on the split surface of an archive half, several information on sediments such as sedimentary structures, grain size, thickness of sand layers, and occurrence of shell fossils were described during the VCD.

On the basis of the VCD and scanned images of split core surface, YD13 sediments are mainly composed of gray muddy silts. In addition, many millimeter-scale coarse-silt to sand layers are observed on the Soft-X ray radiographs. Because Soft-X radiograph is negative, brighter appearance of the image indicate lower transmittance of Soft-X ray, which generally suggests higher wet bulk density due to lower water content caused by larger grain size or more compaction, while darker appearance is attributed to lower wet bulk density due to higher water content caused by higher clay content or less compaction. The definition, nature, and categorization of the coarse-silt to sand layers observed on the Soft-X ray radiographs are described below.

2.4.1.1 Coarse-silt to sand layers

The coarse-silt to sand layers, which consist dominantly of coarse-silt to sand grains, are observed during VCD and also identified as the bright layers on the Soft-X radiographs, corresponding to the sediments with lower water content compared to the adjacent parts of the sediments. To interpret the origin of these layers in YD13 sediments, these layers

are described and categorized into three types, Type A, B, and C based on their brightness on Soft-X ray radiographs, water content, and sedimentary structures. Both darkness on Soft-X ray radiographs and water content are considered as dominantly reflecting grain size. Sedimentary structures include sharpness of the bottom boundary and the upward grading. Figure 2.8 shows the typical coarse-silt to sand layers of Type A, B, and C, respectively. Type A layer is defined as a layer that is clearly recognized as a bright layer on the Soft-X ray radiograph, with the low water content compared to the adjacent sediment, good horizontal continuity, a sharp bottom boundary, and upward fining. Type B layer is defined as a layer that is recognized as a bright layer on Soft-X ray radiograph, with a sharp bottom boundary and upward fining, poor horizontal continuity on the Soft-X ray radiograph. Type C layer is defined as a layer that is recognized as an unclear bright layer on Soft-X ray radiograph without a sharp bottom boundary. Horizontal continuity and upward fining are less distinct in Type C layers.

2.4.1.2 Muddy silt sediments

Except the coarse-silt to sand layers, sediments of YD13 cores are composed of homogeneous mud to fine-silt. They are considered as the sediment which accumulated more or less continuously. Thus, I call these sediments as the background sediments below.

2.4.2 Water content

Figure 2.7 shows the water content profiles against drilling depths in YD13 Hole 1, Hole 2, and G2.

Water content of the cores from Hole 1 varies between 25.3 % and 42.6 % with an average of 37.8 %. The water content in Hole 1 decreases from 38.8 ± 1.85 % to 35.9 ± 1.94 at 6.2 m_drilling depth between Cores 6 and 7. Water content of Hole 1 also gradually decreases downward from 8.4 m_drilling depth (0.2 m below the top of Core 9) to 9.4 m_drilling depth (the bottom of Core 10) from around 37 % to 32 %.

Water content of the cores from Hole 2 varies between 25.0 % and 42.9 % with an average of 37.3 %. There is no clear decrease in water content approximately at 6.2 m_drilling depth where a decrease of ~3 % is observed in Hole 1. There is a decrease trend from around 37 % to 32 % between 7.8 to 9.2 m_drilling depth in Hole 2 Core 9 to Core 10.

Water content of G2 varies between 35.6 % and 45.5 % with an average of 40.3 %. The core is characterized by higher water content compared to both Hole 1 and Hole 2, and shows a clear decreasing trend downward from around 45 % to 35 %.

Water content at each hole of YD13 shows 10 cm-scale fluctuations of 1~2 % in amplitude and m-scale fluctuation of ~5 % in amplitude. In addition, intervals with low water

content around 30 % are observed, which correspond to frequent coarse-silt to sand layers such as at 5.2 to 5.3 m_drilling depth in Hole 1 and at 9 to 10 m_drilling depth in both Hole 1 and Hole 2. 2.4.3 Lithostratigraphy

On the basis of the frequency and types of coarse-silt to sand layers, the sediment of YD13 are divided into Units 1 to 4 in descending order as are described below.

2.4.3 Lithostratigraphy

2.4.3.1 Unit 1

Unit 1 is characterized by frequent occurrence of Type A, B, and C layers that are interbedded with gray homogeneous clayey silt. The frequency of coarse-silt to sand layers are ~20 layers/m and average water content of Unit 1 is 38.6 %. The base of Unit 1 in Hole 1 and 2 could be defined individually by the start of frequent coarse-silt to sand layers intercalations. The base of Unit 1 is defined by a 8 cm thick visible fine to medium sand layer at 5.21 to 5.29 m_drilling depth in Hole 1, and a couples of sand layers with 10cm thick in total at the interval of 6.97 to 7.07 m_drilling depth in Hole 2 (Figure 2.9). G2 did not reach to the bottom Unit 1. Thus, Unit 1 is defined from 0.00 to 5.29 m drilling depth in Hole 1, 0.00 to 7.07 m drilling depth in Hole 2, and includes the whole G2. Shell fossils, including both of well- and poorly-preserved ones, are relatively abundant especially near the bottom of Unit 1, while benthic foraminifera are rare in Unit 1.

2.4.3.2 Unit 2

Unit 2 is characterized by gray homogeneous clayey silt with relatively low water content with rare occurrence of coarse-silt to sand layers. Most of the coarse-silt to sand layers in Unit 2 are millimeter-thick and categorized as Type C. The frequency of coarse-silt to sand layer intercalations in Unit 2 is 6.3 layers/m in average, which is less than one third of Unit 1. The base of Unit 2 is defined by the last occurrence of the cm-thick, disturbed fine sand layers of Unit 3 on the Soft-X ray radiographs at 8.77 m_drilling depth in Hole 1. In Hole 2, the boundary between Unit 2 and Unit 3 was not recovered because it is located within a core gap between Core 9 and Core 10. Thus, Unit 2 is defined from 5.29 to 8.74 m_drilling depth in Hole 1, and from 7.07 to 8.49+ m_drilling depth in Hole 2. Water content in Unit 2 show a downward decreasing trend from ~37 % to ~32 % with relatively low amplitude variation of less than 5 % in 10 cm–scale, especially in Hole 1. Shell fossils occur only as small fragments and quite rare throughout Unit 2. It is not possible to identify their species names and living environments. On the contrary, benthic foraminifera are common throughout Unit 2, and most abundant in Cores 6 and 7 of Hole 1.

2.4.3.3 Unit 3

Unit 3 is characterized by cm-thick and disturbed coarse-silt to sand layers intercalated in

gray silt sediments. The coarse-silt to sand layers in Unit 3 have relatively low water content below 30 %, and their frequency is 10.8 layers/m in average. The basal boundary of Unit 3 is defined by the first occurrence of gray clayey silt, which is similar in appearance to clayey silt in Unit 1 to 3, at 9.67 m_drilling depth of Hole 2 (Figure 2.9). In Hole 1, Core 10 still contains the clayey silt, thus the basal boundary of Unit 3 is probably below the base of Core 10. Although Core 11 of Hole 1 was not opened in my sampling, the driller in the drilling ship observed that Core 11 of Hole 1 is mainly composed of gray fine sand, indicating that the basal boundary of Unit 3 in Hole 1 is considered as being located between Core 10 and Core 11. Thus, Unit 3 is from 8.74 to 9.64+ m drilling depth in Hole 1, and 8.49+ to 9.67 m drilling depth in Hole 2. In Hole 2, the bottom 25 cm of Unit 3 is highly disturbed before the drilling by the grayish and yellowish-gray fine sands. Unit 3 yields some shell fossils with poor preservation, while foraminifera are rarely found. The shell fossils yielded in Unit 3 are *Pristiterebra pumilio* and Conoidea. The living environment of the former is an inner bay, and that of the latter is unknown because it is difficult to identify to their species only by small fracments.

2.4.3.4 Unit 4

Unit 4 is below 9.7 m_drilling depth in Hole 1 and below 9.67 m_drilling depth in Hole 2. Unit 4 is composed of intercalating of gray fine sands and yellowish-gray medium

sands with gradual boundaries and rare occurrence of mm-thickness silty sand layers with the frequency of 2~3 layers/m. No shell fossil was found from Unit 4.

2.5 Inter-hole correlation and construction of a composite column

Because of the presence of core gaps between recovered cores, it is impossible to construct a totally continuous sedimentary column from a single borehole. This is why two holes are drilled with a slightly different depth interval in order to cover core gaps of each hole. In this section, I try to correlate the sediment cores in between Hole 1, Hole 2, and G2, to make a composite sediment column of YD13 site as continuous as possible.

2.5.1 Inter-hole correlation lithological unit, coarse-silt to sand layers in between Hole 1, Hole 2, and G2

Correlation among the three holes are conducted using key coarse-silt to sand layers that were correlated based on the similarity in lithological characteristics and water content profiles among holes under the constraints of the lithological correlation of the units.

As the first step for correlation, the lithological unit (Unit 1, 2, and 3) boundaries are used as the initial constraint on correlation (dashed lines in Figure 2.7). Because the

subaqueous Yangtze Delta has advanced during the last 7 ka, the similar lithological facies were formed in different ages in the different parts in the delta. However, because the distance between three holes are less than 100 m, the similar lithological facies could be assumed to be formed during the same period. Thus, the correlation among Hole 1, Hole 2, and G2 as described below are limited within the same lithological unit of each hole, whereas this limitation does not exclude the possibility that some part of each lithological unit in Hole 1, Hole 2, and G2 might lack.

As the second step, the meter-scale correlation among three holes are conducted on the basis of meter-scale fluctuation of water content as is shown by the grey shades in Figure 2.7. In Figure 2.7, the grey shades indicate which peaks of meter-scale fluctuation in the water content are correlated, and are drawn in the range where the trend of water content are same between two holes (Figure 2.7). The meter-scale minimum peaks of water content are shown as H1-1, H1-2, … , and H1-6 in Hole 1, H2-1, H2-2, … , and H2-8 in Hole 2, and G2-1 in G2. It is noted that the grey shades do not mean that the both sides of grey shades are exactly correlated in a centimeter-scale.

Because any eroded structure is not observed within each lithological unit in all of G2, Hole 1, and Hole 2, it is assumed that the sediment within each lithological unit is continuous in all of G2, Hole 1, and Hole 2. Namely, once one correlation between two

holes are established, This assumption means that the core gaps between adjacent cores in one hole could not expand to meter-scale within each lithological unit, and that the adjacent cores in one hole should not overlap in depth. This assumption indicated that, for example, once a core in a hole (for example, Hole 1) is correlated to a core in other hole (for example, Hole 2) based on the meter-scale peak of water content, the adjacent core in Hole 1 should be correlated to the adjacent meter-scale peak of water content in Hole 2.

As to Unit 1, comparing the water content at the top part of Hole 1, Hole 2, and G2, the water content at the top part of G2 shows highest value around 45 %, and a clear decrease trend downward to 40 %, while the water content in Unit 1 of Hole 1 and Hole 2 fluctuated around 35 to 40 % (Figure 2.7). Therefore, the top part of G2 with high water content up to 45 % seems not to be correspond to any part of Unit 1 in Hole 1 and Hole 2, and thus, G2 is assumed to occupy the top part of YD13 cores. Then, comparing fluctuation patterns of water content of G2 with those at the top few meter of Hole 1 and Hole 2, water content at the top part of Hole 2 and those at the bottom part of G2 shows similar fluctuation pattern, while water content at the top part of Hole 1 does not show a similar pattern. Namely, water content of Hole 2 from 0.0 to 0.4 m_drilling depth and water content of G2 from 0.6 to 1.0 m_drilling depth fluctuate around 40 % with a small amplitude within

±2 %, then drop to 33 % at 0.5 m_drilling depth in Hole 2 and 1.1 m_drilling depth in G2, and finally increase to 40 % at 0.8 m_drilling depth in Hole 2 and 1.4 m_drilling depth in G2. On the other hand, the top part of Hole 1 do not show such a fluctuation of water content in Hole 2 and G2, especially do not have a minimum peak around 33 % with broad width around 20 cm which are observed at 0.5 m_drilling depth in Hole 2 and 1.1 m_drilling depth in G2. Therefore, 0.5 m_drilling depth of Hole 2 and 1.1 m_drilling depth of G2 are assumed to correspond each other (grey shade (A) in Figure 2.7), while Hole 1 is assumed not to have a correlative part to the bottom part of G2 around 1.1 m_drilling depth. On the other hand, the bottom part of Core 1 of Hole 2 and the top part of Core 1 of Hole 1 show similar fluctuation of water content, which periodically changes 10 cm-scale with amplitude of 2 to 3 %, indicating that the bottom part of Core 1 of Hole 2 and the top part of Core 1 of Hole 1 are corresponding (grey shade (B) in Figure 2.7). Starting from this correspondence, each core in Hole 1 are correlated to cores in Hole 2 one by one toward the bottom of Unit 1, based on the meter-scale peaks of water content. Because the minimum peak of H1-1 and H2-2 is correlated as was described above, the minimum peak of H2-3 could correlated to the peak below H1-2. If the minimum peak of H2-3 is correlated to the minimum peak of H1-3, the overlap of Core 1 and 2 in Hole 1 will occur. Thus, the minimum peak of H2-2 should be correlated to the minimum peak

of H1-3. the minimum peak of H2-3 the because water content fluctuate with cycle of roughly 1 m, it is required for a core to shift by roughly 1 m in depth for changing the corresponding meter-scale peak of water content in the other hole. Therefore, under the constraint that there are no meter-scale gaps within Unit 1, the meter-scale correlation are limited as the gray shades as is shown in Figure 2.7.

As to Unit 2, the thickness of Unit 2 in Hole 2 (1.5 m) is thinner than that in Hole 1 (3.6 m). Under the assumption that sediments are continuous within the each lithological unit, as described above, it is suggested that either the top or bottom part of Unit 2 in Hole 2 lacks. As was described in the sedimentological settings, the system tract in the subaqueous Yangtze Deltas are composed of L-HST, E-HST, and L-TST from the sea floor. Based on the seismic profiles, it is indicated the E-HST are partly truncated by L-HST (Xu et al., 2016). Assuming that Unit 2 of YD13 cores correspond to E-HST, the lack of strata in Unit 2 might exist in the upper part of Unit 2 rather than in the lower part of Unit 2. Therefore, in the correlation between Hole 1 and Hole 2, Unit 2 in Hole 2 are correlated to the lower part of Unit 2 in Hole 1.

The uncertainness of meter-scale correlation can be estimated as the range of depth which each core can move. Each core can move in depth where the trend of the water content in both holes (grey shades in Figure 2.7) are same. Because the difference in thickness of

grey shades in Figure 2.7 are less than 20 cm in both holes, the maximum uncertainness of the meter-scale correlation are also estimated as less than 20 cm. In addition, the other constraints on the range of each core can move is that the trend of water content between two holes is same, and that the adjacent cores in the same hole do not overlap. As a result, the meter-scale correlation between G2, Hole 1, and Hole 2 are constructed as is shown in Figure 2.7.

As a final step, under the constraints of meter-scale correlation based on meter-scale variation of water content, the coarse-silt to sand layers, which are defined on the Soft-X ray radiographs, macroscopic observations, and water content, are correlated between G2 and Hole 2, and Hole 2 and Hole 1 to conduct their correlation with centimeter precision in between these holes. Under the uncertainness of meter-scale correlation as is shown in Figure 2.7, the centimeter-scale correlation between the coarse-silt to sand layers in each core are examined based on the Soft-X ray radiograph, sketch of split surface of the core, and centimeter fluctuation of water content (Figure 2.7). Because the coarse-silt to sand layers in the Soft-X ray radiograph are not necessarily clear and common among three holes, the other candidate correlation within the uncertainness of meter-scale correlation are also shown in Figure 2.7.

2.5.2 Construction of a composite column and definition of composite depth

A composite column of YD13 cores is constructed based on the inter-hole correlation described above. Based on the correlation described in the previous section, the top of G2 is defined as the top of the composite column. Using the correlation, cores of Hole 1 and Hole 2 are aligned with respect to the composite depth one by one from the top toward the bottom. There are six core gaps that cannot be filled by cores from the other holes. The width of core gap in a composite column is assumed to be the same as that in the drilling depth. Namely, from 2.78 to 2.79 m between Core 3 and Core 4 of Hole 2, from 4.62 to 4.69 m between Core 4 and Core 5 of Hole 2, from 5.92 to 6.05 m between Core 4 and Core 5 of Hole 1, from 7.90 to 7.96 m between Core 5 and Core 6 of Hole 1, from 8.75 to 8.86 m between Core 6 and Core 7 of Hole 1, and between 9.86 to 9.96 m between Core 7 and Core 8 of Hole 1. The composite column are shown in Figure 2.11.

G2 occupies the uppermost part of the composite column (Figure 2.11). The bottom ~50 cm of G2 overlaps with the uppermost part of Hole 2. The top of Hole 1 corresponds to ~0.8 m in the drilling depth of Hole 2.

Although the total thickness of Unit 1, 2, and 3 on the composite depth scale is similar between Hole 1 and 2, the thickness of each unit are different between Hole 1 and 2. The

total thickness of the sediment of Unit 1 in Hole 1 is 5.3 m, while that in Hole 2 is 7.1 m, 1.8 m thicker than in Hole 1. On the other hand, the thickness of sediments of Unit 2 in Hole 1 is 3.5 m, while that in Hole 2 is 1.3 m, 2.2 m thinner than in Hole 1. This is because of two large stratigraphic gaps at different composite depth; 0.94 m gap in Hole 1 between 7.0 to 7.9 m in the composite depth and 1.55 m gap in Hole 2 between 7.9 to 9.5 m in the composite depth. Hence, the total thickness of the sediment of Unit 1 plus Unit 2 are almost the same in both Hole 1 (7.7 m) and Hole 2 (7.9 m), and the top depth of Unit 3 in Hole 1 and Hole 2 are similar in the drilling depth. The bottom depths of Unit 3 in Hole 1 and Hole 2 are also similar at ~9.7m in the drilling depth, indicating that the thickness of Unit 3 is similar in both Hole 1 and Hole 2.

Based on the depositional age, Unit 2 and Unit 1 correspond to be the early highstand system tract (E-HST) and the late highstand system tract (L-HST) described in Xu et al. (2016). On the seismic profiles around the subaqueous Yangtze delta in Xu et al. (2016), the seaward thinning of the E-HST strata is observed commonly. Because Hole 2 was drilled deeper site (37 m in water depth) compared to Hole 1 (35 m in water depth), the difference in thickness of Unit 2 could be explained by the thickness change in the E-HST strata around the subaqueous Yangtze delta.

2.6 Construction of an age model

2.6.1 Radiocarbon dating

All the radiocarbon ages analyzed in this thesis is shown in Figure 12.

2.6.1.1 Shell fossils

In Unit 1, radiocarbon ages of eleven shell fossils range from 0.19 to 2.42 ka in the calendar age with the estimation error (95 %) of 0.09 ky. In Unit 2, shell fossils were not dated because they only occurs as small fragments in small amounts. In Unit 3, the radiocarbon ages of two poorly preserved shell fossils range from 5.09 to 6.25 ka with the estimation error (95 %) of 0.09 ky (Table 2.2).

2.6.1.2 Benthic foraminifera

The ^{14}C calendar ages of four benthic foraminiferal samples in Unit 2 range from 7.08 to 8.31 ka with an estimation error of 0.07 ky and they show an increasing trend downward from 7.53 to 9.28 m in the composite depth (Figure 12; Table 2.3).

Although there is no shell fossil date in Unit 2, ^{14}C calendar ages of benthic foraminifera in Unit 2 are entirely older than the ages of shell fossils in Unit 3, suggesting that benthic foraminifera in Unit 2 are of reworked origin, and that their radiocarbon ages likely

represent the depositional ages of reworked materials.

2.6.1.3 POC

The ^{14}C calendar ages of POC samples are listed in Table 2.7. The ages of POC samples in Unit 1 of Hole 1 range from 6.5 to 7.7 ka, showing no clear trend with depth and those in Unit 2 of Hole 1 range from 9.6 to 10.7 ka, also showing no clear trend with depth (Figure 2.12). The ages of POC samples from Unit 1 in Hole 2 range from 6.1 to 8.1 ka, and those from Unit 2 in Hole 2 range from 9.3 to 10.4 ka. The ages of POC samples of Hole 2 show increasing trend with depth throughout Unit 1 to Unit 3.

The ages of POC are older than those of shell fossils and benthic foraminifera taken from the same horizons by 4~5 ky and 1~2 ky, respectively. These age differences observed between POC and shell fossils are consistent with the age of 3 to 5 ka for POC in the modern surface sediments around the subaqueous Yangtze delta to the inner shelf of ECS (Li et al., 2012; Wang et al., 2013), but are much larger than the ages of 1 ka for POC sampled at the lower part of the modern Yangtze River (Wang et al., 2012).

The differences between the age for POC in the modern surface sediments around the subaqueous Yangtze Delta and those for POC in the lower Yangtze River are not well explained in the previous studies. One possible reason for this age difference is the rapid degradation of young and labile POC on the ocean floor and relative enrichment of old

and refractory organic carbon in the surface sediments (Marwick et al., 2015).

2.6.2 The age model based on the radiocarbon ages of shell fossils

Using the composite depth and radiocarbon ages of shells, an age model for YD13 was constructed (Figure 2.12). This age model is made by connecting the youngest shell fossil ages. Age points that makes age reversal with depth are discarded. Around 2.5 and 3.9 m of the composite depths, the ages of poorly-preserved shells tend to be older than those of well-preserved shells by 0.5~0.7 ky (Figure 2.12). Because the age model of Unit 2 is only constrained by shell fossils at the top and bottom of it, there is uncertainness of the age model in Unit 2. Considering that the sedimentation rate after 2 ka are commonly higher than the sedimentation rate before 2 ka around the subaqueous Yangtze Delta, it is estimated that the sedimentation rate in Unit 2 of YD13 increased toward the top of Unit 2. In fact, the averaged linear sedimentation rate in Unit 2 (1.22 m/ky) is higher than that in Unit 3 (0.66 m/ky) and lower than that in Unit 1 (3.9 m/ky) (Figure 2.12). Thus, the depositional age of Unit 2 is estimated to exist in the grey shade in Figure 2.12 and this range is used as an uncertainness of the depositional age in Unit 2 at this moment.

The radiocarbon ages of benthic foraminifera in Unit 2 are not used in this age model,

because they are older than the age of a shell fossil in underlying Unit 3.

In this age model, the depositional age is older than 5.1±0.1 ka in Unit 3, from 5.1±0.1 to 2.3±0.1 ka in Unit 2, from 2.3±0.1 to 1.2±0.1 ka in the lower part of Unit 1 below 3.3 m in the composite depth, and younger than 1.2±0.1 ka in the upper part of Unit 1 above 3.3 m in the composite depth.

2.7 Results

2.7.1 Sedimentation rate

Based on the thickness of sediments in the composite column and the shell-based age model, the linear sedimentation rates for each lithological unit was calculated (Figure 2.13a). The average sedimentation rates were 0.06 cm/yr for Unit 3, 0.12 cm/yr for Unit 2, and 0.38 cm/yr for Unit 1. Within Unit 1, the sedimentation rates were 1.7 cm/yr from 7.8 to 5.1 m in the composite depth during 2.3 to 2.1 ka, 0.2 cm/yr from 5.1 to 3.3 m during 2.1 to 1.3 ka, and 0.3 cm/yr above 3.3 m in the composite depth after 1.3 ka. During the last 6 ka, the sedimentation rates increased in Unit 1 after 2.2 ka, especially from 2.2 to 2.1 ka during 7.8 to 5.1 m in the composite depth.

2.7.2 Coarse-silt to sand layer frequency

Based on the shell-based age model, the coarse-silt to sand layer frequency was calculated as the total number of the coarse-silt to sand layers within the 200-yr moving window (Figure 2.13b). In this calculation, the coarse-silt to sand layers of only Type A and Type B were used, because they have a sharp bottom boundary and seem to be resulted from episodic sedimentation. Since there are only a few Type A and Type B layers in Unit 2, the frequency of coarse layers show only low value of less than 5 layers / 200 yrs during 4.0 to 3.5 ka. In Unit 1, the frequency of coarse layers have a sharp maximum of 30 layers / 200 yrs between 2.3 to 2.0 ka, then go down to the minimum of 3 layers / 200 yrs, and gradually increased toward 0.8 ka with some fluctuation.

2.7.4 Changes in the ESR signal intensity and CI values in the YD13 sediments

In Chapter 1, it was shown that quartz in the sediments discharged from the different parts of the Yangtze drainage basin have different ESR signal intensity and CI (Figure 1.9), and that the fine-silt fraction of the riverbed sediments could represent the SPM discharged from the Yangtze. It was also demonstrated that changes in major sources of SPM within the Yangtze River basin can be detected by analyzing the ESR signal intensity of quartz

in the fine-silt fraction. Thus, the ESR signal intensity and CI of quartz in the fine-silt fraction of YD13 sediments were analyzed to monitor changes in the provenance of detrital grains carried as SPM, which is expected to reflect changes in distribution of summer precipitation in the Yangtze River basin. Figure 2.14 shows the changes in the ESR signal intensity and CI of quartz in the fine-silt fraction in the YD13 core sediments. Because the thickness of the coarse layers varied from mm to cm-scale, some of samples for the ESR analysis may contain both the coarse-silt to sand layers and the background sediments. To evaluate the contribution from the coarse-silt to sand layers to the provenance of the background sediment in a sample, the analyzed samples are categorized into three classes: coarse-silt to sand layer sediments, coarse-silt to sand layer-bearing sediments, and the background sediments. The coarse-silt to sand layer sediments indicate samples which contain either Type A or Type B layers more than a half. The coarse-silt to sandy layer-bearing sediments indicate samples which contain either Type A or Type B layer less than a half and also contain the background sediments. Background sediments indicate samples is composed exclusively of gray clayey silt.

2.7.4.1 Changes in the ESR signal intensity and CI values of the background sediments

During the last 7 ky, the ESR signal intensity and CI of the background sediments in

YD13 varied from 2 to 15, and from 7.5 to 8.8, respectively (Figure 2.14).

The ESR signal intensity tends to show high values between 4 and 16 with high amplitude variation before 4.1 ka, gradually decreases around 5 during 4.1 to 2.3 ka, shows a maximum peak around 15 with high values during 2.3 to 2.1 ka, gradually increases during 2.0 to 1.2 ka, slightly decrease to 5 during 1.2 to 0.7 ka, increase to 15 during 0.7 to 0.4 ka, and slightly decreases after 0.4 ka. CI value shows medium values with high amplitude variations between 0.2 and 8.6 before 1.1 ka, shows high values up to 8.8 during 1.1 to 0.8 ka, and decreases to around 8 after 0.8 ka (Figure 2.14).

2.7.4.2 Changes in the ESR signal intensity and CI values of quartz in the coarse-silt to sand sediments and coarse-silt to sand layer bearing sediments

In Unit 2, the ESR signal intensity of coarse-silt to sand layers bearing sediments tend to be low <5 and CI of those layers are medium from 8.2 to 8.6. There is only one sample of coarse-silt to sandy layer sediments in Unit 2, and its ESR signal intensity and CI are 10 and 7.9, respectively.

In Unit 1, the ESR signal intensity of the coarse-silt to sand layer sediments show large fluctuation between 5 and 12 from 2.3 to 1.8 ka, low values around 5 from 1.1 to 0.9 ka, and high values over 12 after 0.6 ka. CI of these sediments increase to high values of 8.7 from 2.3 to 1.5 ka, then decrease to low values of 8.1 after 1.5 ka. The ESR signal intensity

of the coarse-silt to sand bearing sediments stably show high values between 7 and 12 throughout Unit 1. CI of these sediments show high amplitude variation between 8.1 and 8.8. Thus, it seems that the changes in provenance are notable in the coarse-silt to sandy layer and coarse-silt to sandy layer bearing sediments.

2.8 Discussion

2.8.1 Correlation between the flood layers at YD13 site and historical records of floods in the Yangtze River

2.8.1.1 The origin of the coarse-silt to sand layers in YD13 sediments

According to previous studies of the sediment cores from the subaqueous Yangtze Delta, sand layers were detected in core sediments, which were deposited during the last hundreds to thousands of years in the subaqueous delta facies (Wang et al., 2010; Hu et al., 2014), In their studies, the sand layers are interpreted as reflecting flood events based on comparison with the historical flood records (Wang et al., 2010; Hu et al., 2014). At YD13 site, there are also many coarse-silt to sand layers in Unit 1. Especially, the Type A and Type B layers show a sharp basal boundary and upward fining, therefore it is likely

that these two types of layers were deposited during the flood events. To confirm whether the Type A and Type B layers in the YD13 core sediments represent flood events in the past, the occurrence and frequency of the Type A and Type B layers are compared with that of the historical floods record.

2.8.1.2 Correlation between the coarse-silt to sand layers and the historical record of floods

To examine the similarity in temporal change in frequency in temporal change in frequency between the occurrence of the Type A and Type B layers and the historical flood events, timings of both the Type A and Type B layers are compared with timings of the historical floods records in Figure 2.15. The historical floods record are based on the compilation by Wang et al. (2010). Figure 2.15 also shows the frequency of the Type A and Type B layers and the historical recorded floods at every 100 yr, respectively.

In Figure 2.15, both the Type A and Type B layers and the historical floods occurred frequently during 2.3 to 2.1 ka (peak E). During 2.1 to 1.2 ka, both the frequency of the Type A and Type B layers and the historical recorded floods have a peak around 1.5 ka (peak D), although the Type A and Type B layers also has a peak around 1.9 ka. During 1.2 to 0.8 ka, both the Type A and Type B layers and the historical floods records occurred every few decades and the frequency of both the Type A and Type B layers have a peak

around 0.8 ka (peak C). During 0.8 to 0.6 ka, the Type A and Type B layers occurred almost every decades, while the occurrence of the historical floods records lacks during the same period. After 0.6 ka, the historical floods record occurred constantly and its frequency increased toward the top, while the Type A and Type B layers occurred around 0.5 and 0.3 ka. Throughout the last 2.3 ka, both the Type A and Type B layers and the historical floods records have a peak around 2.1 ka (peak E) and gradually increase toward 0.5 ka with several peaks at every 300 to 400 yrs, showing a similar pattern of fluctuation, As to the period from 1.2 to 0.8 ka, the frequency and occurrence of the Type A and Type B layers are similar to those of the historical recorded floods, indicating that these layers could record the floods during this period. During 2.3 to 1.2 ka, the frequency of the Type A and Type B layers are larger than that of the historical flood record, although both the occurrence of the Type A and Type B layers and the historical flood record show a similar pattern that decreased at 2.1 ka (Figure 2.15).

There are many studies about the occurrence of the floods or droughts within the Yangtze Basin using the historical documents, whereas these studies were mostly limited to the last 600 to 1000 yrs due to the lack of the reliable documents (e.g. Jiang et al., 2006; Shen et al, 2007). Thus, the historical flood record could gradually become incomplete as the age becomes old. It is possible the Type A and Type B layers to preserve the occurrence

of floods better than the historical documents especially before 1.2 ka when the occurrence of the historical recorded floods becomes rare. On the other hand, after 0.5 ka, the Type A and Type B layers lacks around 0.4 and 0.2 ka, and their frequency is less than that of historical recorded floods. However, during the last 0.5 ka, there are many Type C layers without the horizontal continuity and these discontinuity could be explained by disturbance during the coring. Considering that the composite section during the last 0.5 ka is covered by a gravity core G2, it is possible that the coring method effects on the preservation of the coarse-silt to sand layers.

In summary, the Type A and Type B layers in YD13 core seem to represent the flood events within the Yangtze basin at least during 2.3 to 0.5 ka, while the historical flood records seems to be reliable compared to the Type A and Type B layers in YD13 core at least during the last 0.5 ka. Combining the Type A and Type B layers in YD13 and the historical recorded floods, the frequency of floods within the Yangtze River is high from 2.3 to 2.1 ka, drop around 2.0 ka, gradually increase toward the modern with several peaks at every 300 to 400 yrs (Figure 2.15).

2.8.2 Possibility of reworking of fine-silt sediment and estimation of the source and the contribution ratio of the reworked materials

In Section 2.6, the depositional age model of YD13 core is constructed based on the radiocarbon age of the shell fossils. On the other hand, OSL ages of quartz in YD13 core by Sugisaki et al. (2015) tend to give older ages than those based the shell-based age model at the same horizon (Figure 2.12). In Unit 2, the depositional age is constraint by the shell-fossil radiocarbon ages of 5.1 and 2.3 ka at the bottom and top of the unit, respectively, while OSL ages of the fine-silt-sized quartz in Unit 2 show the ages from 6.8 to 5.4 ka, all of which are older than those of shell-based ages by up to 3 ky (Figure 2.12; Sugisaki et al., 2015). In Unit 1, the depositional age is constraint by the shell-fossil radiocarbon ages of 2.3 and 0.2 ka at near the bottom and the top of the unit, respectively, while OSL ages of the fine-silt-sized quartz in Unit 1 show the ages from 3.2 to 1.9 ka, which are older than those of shell-based ages by up to 2 ka (Figure 2.12; Sugisaki et al., 2015).

Sugisaki et al (2015) also showed that the SPM in the near surface water of the modern Yangtze River under the normal condition during summer at night was completely bleached by the sunlight during or immediately before transportation. Thus, the OSL ages of quartz in the fine-silt fraction of the sediments around the Yangtze delta are considered as reflecting the age when the quartz particles were discharged from the Yangtze, although there is a possibility that quartz in SPM was not completely bleached in the deeper part

of the river and/or during floods. If I accept the assumption that quartz in SPM discharged from the Yangtze was completely bleached even in the deeper part of the river and during floods, the OSL ages which are older than the shell-fossil ages of the same horizon should reflect contribution of the reworked quartz grains during deposition on the sea floor from older sediments grains in addition to quartz grains directly discharged from the Yangtze, because the OSL ages are based on analysis of multiple grains. If so, the difference between the OSL ages and the depositional age estimated from the shell-based age model should provide information on the contribution of sediments reworked from the older sediments.

In this section, the origin of the reworked material are discussed first, then I attempt to evaluated and subtract the effect of the reworked material on the ESR signal intensity of the analyzed sediments of YD13 based on the estimating contribution ratio of reworked materials.

2.8.2.1 Provenance and age of the reworked sediments

Unit 2

Unit 2 is characterized by abundant occurrence of benthic foraminifera whose radiocarbon ages range from 8.3 to 7.0 ka (Figure 2.12). The older radiocarbon ages of benthic foraminifera in Unit 2 relative to the estimated depositional ages based on the

shell fossils (Figure 2.12) also support that the benthic foraminifera in Unit 2 were reworked from older sediments with depositional age of 7.0~8.3 ka. The radiocarbon ages of benthic foraminifera were acquired from a single genius *Quinqueloculina sp.*, whose living environment is shallow marine from 10 to 50 m in water depth. Because the density of foraminifera skeleton is smaller than that of detrital grains such as quartz due to the pore space in their skeleton, it is possible that the reworking process also transported finer detrital materials together with foraminifera skeleton. Thus, it is estimated that the origin of the reworked materials are a shallow marine sediments whose depositional age from 8.2 to 7.0 ka.

Xu et al. (2016) compiled the seismic profiles, sedimentary facies, and radiocarbon ages of the subaqueous Yangtze delta and discussed its development process. According to their classification of sedimentary facies in the subaqueous Yangtze Delta, sediments deposited between 8.2 and 7.0 ka, the radiocarbon ages of benthic foraminifera in Unit 2 of YD13 cores, correspond to late transgressive system tract (L-TST), which is estimated to have formed during the later period of sea level rise after the Younger Dryas cold reversal (11.7 ka; Xu et al., 2016). Based on several seismic profiles and lithology of previously studied sediments cores that were obtained from in the subaqueous Yangtze delta, it is shown that L-TST are mainly distributed at the water depth of around 30–60 m

under the modern sea level condition, and characterized by silt to clay sediments forming horizontal to slightly seaward-dipping strata (Xu et al., 2012, 2016; Figure 2.3 and 2.4a). Although there still is a discussion on the sea level change around the Yangtze delta since the LGM, the sea level around the Yangtze delta during the last 5 ky is estimated to have been within ±5 m of the present sea level (Song et al., 2013; Liu et al., 2010), indicating that the water depth at YD13 site during the last 5 ky were between 35 m and 50 m.

On the seismic profiles, the L-TST strata are truncated by the early highstand system tract (E-HST) that were deposited during 7–3 ka near the Yangtze rivermouth (Xu et al., 2016). On the other hand, in the offshore side of the YD13 sites, absence of the E-HST strata due to the hiatus after 7 ka are observed and the L-TST strata are currently exposed on the sea floor around the water depth of 40–60 m (Chen et al., 2003; Xu et al., 2016; Figure 2.4a). These absence corresponding to the upper part of L-TST due to a less sediment supply indicate the post-depositional erosion by tidal or storm processes in this area (Wang et al., 2005). Thus, it is reasonable to consider that the benthic foraminifera in Unit 2 of YD13 cores were derived from the reworked materials from L-TST which are now exposed in the offshore side of the YD13 site.

Unit 1

In Unit 1, there are also the age difference between the depositional ages estimated from

the shell-based age model and OSL ages of quartz by up to 2 ky, suggesting the continuous contribution of the reworked materials (Figure 2.12). However, the rare occurrence of foraminifera in Unit 1 make it difficult to constrain the age of reworked materials. The rare occurrence of foraminifera in Unit 1 also suggest either that the source of reworked materials move to the place where occurrence of benthic foraminifera are rare, or that the increasing supply of SPM from the Yangtze River in Unit 1 dilute the contribution of the reworked materials and the occurrence of reworked benthic foraminifera.

Therefore, to constrain the source and age of the reworked materials in Unit 1, potential sources of the reworked materials in Unit 1 are selected and these potential sources are examined whether they fulfill the required condition as the reworked materials in Unit 1 as is discussed below. The reworked materials in Unit 1 are assumed to fulfill the constrains (1) they are mainly composed of clay to silt and (2) they rarely contain foraminifera. Considering that the along shore currents flow southward around the Yangtze Rivermouth (Figure 2.1), the potential source of the reworked materials to YD13 site is limited to either the Yangtze River basin, the Yangtze Delta, or the southwestern part of Yellow Sea to the north of the YD13 site. The potential sources which are located adjacent to YD13 site are shown in Figure 2.16.

Area I is in the subaqueous Yangtze Delta and was located between the YD13 site and the

Yangtze Rivermouth with the water depth of less than 30 m (Figure 2.16). ECS-0702 sediment core was recovered at 22 m water depth within this area (Liu et al., 2010). In ECS-0702 core, high sedimentation rate of around 5 m/ky was observed during the last 2.5 ka, and no unconformity was observed during the same period (Liu et al., 2010). Such high sedimentation rates were commonly observed around the subaqueous Yangtze Delta (Xu et al., 2016). In addition, it contains abundant benthic foraminifera (Liu et al., 2010). Thus, if sediments in Area I was the source, occurrence of the abundant foraminifera is expected in Unit 1. In addition, if the sediments in Area I were the source of the reworked sediments in Unit 1 of YD13, it is suggested that the contribution ratio of the reworked sediments from Area I should have been high because OSL ages of quartz in Unit 1 are close to the depositional age of sediments around Area I (~2.5 ka). However, foraminifera occurrence is rare in Unit 1. Moreover, Area I is covered by a thick L-HST strata up to 10 m that was deposited during the last 2ka, there is no evidence for erosion on the seismic profiles (Xu et al., 2016). Therefore, Area I does not seem to be the source of the reworked material in Unit 1.

Area II is the subaerial Yangtze Delta that has developed during the last 7 ka (Figure 2.2 and 2.16). Hori et al. (2001) studied the sedimentary environment and progradation of the Yangtze Delta during the last 8 ka using three boreholes recovered from the modern

subaerial Yangtze delta. Based on the sedimentary structure and their estimated depositional environment, Hori et al. (2001) categorized the sediments in three boreholes into six depositional units from Unit A to Unit F. Within these depositional units, only are Unit B and Unit D are mainly composed of silty to clayey sediments (Hori et al., 2001). At CM97 site near the modern Yangtze rivermouth, Unit B was deposited in a low-energy prodelta environment during 7 to 1.5 ka (Hori et al., 2001). Unit D was also deposited in inter- to sub-tidal flat environment after 1.5 ka and occupied the uppermost part of CM97 core (Hori et al., 2001). Considering the OSL ages in Unit 1 ranging from 1.9 to 3.2 ka in YD13 core, the depositional age of Unit D is too young to explain the OSL ages in Unit 1 and unlikely to be the source of reworked materials in Unit 1 of YD13. Unit B occupies 17 to 25 m of the modern water depth in CM97 core (Hori et al, 2001). However, in boreholes around the modern subaerial Yangtze delta, the sediment of Unit B are overlain by younger thick deltaic unit, and not exposed in the river channels (Li et al., 2000; Hori et al., 2001). Thus, Unit B are also unlikely to be the source of reworked material in Unit 1 of YD13.

Area III is the riverbed in the middle to lower reaches of the Yangtze mainstream (Figure 2.16). Based on the boreholes around the lower reach of the Yangtze and the subaqueous Yangtze Delta (Li et al., 2000; Song et al., 2013), the riverbed of the lower Yangtze seems

to be formed during the formation of the Yangtze Delta after 7 ka and it does not contain the benthic foraminifera. However, before the TGD construction, deposition occurred in the middle to lower reaches of the Yangtze River before the TGD construction (Figure 1.3). Therefore, it seems to be difficult for the riverbed in the middle to lower reaches of the Yangtze to supply the old sediments, which were deposited in the riverbed before 2.3 ka (deposition of Unit 1), to the YD13 site continuously. Thus, the riverbed sediments of the middle to lower Yangtze are unlikely to be a potential source of the reworked material in Unit 1 of YD13.

Area IV represents the offshore L-TST sediments that is distributed in the offshore of the YD13 site and that are estimated as the source of the reworked sediments in Unit 2 in the previous section (Figure 2.16). Because of the presence of hiatus in Area IV since 6 ka, the offshore L-TST strata is considered to be still exposed at around 40–50 m water depth nowadays (Xu et al., 2016). As is already mentioned, L-TST strata exposed in this water depth is composed of clay to silt deposited during 12.5 to 7.5 ka (Xu et al., 2016). Since the OSL ages in Unit 1 of YD13 range from 1.9 to 3.2 ka, which are closer to the shell-based depositional age compared to the age of the L-TST (Figure 2.12), its contribution should be small if L-TST sediment is the source of the reworked material in Unit 1. Small contribution of the reworked material from the L-TST sediment is consistent with the rare

occurrence of foraminifera in Unit 1. Thus, Area IV sediments that are composed of L-TST sediments, which is same as the reworked material in Unit 2, could be a potential source of reworked material in Unit 1.

Area V is the shallow marine strata distributed along the coast of Jiangsu Province located to the north of the Yangtze rivermouth, including the old Yellow Rivermouth during the last 2ka (Figure 2.16). After the end of the transgression in the early to middle Holocene, a part of the sediments derived from the Yangtze River reached the modern Jiangsu coastal area (Area V), contributing to form the fluvial plain and the subaqueous sand ridges in that area (Li et al., 2001). It is shown that the seabed and coastal area of the southwestern Yellow sea, including the coast of Jiangsu province, have been eroded and transported to offshore at least during the last 150 yr based on examination of the bathymetric data (Zhou et al., 2014). They also showed that a part of eroded sediments are transported to the modern subaqueous Yangtze Delta area (Zhou et al., 2014). It is worth to note that the Yellow River flew into the South Yellow Sea, in the northern part of Area V, during AD 1128 to 1855, inducing the progradation of the shoreline and forming of a large delta. It is shown that the sediments derived from the Yellow River partly influenced the sediments around the subaqueous Yangtze Delta especially during the last 600 yrs (Liu et al., 2010). However, considering that quartz in SPM flowing the

Yellow River is enough exposed to sunlight and their OSL ages are almost reset (Hu et al., 2010), the depositional ages of the old Yellow River is too young to explain to the OSL ages of quartz of around 3 ka in Unit 1 of YD13. Thus, it is possible that the sediments around the Jiangsu coastal area were eroded to be transported to the YD13 site during the last 2 ka, and the fluvial plain and the subaqueous sand ridges are a potential source of the reworked materials in Unit 1 of YD13 but not the old Yellow Rivermouth at least before 0.6 ka.

In summary, the potential source of reworked material in Unit 1 of YD13 are estimated either as the L-TST strata located offshore side of YD13 site or the middle Holocene strata deposited around the coastal area of Jiangsu province.

2.8.2.2 Estimation of the contribution ratio of the reworked sediments and its controlling factor

As was discussed in the previous section, OSL ages of quartz in the YD13 sediments are considered as reflecting ages of mixtures of the reworked materials and the SPM directly supplied from the Yangtze River. In this section, I try to reconstruct temporal changes in contribution ratio of the reworked materials during the last 5 ka, based on the depositional ages and OSL ages of quartz.

Estimation of the contribution ratio of the reworked materials is based on the following

assumptions: 1) the sediments of YD13 are mixtures of the two components; the SPM from the Yangtze River (end member 1) that were directly supplied from the Yangtze, and the reworked sediments (end member 2) whose potential sources were estimated as above; 2) the depositional ages of end member 2 (t_2) in Unit 2 is assumed as an average of the radiocarbon ages of foraminifera in Unit 2; 3) the depositional ages of end member 2 (t_2) in Unit 1 is assumed as 5 to 6 ka when the coast of Jiangsu province were assumed to be formed (Li et al., 2001); 4) the age of the end member 1 (t_1) throughout Unit 1 and 2 is assumed to be equal to as the depositional age of the sediment based on the shell-based age model described in section 2.6.2, while the age of the end member 1 in Unit 2 is assumed to have an uncertainness as is described in section 2.6.2 and shown in Figure 2.12; and 5) the OSL age of fine-silt sized quartz (t_{OSL}) is explained by a linear combination of the end member 1 age (t_1) and end member 2 (t_2) with the mixing ratio of α:(1-α). Assumption (2) is based on the estimation described in the previous section that L-TST strata and the coast of Jiangsu province are the estimated source of the reworked material in Unit 2 and Unit 1, respectively. Assumption (4) is based on Sugisaki et al. (2015) which showed that SPM are almost completely bleached in the lower reach of the Yangtze mainstream, thus the SPM which was directly discharged from the Yangtze River should be equal to the OSL age of the deposition.

Then, the OSL age of fine silt size grains in a sample of Unit 1 and 2 is given by the equation below at the composite depth of each OSL sample in Unit 1 and 2:

$$t_{OSL} = (1-\alpha)\, t_1 + \alpha t_2 \quad \text{——} \quad (2.1)$$

where t_{OSL} is the interpolated OSL age of quartz at the composite depth of OSL sample, t_1 is the interpolated shell-based depositional age at the same composite depth as the OSL sample, t_2 is the average of radiocarbon ages of foraminifera (7.8±1.1 ka) in Unit 2 and the formation of the coast of Jinangsu province (5.5±0.5 ka) in Unit 1 following the assumption (3) described above, and α is the contribution ratio of the old end member at the depth of the OSL sample. The error for t_{OSL} is given by the standard error of OSL ages which are used for 3 point average. t_1 in Unit 2 is assumed to have an uncertainness as is shown in Figure 2.17(a). The error for t_2 is given by 2 × standard deviation of all radiocarbon ages of foraminifera. As α is unknown, the range of α is calculated by resolving equation (2.1) with respect to α at the every horizon where OSL sample exists under the condition of t_{OSL}, t_1, and t_2 within the error or uncertainness of these variables. The contribution ratio of the reworked materials are not calculated for the last 0.6 ka, because the OSL ages of quartz is not available (Figure 2.12).

Equation (2.1) indicates that the contribution ratio of the reworked material becomes smaller when the age of the reworked material becomes older if the OSL ages (t_{OSL}) and

the depositional age (t_1) are constant. Namely, in Unit 1, the age of the reworked material is assumed to be equal to the youngest depositional ages within several potential sources of the reworked material, indicating the estimated contribution ratio of Unit 1 in this section is the maximum value of contribution.

It is also true for Unit2 that the estimated contribution ratio of the reworked materials in this section is the maximum value. L-TST strata, the source of the reworked material in Unit 2, was formed during the transgression process following the sea-level rise and L-TST strata itself could contain the reworked materials from the offshore strata with older ages before 7 ka. Therefore, the contribution ratio of the reworked material which is estimated in this section is the maximum value throughout Unit 2 and 1.

Figure 2.17(b) and (c) shows the reconstructed contribution ratio of the end member 2 with every depth of OSL samples at YD13 core with aspect to the composite depth (Figure 2.17(b)) and the age (Figure 2.17(c)), respectively. The contribution ratio of the reworked sediments in Unit 2 are shown for age models of both Line A and B in Figure 2.17c. In Unit 2, the contribution ratio of the reworked sediments increase from 30 % to over 65 % toward the top of Unit 2, then dropped toward 5 % around 2.6 ka (8.0 m in the composite depth). This trend of the contribution ratio of the reworked sediments in Unit 2 is common regardless of the age model in Unit 2 (age model (A) and (B) in Figure 2.17a). At the

boundary between Unit 2 and Unit 1 around 2.3 ka (7.8m in the composite depth), the contribution ratio from the reworked materials dropped to 10 %. In Unit 1, the contribution ratio of the reworked sediments were ~5 % during 2.3 to 2.1 ka, then gently increased toward up to 40 % toward 0.6 ka (Figure 2.17c).

Based on the previous studies, it was indicated that the formation of L-TST strata around the subaqueous Yangtze Delta ended around 7.5 ka based on the sedimentary facies and radiocarbon ages in the sediment cores around the subaqueous Yangtze Delta (Xu et al., 2016). On the other hand, the increasing contribution of the reworked material from the offshore L-TST strata in Unit 2 from 5.1 to 2.6 ka in Unit 2 indicate that the edge of the modern subaqueous Yangtze delta had been affected by the reworking process from the offshore even in the period after the sea-level rise had ended around 5 ka.

The depositional age of Unit 1 after 2.3 ka is known as the period when the sediment discharge from the Yangtze River highly increased, resulting in the rapid progradation of both the subaerial and subaqueous Yangtze Delta (Li et al., 2000; Hori et al., 2001; Liu et al., 2010).

In Unit 1, the contribution from the reworked material increased after 2.3 ka (Figure

2.17b). Since the Jingsha area is located to just the south of the Jiangsu coast, it is possible that the sediments from the Jiangsu coastal area, which were transported southward by Jiangsu Coastal Current (JCC), was trapped around the Jingsha area (Figure 2.1, 2.2). As the position of the rivermouth sandbar migrated southeastward during the last 2 ka, JCC could have directly flew into the subaqueous Yangtze Delta and the sediments derived from the Jiangsu coastal area could increase (Figure 2.19b).

2.8.2.3 Constraint on the uncertainness of the age model based on the estimated contribution ratio from the reworked materials

The averaged sedimentation rate was 0.66 m/ky in Unit 3, 1.22 m/ky in Unit 2, and 3.79 m in Unit 1, respectively, indicating the sedimentation rate increased during the last 5 ky (Figure 2.12). The averaged sedimentation rate in Unit 3 (0.66 m/ky) seems not to include the effect from the reworked materials, while the averaged sedimentation rate in Unit 2 (1.22 m/ky) includes the effect from the reworked materials as was discussed in this section. Therefore, it seems that the sedimentation rate from the riverine materials (End member 2) in Unit 2 seems to be larger than that in Unit 3; namely, the lowest sedimentation rate from the riverine materials is assumed as 0.66 m/ky. Combined the lowest sedimentation rate from the riverine sediments with the estimated contribution ratio from the reworked materials in Unit 2, the lowest value of the total sedimentation

rate (End member 1 plus 2) in Unit 2 could be calculated.

$$R_{1,n} : R_2 = \alpha_n : (1-\alpha_n) \ldots (2.2)$$

$$R_{t,n} = R_{1,n} + R_2 = R_2 / (1-\alpha_n) \ldots (2.3)$$

Where $R_{1,n}$ is the sedimentation rate from the reworked materials at the depth of nth OSL sample in Unit 2, R_2 is the sedimentation rate from the riverine (Yangtze-derived) materials (fixed at the minimum value of 0.66 m/ky), α_n is the contribution rate from the reworked materials shown in Figure 2.17b at the depth of nth OSL sample, and $R_{t,n}$ (unknown) is the total sedimentation rate of the reworked plus riverine materials at nth OSL samples. $R_{t,n}$ is calculated at the depth of every OSL sample. Because now R_2 is fixed at the lowest value 0.66 m/ky, $R_{t,n}$ also indicates the lowest range of it.

Using $R_{t,n}$, the age difference between every adjacent OSL samples is calculated.

$$t_n = \Delta d_n / R_{t,n} \quad \ldots (2.4)$$

Where t_n (unknown) is the age difference between nth and n-1th OSL samples, $R_{t,n}$ is the total sedimentation rate at the depth of nth OSL sample, Δd_n is a difference of depth between nth and n-1th OSL samples.

The age-depth range acquired from formula 2.4 is shown in Figure 2.20. Because the age-depth range (Blue area in Figure 2.20) is initially acquired from the shell-based age model with uncertainness (Orange area in Figure 2.20), the blue and orange ranges are

expected to overlap each other. In Figure 2.20, the age models of blue and orange area only overlap around the shell based age model with the total sedimentation rate of 1.22 m/ky, and this overlapped range is assumed to be treated as the uncertainness of the age model in Unit 2. The uncertainness of the age model in Unit 2 is almost zero from 5 to 4 ka, then gradually increase up to ~300 yrs.

2.8.2.4 Removing the effect of the reworked materials from the ESR signal intensity and CI value in the background sediments

Significant contribution of the reworked materials at YD13 core during the last 5.1 ka, as was shown in Figure 2.17, suggests that the ESR signal intensity of sediments in YD13 could also be affected by the reworked materials. To extract the signal of the sediments directly discharged from the Yangtze, I tried to remove the effect of the reworked materials on the ESR signal intensity and CI value in this section.

The concept on estimation of the ESR signal intensity (or CI value) using the contribution ratio of the reworked material estimated in Figure 2.17 is shown in Figure 2.21. First, using the equation 2.1 under the same assumptions as described in the previous section, the contribution ratio of the reworked sediments are estimated at each sampling horizon in Unit 1 and 2 where the ESR signal intensity analysis was conducted. As the next step, the medium, minimum, and maximum corrected ESR

signal intensity are estimated by drawing lines starting from the medium, maximum, and minimum estimation for the ESR signal intensity of the reworked sediments, passing through the point representing the sample of interest and read the intercepts which represents the ESR signal intensity of the SPM to the left edge of the Figure which represents the reworked sediments being zero (Figure 2.2).

The maximum (minimum) value of the corrected ESR signal intensity is estimated by the minimum (maximum) estimate of the ESR signal intensity of the reworked sediments and the minimum (maximum) estimate of the contribution ratio of the reworked sediments (Figure 2.21). The medium value of the corrected ESR signal intensity is estimated by the medium values of the ESR signal intensity of the reworked sediments and the contribution ratio of the reworked sediments. The range of the ESR signal intensity of the reworked sediments is assumed as from 4 to 10 with the medium value of 7 using the range of the ESR signal intensity of quartz before 6 ka. This is because the age of the reworked sediments are estimated as 5.5±0.5 ka in Unit 1 and 7.5±1.1 ka in Unit 2 (Figure 2.18a). The corrections of the ESR signal intensity for constitution of the reworked sediments are conducted for the background sediments which were defined in section 2.7.4, because the flood sediments should reflect the event sedimentation and may not be appropriate to study the long-time variation of the

provenance. CI values of each samples are corrected for the effect of the reworked sediments using the same way as for the ESR signal intensity as was described above. The corrected ESR signal intensity and corrected CI values during the last 5.5 ka are shown in Figure 2.22a and b, respectively. The estimation range of the corrected ESR signal intensity is wide during 4 to 2.3 ka due to the large estimation error in the contribution ratio from the reworked sediments in that period (Figure 2.22a). However, the corrected ESR signal intensity seem to indicate the millennial- to centennial-scale fluctuations. The corrected CI values during 4 to 2.3 ka have a wide range of error similar to those of the ESR signal intensity during the same period, and also show the millennial- to centennial-scale fluctuation (Figure 2.22b). Thus, the corrected ESR signal intensity and CI values in Figure 2.22 is used for discussing the provenance changes at YD13 site during the last 5 ka.

2.8.3 Migration of the precipitation front in the Yangtze drainage basin during the middle to late Holocene

2.8.3.1 Temporal changes in the provenance of the background sediments based on the ESR signal intensity and CI values of quartz and their implication for the rain front movement

The rework-corrected ESR signal intensity and rework-corrected CI value shows centennial- to millennial-scale fluctuations during the last 5 ka (Figure 2.22). First in this section, the ESR signal intensity and CI values of quartz in samples from the background sediments that does not contain the flood layers are examined to reconstruct changes in the provenance of SPM discharged from the Yangtze River during the last 5.1 ky.

In Part 1, the major tributaries of the Yangtze were categorized into four groups based on their geographical distribution and coupling of the data plots (reflecting similarity of source rocks) on the ESR signal intensity vs CI diagram shown in Figure 1.9. Four groups are the upper Jinshajiang, the western tributaries, the northern tributaries, and the southeastern tributaries, respectively (Figure 1.9). The temporal variation of the ESR signal intensity and CI values of quartz in the background sediments are categorized into seven periods (5.0–4.1 ka, 4.1–2.3 ka, 2.3–2.1 ka, 2.1–1.3 ka, 1.3-1.0 ka, 1.0–0.7 ka, and after 0.7 ka) based on the trend of the ESR signal intensity and CI values changed, which are plotted on the ranges for four major tributary groups as was shown in Figure 1.9 (Figure 2.24).

In Figure 2.24, the provenance of the background sediments show the millennial changes. During 5.1 to 4.1 ka, both the ESR signal intensity and CI values highly varies, indicating the frequent changes of the provenance within the whole Yangtze basin (Figure 2.24a).

During 4.1 to 2.3 ka, the ESR signal intensity tends to be low, suggesting that the dominant contribution from the northwestern tributaries with possible minor contribution from the northeastern tributaries (Figure 2.24b). During 2.3 to 2.1 ka, the ESR signal intensity has a wide range from low to very high, whereas CI shows the medium to low values, suggesting the dominant contribution from the southeastern tributaries in addition to the western tributaries, upper Jinshajiang, and northeastern tributaries (Figure 2.24c). During 2.1 to 1.3 ka, the ESR signal intensity tends to be low again, suggesting the dominant contribution from the western tributaries and the upper Jinshajiang (Figure 2.24d). During the 1.3 to 1.0 ka, the ESR signal intensity increase slightly compared to those during 2.1 to 1.3 ka, suggesting the more contribution from the upper Jinshajiang or southeastern tributaries (Figure 2.24e). During 1.0 to 0.7 ka, the ESR signal intensity became slightly low and the CI value changed with high amplitude compared to those during 1.3 to 1.0 ka, suggesting the northeastern and Jinshajiang tributaries (Figure 2.24f). During 0.7 to 0.2 ka, the ESR signal intensity clearly became high and CI values became low (Figure 2.24g). The samples shown in Figure 2.24g during 0.7 to 0.2 ka seem to be out of range in those of tributary groups within the Yangtze basin. As was already described above, the rivermouth of the Yellow River was located in the South Yellow Sea during AD 1128 to 1857 to form a large delta, and the sediment from the Yellow River

partly affected the subaqueous Yangtze Delta during the last 600 yr (Liu et al., 2010). Thus, the high ESR signal intensity and low CI value during 0.7 to 0.2 ka could be attributable to the effect from the old Yellow River.

It is well known that the precipitation front in the monsoonal China showed a meridional migration annually based on the meteorological observation since the late 20th century (Ding et al., 2008; Zhou et al., 2011). Chen et al. (2015) compiled various paleo-climatic indices, including tree-ring $\delta^{18}O$, pollen assemblage, speleothem $\delta^{18}O$, and plant $\delta^{13}C$ around the Central and East Asia during the last millennium, especially during the Medieval Warm Period (MWP; 1.0–0.7 ka) and the Little Ice Age (LIA, 0.6–0.1 ka), respectively (Figure 2.25). They showed that North to Central China, which is located to the north of Huai River, became wetter relative to the average of the last millennium, while South China including the Yangtze basin became drier during the MWP. Similarly, they show that North to Central China became drier, while South China became wetter during the LIA. Based on the comparison of the pattern of the precipitation during the last 1 ky and the observational pattern of the precipitation during the late 20th century, they assumed that the pattern of the precipitation during LIA and MWP is similar to that during La Nina and El Nino event in the 20th century, respectively. They also compared these pattern with the reconstructed SST in the western equatorial Pacific, which is a proxy for

ENSO activity, and concluded that the pattern of the precipitation during the last 1 ky was affected by the ENSO activity (Chen et al., 2015).

In Part 1 of the thesis, it was shown that the ESR signal intensity of quartz in the detrital materials within the Yangtze basin have a decreasing trend toward the northwestern part of the basin. Namely, the lower ESR signal intensity during 1.0 to 0.7 ka, corresponding to MWP in the background sediment of YD13 core suggest that the background sediments in YD13 core were mainly derived from the northwestern Yangtze basin during this period (Figure 2.24f). On the other hand, the higher ESR signal intensity after 0.7 ka, corresponding to LIA, in the background sediments of YD13 core suggest that the background sediments were mainly derived from the southeastern Yangtze basin (Figure 2.24g). The northward (southward) migration of the main sediment source area of the Yangtze River during MWP (LIA) is consistent with the northward (southward) migration of the wet area in MWP (LIA) based on Chen et al. (2015) as is described above. Thus, it is reasonable to assume that the changes in the provenance of sediments in YD13 reflect the migration of the monsoonal precipitation front within the Yangtze basin.

2.8.3.2 Estimation of the relative contribution of sediments from the northwestern and southeastern parts of the Yangtze drainage basin

In the previous section, I demonstrated that changes in the provenance of sediments in YD13 core seems to indicate migration of the precipitation front. In this section, the relative contribution of SPM from the northwestern and southeastern part of the Yangtze drainage basin is estimated to examine the magnitude the precipitation change in each part of the Yangtze basin in comparison with the modern precipitation in each part of the basin.

Although the Yangtze drainage basin was divided into four tributary groups in the previous section, I divided the Yangtze drainage basin into two areas, namely the northwestern area and southeastern area for the sake of simplification. The northwestern area includes the upper Jinshajiang, western tributaries, and northeastern tributaries, while the southeastern area corresponds to the southeastern tributaries.

The ESR signal intensity of sediments from the northwestern and southeastern areas are calculated in the similar equations as are described below.

$$\alpha_{JSJ} = QY_{JSJ} / QY_{NW,\,total} \ldots (2.2)$$

$$\alpha_{JSJ} + \alpha_{MJ} + \alpha_{JLJ} + \alpha_{HJ} = 1 \ldots (2.3)$$

$$ESR_{NW} = \alpha_{JSJ} ESR_{JSJ} + \alpha_{MJ} ESR_{MJ} + \alpha_{JLJ} ESR_{JLJ} + \alpha_{HJ} ESR_{HJ} \ldots (2.4)$$

$$\alpha_{WJ} + \alpha_{DTL} + \alpha_{PYL} = 1 \ldots (2.6)$$

$$ESR_{SE} = \alpha_{WJ} ESR_{WJ} + \alpha_{DTL} ESR_{DTL} + \alpha_{PYL} ESR_{PYL} \ldots (2.7)$$

In the equation (2.2), α_{JSJ} is the contribution ratio of the Jinshajiang to the total quartz discharged from the northwestern area, QY_{JSJ} is the quartz discharge from the Jinshajiang, $QY_{NW,\ total}$ is the total quartz discharge from the northwestern area including the Jinshajiang, Minjiang, Jialingjiang, and Hanjiang. Similarly, α_{MJ}, α_{JLJ}, and α_{HJ} represent the contribution ratio of the Minjiang, Jialingjiang, and Hanjiang to the total quartz discharged from the northwestern area, respectively, and are calculated in the same way as α_{JSJ} in the equation (2.2). Thus, the summation of α_{JSJ}, α_{MJ}, α_{JLJ}, and α_{HJ} is equal to 1 as is shown in the equation (2.3).

In the equation (2.4), ESR_{JSJ}, $ESR_{MJ}+\alpha$, ESR_{JLJ}, and ESR_{HJ} indicate the ESR signal intensity of sediments discharged from the Jinshajiang, Minjiang, Jialingjiang, and Hanjiang. ESR_{NW} is calculated as the weighted average of the ESR signal intensity of sediments discharged from the northwestern area.

α_{WJ}, α_{DTL}, and α_{PYL}, which represent the contribution ratio of the Wujiang, Dongting Lake, and Poyang Lake to the total quartz discharged from the southeastern area, are also calculated in the same way as α_{JSJ} in the equation (2.2). In the equation (2.7), ESR_{SE} is calculated as the weighted average of the ESR signal intensity of sediments discharged from the southeastern area.

The calculated values of ESR_{NW} and ESR_{SE} are 4.0 and 14.8, respectively. I assume that

the ESR signal intensity of quartz in the fine–silt fraction of the sediments at the rivermouth is explained by a linear combination of the ESR signal intensity of quartz in the fine–silt fraction of the sediments from the northwestern area and from the southeastern area of the drainage basin, which is expressed by the equation below.

$$ESR_{Rivermouth} = \alpha ESR_{NW} + (1-\alpha)ESR_{SE} \quad \ldots (2.8)$$

where $ESR_{Rivermouth}$ is the analyzed ESR signal intensity of quartz in the fine–silt fraction of the sediments at YD13, ESR_{NW} is the ESR signal intensity of quartz in the fine–silt fraction of the sediments from the northwestern area, ESR_{SE} is the ESR signal intensity of quartz in the fine–silt fraction of the sediments from the southeastern area, and α is the relative contribution ratio of sediments from the northwestern area ($0< \alpha <1$), respectively. Since ESR_{NW} and ESR_{SE} have uncertainties of 1.96σ, α is also estimated with uncertainty; considering the range of ESR_{NW} is smaller than that of ESR_{SE}, the minimum value of α (α_{min}) is expressed by

$$ESR_{Rivermouth} = \alpha_{min} ESR_{NW,min} + (1-\alpha)_{min} ESR_{SE,min} \quad \ldots (2.9)$$

where $ESR_{NW,min}$ and $ESR_{SE,min}$ are the minimum estimate of the ESR signal intensity of quartz in the fine–silt fraction of the sediments from the northwestern and southeastern areas, respectively.

Similarly, the maximum values of α (α_{max}) is expressed by

$$ESR_{Rivermouth} = \alpha_{max} ESR_{NW, max} + (1-\alpha)_{max} ESR_{SE, max} \quad \ldots (2.10)$$

where $ESR_{NW, max}$ and $ESR_{SE, min}$ are the minimum estimate of the ESR signal intensity of quartz in the fine–silt fraction of the sediments from the southeastern areas, respectively.

Under the average annual sediment budget during the late 20th century (Figure 1.4), the modern contribution ratio of SPM from the northwestern area of the Yangtze Basin to the sediments at the rivermouth is calculated as 91 %. The analyzed ESR signal intensity at the modern Yangtze rivermouth is 4.4 (Table 1.3). If assuming $ESR_{Rivermouth}$ is 4.4, the contribution ratio from the northwestern area is estimated between 72 to 100 % with an average of 96 %, using the equations (2.8)–(2.10). Thus, the equation (2.2)–(2.4) properly reflect the contribution ratio of the sediment from the northwestern part and southeastern area of the Yangtze.

Using the formulas (2.8)–(2.10), the relative contribution ratio of the sediment from the northwestern area (α) in the background sediments are estimated using the three point averaged ESR signal intensity of the background sediments as expressed $ESR_{Rivermouth}$ (Figure 2.27).

In Figure 2.27(a), the contribution ratio from the northwestern area has changed in a millennial scale during the last 5.1 ka, although the error of estimation is large. From 5.1

to 4.1 ka, the contribution ratio from the northwestern area remained less than 60 %, except samples around 4.4 ka where the median values was around 60 % (Figure 2.27(a)), then the ratio increased to near 100 % around.4.1 ka. From 4.1 to 2.3 ka, the median value of the contribution ratio from the northwestern area remains high at around 80–100 %. Then the contribution ratio from the northwestern area suddenly decreased to 10 % from 2.3 to 2.1 ka and then increased to 100 % at 2.1 ka. From 2.1 to 1.0 ka, the contribution ratio shows a slightly decreasing trend although the estimation error is large. From 1.0 to 0.9 ka, the contribution ratio show a rapid increase to 100 %. After 0.9 ka, the contribution ratio decreased from 90 % to 20 %, then seemed to increase again to high value around 70 % consistent with the value in the modern status from 0.5 to 0.2 ka (Figure 2.27(a)).

2.8.3.3 Migration of the precipitation front within the Yangtze basin during the last 5 ka reconstructed from the background sediments of YD13 cores

Within the last 5 ka, there are a few periods when the contribution from the northwestern area drastically decreased to less than 20 %. In order to examine the hydrological condition in the Yangtze basin when the contribution from the northwestern area became low, the maximum sediment load and water discharge observed during the period when the instrumental observation was conducted are used as a reference for an extreme condition. Based on the observation at the gauge stations along the Yangtze River, the

sediment load is calculated as a product of the suspended sediment concentrations (SSC) and the water discharge (Wang et al., 2007). The maximum SSC at Yichang from 1950 to 1980 was 10.5 kg/m^3 observed on July 29, 1959 and the maximum water discharge from 1877 to 2000 was 71,100 m^3/s on Sept. 4, 1896 (Chen et al., 2001; Zhang et al., 2006). The observational period of the SSC and water discharge is different because the observation of SSC started only in the late 20th century, while that of water discharge stated in 19th century. As a product of these maximum values of SSC and water discharge, the maximum sediment load at Yichang can be calculated as 64.5 Mt/day. On the other hand, the averaged SSC and water discharge at Yichang during July of the late 20th century were 1.91 kg/m^3 and 3.0×10^4 m^3/s, respectively (Chen et al., 2001) and, the average sediment discharge in July is calculated as 4.9 Mt/day. Thus, the sediment discharge at Yichang during the extreme flood could be at least 13 times larger than the average value of July based on the observational records.

The significant low contribution from the northwestern area around 10 % at around 4.2 ka, 2.2 ka, and 0.5–0.3 ka are assumed to be induced by either extreme high sediment discharge from the southeastern area or extreme low sediment discharge from the northwestern area. Assuming that the sediment discharge from the southeastern area in July increased to 13 times larger than the average sediment discharge from the region

during the late 20th century, the contribution ratio from the northwestern area in the annual sediment discharge would decrease to 49 % at most. Therefore, under the hydrological condition similar to that during the late 20th century, it is difficult to explain the very low contribution ratio from the northwestern area below 49 % by the increase of the sediment discharge from the southeastern area only.

To explain the very low contribution from the northwestern area by changes in the distribution of the sediment discharge within the Yangtze River basin, there are two possibility. One possibility is that the decrease in the sediment discharge from the northwestern area happened simultaneously with the increase in the sediment discharge from the southeastern area. Another possibility is that the increase in the sediment discharge from the southeastern area was beyond the magnitude estimated based on the hydrological condition during the late 20th century. On the other hand, to explain the low contribution ratio from the northwestern area around 20 % only by the increase in the sediment discharge from the southeastern area, it is required that the sediment discharge from the southeastern area increased by almost 50 times larger than the average sediment discharge from the southeastern area during the late 20th century.

Thus, to explain the low sediment contribution over 51 % from the northwestern area, the decrease in the sediment discharge from the northwestern area seems necessary in

addition to the increase the sediment discharge from the southeastern area. Consequently, the position of the precipitation front seems to have retreated southward compared to that at present.

Thus, the high α of value around 90 % indicates that the sediment contribution from the northwestern and southeastern areas is similar to that in the modern hydrological condition, whereas modarate α value around 80–60 % also indicate that the larger contribution from the southeastern area compared to the hydrological condition at present. In summary, the increasing α value suggests northward migration of the precipitation front, while decreasing α value suggests the southward migration of the precipitation front.

Based on the α value, the changes in the position of the precipitation front in the Yangtze basin during the last 5.1 ka are illustrated as following. The precipitation front showed a significant southward migration from 5.1 to 4.1 ka, northward migration from 4.1 to 2.3 ka, significant southward migration from 2.3 to 2.1 ka, northward migration from 2.1 to 1.3 ka, slight southward migration from 1.3 to 1.0 ka, northward migration from 1.0 to 0.7 ka, and significant southward migration from 0.7 to 0.2 ka (Figure 2.25).

The meteorological observation since the late 20th century revealed that the weakening of EASM intensity leads to the southward migration of the precipitation front around the

Yangtze River basin (Ding et al., 2008; Zhang et al., 2009). Namely, the southward (northward) migration of the precipitation front recorded in YD13 core are interpreted as indicating the weakening (intensification) of the EASM. There are many reconstructions on the EASM intensity changes in the past based on the various proxies such as the oxygen isotope ratio of the stalagmite and late sediments, carbon isotope of the peats, and tree-ring (An et al., 2000; Wang et al., 2005; Zhang et al., 2011; Yi et al., 2012). Based on these reconstructions, it has been believed that the EASM intensity have been regulated by the insolation and that there is a weakening trend of the EASM intensity after the maximum insolation intensity was attained at the Holocene optimum around 7–8 ka (e.g. Wang et al., 2005; Zhang et al., 2011). It is also believed that the timing of weakening of EASM varied between North China and South China (An et al., 2000; Zhang et al., 2011). On the other hand, several recent studies demonstrated that the oxygen isotopes of the stalagmites do not reflect the intensity of summer precipitation but rather reflect other factors such as the vapor sources and/or condition of vapor source area (e.g. Maher et al., 2012; Liu et al., 2015).

In the Yangtze basin, Kubota et al. (2015) reconstructed the water discharge from the whole Yangtze basin during the last 7 ka. Their result demonstrated that the water discharge from the Yangtze basin fluctuated in millennial scale but long-term decreasing

trend since 7 ka is not clear, suggesting that the water discharge from the Yangtze basin were not regulated by the insolation (Kubota et al., 2015; Figure 2.28(b)). From 5 to 4 ka, it seems that the contribution from the northwestern area in YD13 sediments and the water discharge from the Yangtze River reconstructed by Kubota et al. (2015) changes asynchronously. Namely, when the contribution from the northwestern area in YD13 sediments increases (decreases), the water discharge from the Yangtze River decreased (increased). From 5 to 4 ka, the water discharge from the Yangtze River changes centennially, and the contribution from the northwestern area in YD13 sediments also changes centennially but asynchronous with the water discharge from the Yangtze River. From 4 to 2.3 ka, the water discharge from the Yangtze River changes centennially, while the contribution from the northwestern area in YD13 sediments remained high with slight decrease at around 3.2 ka. From 2.3 to 0.7 ka, the contribution from the northwestern area in YD13 sediments and the water discharge from the Yangtze changed asynchronously again. However, after 0.7 ka, it seems that contribution from the northwestern area in YD13 sediments and the water discharge from the Yangtze changed synchronously.

The meteorological observation during the late 20th century indicates that the strong (weak) convection over the South China Sea to South China leads to the northwestward (southeastward) migration of the precipitation front (Ding et al., 2008). Thus, it seems

that the high contribution from the southeastern Yangtze basin in the YD13 sediments suggests the southeastern migration of the precipitation front, namely the weak monsoon. On the other hand, when the monsoon (convection) becomes much strong, the westerly jet moves northward earlier and the precipitation front also moves to northward earlier. As a result, it is also indicated that the precipitation front induced by the convection could reach to the Yellow River Basin, and that the precipitation in the whole Yangtze Basin could decrease (Ding et al., 2008). Consequently, the intensification of the monsoon and the decrease in the total precipitation within the whole Yangtze Basin, which leads to the decrease in the water discharge from the whole Yangtze River, could occur simultaneously, resulting in the asynchronous relationship between the water discharge from the Yangtze River and the contribution from the northwestern area of the Yangtze Basin in YD13 core.

In summary, the combination of the contribution ratio within the Yangtze basin to the YD13 sediments and the water discharge from the Yangtze River could represent the migration of the precipitation front. It is also suggested that the distribution of precipitation within the vast area like the Yangtze basin is necessary to reconstruct the migration of the precipitation front, connecting to the monsoon intensity.

2.8.4 Relationship between changes in the precipitation front position and the frequency and provenance of the flood layers

In the Yangtze River, floods have been occurring frequently. For example, during the 20th century, there were three large flood events in 1931, 1954, and 1998 in the Yangtze basin and these floods submerged the land along its channels (Dai et al., 2010). There are many reconstructions of floods or droughts in the Yangtze basin based on the historical documents, many of which discussed the factors that trigger the occurrence of floods or droughts (e.g. Jiang et al., 2005; Shen et al., 2007; Ji et al., 2015). Other studies used the slackwater sediments, which were left along the valley when the water level reach a high level than usual, to reconstruct the magnitude and occurrence of paleofloods (Huang et al., 2013; Guo et al., 2016). Based on their flood reconstructions, the occurrence of floods in the Yangtze basin are considered as influenced by ENSO activity (Jiang et al., 2006). In fact, the large flood of the Yangtze since the late 20th century, when the meteorological data are available, mainly occurred after the occurrence of El Nino (Shankman et al., 2006). In a short time scale from weekly to monthly, it is reported that the floods occurred when the precipitation front remain at the same region for several weeks (e.g. Zong and Chen, 2000), suggesting that the position of the precipitation front could be an important factor to control to the occurrence of the floods.

However, the flood reconstruction based on the historical documents are usually limited to the last 500 to 1000 yrs because of the lack of the reliable descriptions (Jiang et al., 2005; 2006; Zhang et al., 2008). The record of the slackwater sediments along the river channel are not appropriate for a long-term continuous reconstruction of paleofloods, because slackwater sediments are preserved intermittently when the water level reached an extremely high than usual. In this section, the relationship between the occurrence of floods and the migration of the precipitation front during the last 2.3 ka is discussed by directly comparing the ESR signal intensity and frequency of the flood layers and the ESR signal intensity of the background sediments which are obtained from both YD13 core.

2.8.4.1 Relationship among the migration of the precipitation front, frequency of the flood layers, and provenances of the flood layers

To examine the relationship among the flood frequency, provenance of floods, and the migration of the precipitation front that caused the floods, the flood-layer frequency is calculated (Figure 2.29). Because of the rare occurrence of the floods layers in YD13 core before 2.3 ka, the flood-layer frequency is calculated only for the last 2.3 ka as the count of the Type A plus B layers at every 100 yrs as defined in Section 2.4.2.1.

Figure 2.29 compares the ESR signal intensity of the background sediments corrected for

contamination of the reworked sediments, the ESR signal intensity of the flood sediments, the flood-layer frequencyThe ESR signal intensity of the flood sediments tend to be larger than those of the background sediments during 1.9–1.3 ka, indicating that floods occurred in the southeastern area of the Yangtze basin when the precipitation front remained in the northwestern area of the Yangtze basin. This difference between the position of the flood occurrence and the precipitation front during 1.9–1.3 ka suggests that the controlling factor of the flood occurrence and the migration of the precipitation front during that period might have been different from the present.

The period from 2.3 to 2.1 has a clear characteristic; namely, the flood-layer frequency, the ESR signal intensity of the background sediments and the ESR signal intensity of the flood sediments increased in this period (Figure 2.29). Considering the high contribution ratio of the southeastern basin in this period (Figure 2.28), it is assumed that there was heavy rain and floods occurrence in the southeastern area, whereas a drought might have happened in the northwestern area. Paleofloods study by Guo et al. (2016) in the Three Gorges region, which is the outlet of all the upper Yangtze basin, suggests absence of flood during this period at which is conformable with the possible drought in the upper Yangtze basin estimated from this thesis. Li et al. (2014) studied the sediment core recovered from the central Jianghan Plain, which was located in the outlet of the Three

Gorges, and showed that there were dry periods during 4.4–3.9 ka and 2.3–2.1 ka based on Rb/Sr ratio. Since Rb have a similar diameter to that of K, Rb is dispersed in minerals containing K and tends to be enriched in clay minerals (Wang et al., 2010). On the other hand, Sr tend to be concentrated to coarse grains. Because the Jianghan Plain gathers the water which are discharged from the whole upper Yangtze River basin, the dry condition in the Jianghan Plain also suggests dry condition in the upper Yangtze River basin. Since the previous studies which reconstructed the paleofloods using the historical records only extends back to the last 2 ky due to the limitation of the historical documents (Ge et al., 2016), there is no supporting evidence for the possible frequent floods in the southeastern area during 2.3 to 2.1 ka. However, the sea surface salinity (SSS) changes in the ECS reconstructed by Kubota et al. (2010) showed a decreasing trend between 3 to 2 ka. Because the SSS in the ECS is highly affected by the water summer water discharge from the Yangtze River, the decrease of SSS in the ECS suggests larger discharge from the Yangtze River in total (Kubota et al., 2010; 2015). Thus, it is estimated that, during 2.3–2.1 ka, severe drought in the northwestern area and frequent floods in the southeastern area may have occurred simultaneously during 2.3–2.1 ka, resulting in the increasing ESR signal intensity and increased the flood frequency in YD13 core.

2.9 Summary

YD13 cores were recovered from the subaqueous Yangtze delta. A composite column of YD13 sediments is constructed for top 10 m of the sequence by splicing cores from two holes and a gravity core. The top 10 m of YD13 sediments are mainly composed of gray silt and many coarse-silt to sand layers are identified on the composite column. Four lithological units are defined based on the occurrence of the coarse-silt to sand layers. The sedimentary age model of YD13 is constructed for the last 5.1 ky based on the radiocarbon ages of shell fossils (the shell-based age model).

The coarse–silt to sand layers in YD13 sediments are categorized into three types based on their sedimentological structure. Within three types, Type A and Type B layers which have a horizontal continuity and the sharp bottom boundary seem to represent the paleoflood events, when comparing with the historical floods record.

On the basis of the older radiocarbon ages of the foraminifera and the older OSL ages of the fine-silt sized quartz compared to the ages by the shell-based age model, it is suggested that the YD13 sediments deposited during 5.1 to 2.3 ka were significantly affected by the reworked materials, which were originally deposited during the transgression in the early to middle Holocene by 7.5 ka in addition to the riverine

sediments discharged directly from the Yangtze rivermouth. It is also suggested that the YD13 sediments during the last 2.3 ka might be partly affected by the coastal sediments along the Jiangsu province, although the contribution from the reworked materials are smaller than those during 5.1 to 2.3 ka. The contribution ratio of reworked sediments are estimated around 30 to 70 % and seems to be controlled by the development of the Yangtze delta and sediment discharge from the Yangtze River.

The ESR signal intensity and crystallinity index are analyzed for both the coarse-silt to sand layers and the background sediments that do not include the coarse-silt to sand layers. The result of the background sediments revealed changes in the provenance within the Yangtze drainage basin during the last 5.1 ka. I tried to remove the effect of the reworked materials from the ESR signal intensity and CI values of quartz in the fine–silt fraction of YD13 sediments using the estimated contribution ratio of the reworked materials.

When comparing the ESR signal intensity and CI of YD13 sediments during the last 5.1 ky with those for the major tributaries of the Yangtze drainage basin, the contribution from the southeastern area became significant during 2.3–2.1 ka, 1.3–1.0 ka, and after 0.7 ka, while that from the northwestern area became moderate to significant during the other period. Assuming the provenance change in YD13 sediments reflect changes in the

distribution of precipitation in the drainage basin, the changes in the provenance change in YD13 sediments is consistent with the past climate reconstructed from the historical records and other paleo-climatological proxies.

The estimation of the contribution ratio from the northwestern and southeastern Yangtze basin to YD13 sediments during the last 5.1 ka suggests that the contribution ratio from the northwestern area decreased up to 80 %. Based on the observed maximum and average sediment discharge, not only the increase of precipitation in the southeastern part but also the decrease of precipitation in the northwestern part would be necessarily to explain this magnitude. This status could correspond to the precipitation pattern during the weaker monsoon, and combined with the water discharge from the Yangtze River by other study, the migration of the precipitation front could be reconstructed. In comparison with the ESR signal intensity of the background sediments and the flood layers (Type A and Type B), it is suggested that the flood tend to occur at the same area as the precipitation front is located.

Conclusion

To estimate the intensity of the East Asian Summer Monsoon in the past, the spatial distribution of the precipitation front through the provenance of sediments within the Yangtze River Basin was reconstructed at the subaqueous Yangtze Delta, where gathers the sediments from the whole the Yangtze basin. As the first step, to distinguish the sediments from different parts of the Yangtze basin, the ESR signal intensity and CI value of riverbed sediments taken from the mainstream and major tributaries of the Yangtze are examined. It is indicated that the ESR signal intensity and CI value reflect the geological blocks in the basin which each tributary groups belongs to, and that the major tributaries of the Yangtze are categorized into four groups (the western, upper Jinshajiang, northeastern, and southeastern tributaries) based on the geographical distribution of the tributaries using the coupling of the ESR signal intensity and CI value.

As the sedimentary record at the Yangtze rivermouth during the middle to late Holocene, YD13 cores were recovered from the subaqueous Yangtze Delta with the water depth around 35 m. YD13 cores were mainly composed of the clayey silt with intercalation of the coarse–silt to sand layers. The top 10 m of YD13 was categorized into lithological units based on the frequency and structure of the coarse–silt to sand layers, and the inter-hole correlation among Hole 1, Hole 2, and G2 of YD13 were established by correlating

the coarse–silt to sand layers under the constraint of the lithological units and the water content. Based on the radiocarbon ages of the shell fossils, the top 10 m of YD13 core covers the last 5 ky.

The older OSL ages of quartz in the fine–silt fraction compared to the shell-based age model indicate the contamination from the reworked materials at YD13 core and the contribution ratio of the reworked materials are estimated. In Unit 2 from 5.1 to 2.3 ka, the source of the reworked materials is estimated as the late transgression system tract (L-TST) strata located offshore of YD13 site and the contribution ratio of it reaches up to 60 %. In Unit after 2.3 ka, the source of the reworked materials are estimated as the coastal sediments located to the north of the Yangtze Delta or the L-TST strata, and the contribution ratio of it is estimated as 10–40 %. The effect from the reworked materials are removed from the ESR signal intensity and CI value based on the estimated contribution ratio from the reworked materials.

The ESR signal intensity in the background sediments, which do not include the coarse–silt to sand layers, show the centennial to millennial fluctuation, and seems to represent the north–south migration of the precipitation front over the Yangtze basin during the last 5 ky. The coarse–silt to sand layers with sharp bottom boundary and upward fining show the similar frequency with that of the historical recorded floods during the last 2.3 ka and

seem to represent the occurrence of floods within the Yangtze basin. Comparing the ESR signal intensity of the coarse–silt to sand layers and that of the background sediments, it is indicated that floods within the Yangtze basin occurred at the same area as the area where the precipitation front was located.

Acknowledgement

I would like to thank R. Tada, K. Wang, T. Irino, H. Zheng for helping, advising, and pushing me during the analysis and writing. For arranging and helping the field trips in China and the YD13 sampling party at the Nanjing Normal University, I would like to thank C. Luo, M. He, P. Wang, S. Li, and car drivers. I would also like to thank S. Sugisaki, Y. Suzuki, S. Kurokawa, and Y. Kuboki for helping the field trips or the YD13 sampling party.

For the ESR and XRD analysis, K. Nagashima, and A. Karasuda helped me, and the staffs at Takasaki Advanced Radiation Research Institute, National Institutes for Quantum and Radiological Science and Technology (QST) help me γ-ray irradiation. M. Uchida and the staffs at the National Institute for Environmental Studies, Japan (NIES) and Y. Kubota helped me for the radiocarbon dating.

References

Ali JR, Thompson GM, Zhou MF, Song X (2005) Emeishan large igneous province, SW China. LITHOS 79:475-489. doi:10.1016/j.lithos.2004.09.013.

An Z, Porter SC, Kutzbach JE, Wu X, Wang S, Liu X, Li X, Zhou W (2000) Asynchronous Holocene optimum of the East Asian Monsoon. Quaternary Sci. Rev. 19:743-762.

Chang J, Li J, Lu D, Zhu X, Lu C, Zhou Y, Deng C (2010), The hydrological effect between Jingjiang River and Dongting Lake during the initial period of Three Gorges Project Operation. J Geog Sci 20(5):771-786. doi:10.1007/s11442-010-0810-9.

Chen J, Chen F, Feng S, Huang W, Liu J, Zhou A (2015) Hydroclimatic changes in China and surroundings during the Medieval Climate Anomaly and Little Ice Age: spatial patterns and possible mechanisms. Quaternary Sci. Rev. 307:98-111. doi:10.1016/j.quascirev.2014.10.012.

Chen J, Jahn B (1998) Crustal evolution of southeastern China: Nd and Sr isotopic evidence. Tectonophysics 284:101-133.

Chen JCH, Fung IY, Wu C-H, Cai Y, Edman JP, Liu Y, Day J-A, Bhattacharya T, Mondal Y, Labrousse CA (2015) Role of seasonal transitions and westerly jets in East Asian paleoclimate. Quaternary Sci. Rev. 108:111-129.

Chen Z, Li J, Shen H, Wang Z (2001) Yangtze River of China: historical analysis of discharge variability and sediment flux. Geomorphology 41:77-91. doi:10.1016/S0022-1694(02)00028-8.

Dai S-B, Lu XX (2010) Sediment deposition and erosion during the extreme flood events in the middle and lower reaches of the Yangtze River. Quat Int 226:4-11. doi:10.1016/j.quaint.2010.01.026.

Dai S-B, Yang S-L, Zhu J, Gao A, Li P (2005) The role of Lake Dongting in regulating the sediment budget of the Yangtze River. Hydrol Earth Syst Sci. 9:692-698.

Deng J, Wang Q, Li G, Li C, Wang C (2014) Tethys tectonic evolution and its bearing on the distribution of important mineral deposits in the Sanjiang region, SW China. Gondwana Res 26(2):419-437. doi:10.1016/j.gr.2013.08.002.

Ding Y, Wang Z, Sun Y (2008) Inter-decadal variation of the summer precipitation in East China and its association with decreasing Asian summer monsoon. Part I: Observed evidences. Int. J. Climatol. 28:1139-1161. doi:10.1002/joc.1615.

Dong Y, Santosh M (2016) Tectonic architecture and multiple orogeny of the Qinling Orogenic Belt, Central China. Gondowana Res 29(1):1-40. doi:10.1016/j.gr.2015.06.009.

Dong Y, Zhang G, Neubauer F, Liu X, Genser J, Hauzenberger C (2011) Tectonic evolution of the Qinling orogen, China: Review and synthesis. J Asian Earth Sci 41:213-

237. doi:10.1016/j.jseaes.2011.03.002.

Enkelmann E, Weislogel A, Ratschbacher L, Eide E, Renno A, Wooden J (2007) How was the Triassic Songpan-Ganzi basin filled? A provenance study. Tectonics 26:TC4007. doi:10.1029/2006TC002078.

Feigl FJ, Fowler WB, Yip KL (1974) Oxygen vacancy model for the E1' center in SiO2. Solid State Commun 14:225-229.

Gao JH, Jia J, Wang YP, Yang Y, Li J, Bai F, Zou X, Gao S (2015) Variations in quantity, composition and grain size of Changjiang sediment discharging into the sea in response to human activities. Hydrol Earth Syst Sci 19(2):645-655. doi:10.5194/hess-19-645-2015.

Guo Y, Huang CC, Zhou Y, Pang J, Zha X, Zhou L, Mao P (2016) Extraordinary flood events and the response to monsoonal climatic change during the last 3000 years along the middle Yangtze River valley, China. Palaeogeogr. Palaeoclimatol. Palaeoecol. 462:70-84. doi:10.1016/j.palaeo.2016.09.005.

Han G, Liu C-Q (2004) Water geochemistry controlled by carbonate dissolution: a study of the river waters draining karst-dominated terrain, Guizhou Province, China. Chem Geol 204:1-21. doi:10.1016/j.chemgeo.2003.09.009.

Hao F, Guo T, Zhu Y, Cal X, Zou H, Li P (2008) Evidence for multiple stages of oil cracking and thermochemical sulfate reduction in the Puguang gas field, Sichuan Basin,

China. Am Assoc Pet Geol Bull 92(5):611-637. doi:10.1306/01210807090.

Hassan MA, Church M, Yan Y, Slaymaker O (2010) Spatial and temporal variation of in-reach suspended sediment dynamics along the mainstem of Changjiang (Yangtze River), China. Water Resour Res 46:W11551. doi:10.1029/2010WR009228.

Hayashi S, Murakami S, Xu K-Q, Watanabe M (2008) Effect of the Three Gorges Dam Project on flood control in the Dongting Lake area, China, in a 1998-type flood. J Hydro-environ Res 2:148-163. doi:10.1016/j.jher.2008.10.002.

He M, Zheng H, Clift PD, Tada R, Wu W, Luo C (2015) Geochemistry of fine-grained sediments in the Yangtze River and the implications for provenance and chemical weathering in East Asia. Progr Earth Planet Sci 2:32. doi:10.1186/s40645-015-0061-6.

Hennig T, Wang W, Feng Y, Ou X, He D (2013) Review of Yunnan's hydropower development Comparing small and large hydropower projects regarding their environmental implications and socio-economic consequences. Renewable Sustainable Energy Rev 27:595-595. doi:10.1016/j.rser.2013.07.023.

Hori K, Saito Y, Zhao Q, Cheng PW, Sato Y, Li C (2001) Sedimentary facies and Holocene progradation rates of the Changjiang (Yangtze) delta, China. Geomorphology 41:233-248.

Hu B, Wang H, Yang Z, Sun X (2011) Temporal and spatial variations of sediment rating

curves in the Changjiang (Yangtze River) basin and their implications. Quat Int 230:34-43. doi:10.1016/j.quaint.2009.08.018.

Hu B, Yang Z, Wang H, Sun X, Bi N, Li G (2009) Sedimentation in the Three Gorges Dam and the future trend of Changjiang (Yangtze River) sediment flux to the sea. Hydrol. Earth Syst. Sci. 13:2253-2264.

Hu C, Henderson G-M, Huang J, Xie S, Sun Y, Johnson K-R (2008) Quantification of Holocene Asian monsoon rainfall from spatially separated cave records. Earth Planet. Sci. Let. 266:221-232.

Hu G, Li A, Liu J, Gang X, Mei X, Kong X (2014) High resolution records of flood deposition in the mud area off the Changjiang River mouth during the past century. Chinese J. Oceanol. Limnol. 32:909-920.

Hu G, Zhang JF, Qiu WL, Zhou LP (2010) Residual OSL signals in modern fluvial sediments from the Yellow River (HuangHe) and the implications for dating young sediments. Quat. Geochronogy. 5:187-193. doi:10.1016/j.quageo.2009.05.003.

Hu Q, Feng S, Guo H, Chen G, Jiang T (2007) Interactions of the Yangtze river flow and hydrologic processes of the Poyang Lake, China. J Hydrol 347:90-100. doi:10.1016/j.jhydrol.2007.09.005.

Huang CC, Pang J, Zu X, Zhou Y, Yin S, Su H, Zhou L, Yang J (2013) Extraordinary

hydro-climatic events during the period AD 200?300 recorded by slackwater deposits in the upper Hanjiang River valley, China. Palaeogeogr. Palaeoclimatol. Palaeoecol. 374:274-283.

Isozaki Y (2009) Characterization of eolian dust and its sources in the Tarim Basin and their temporal changes during Plio-Pleistocene based on the ESR signal intensity and Crystallinity Index of quartz. Ph. D. thesis, The University of Tokyo, Tokyo, Japan.

Ji Y, Zhou G, Wang S, Wang L (2015) Increase in flood and drought disasters during 1500?2000 in Southwest China. Nat. Hazards. 77:1853-1861.

Jiang T, Zhang Q, Blender R, Fraedrich K (2005) Yangtze Delta floods and droughts of the last millennium. Theor. Appl. Climatol. 82:131-141.

Jiang T, Zhang Q, Zhu D, Wu Y (2006) Yangtze floods and droughts (China) and teleconnections with ENSo activities (1470-2003). Quaternary Int. 144:29-37.

Kubota Y, Kimoto K, Tada R, Oda H, Yokoyama Y, Matsuzaki H (2010) Variations of East Asian summer monsoon since the last deglaciation based on Mg/Ca and oxygen isotope of planktic foraminifera in the northern East China Sea. 25:PA4205.

Kubota Y, Tada R, Kimot K (2015) Changes in East Asian summer monsoon precipitation during the Holocene deduced from a freshwater flux reconstruction of the Changjiang (Yangtze River) based on the oxygen isotope mass balance in the northern East China Sea.

Clim. Past. 11:265-281.

Lane SN, Parsons DR, Best JL, Orfeo O, Kostaschuk RA, Hardy RJ (2008) Causes of rapid mixing at a junction of two large rivers: Rio Parana and Rio Paraguay, Argentina. J Geophys Res 113:F02019. doi:10.1029/2006JF000745.

Li C, Chen Q, Zhang J, Yang S, Fan D (2000) Stratigraphy and paleoenvironmental changes in the Yangtze Delta during the Late Quaternary. J. Asian Earth Sci. 18:453-469.

Li CX, Zhang JQ, Fan DD, Deng B (2001) Holocene regression and the tidal radial sand ridge system formation in the Jiangsu coastal zone, east China. Marine Geol. 173:97-210. doi:10.1016/S0025-3227(00)00169-9.

Li X, Bianchi T-S, Allison M-A, Chapman P, Mitra S, Zhang Z, Yang G, Yu Z (2012) Composition, abundance and age of total organic carbon in surface sediments from the inner shelf of the East China Sea. Marine Chem. 145-147:37-52.

Liu H, Lan H, Liu Y, Zhou Y (2011) Characteristics of spatial distribution of debris flow and the effect of their sediment yield in main downstream of Jinsha River, China. Environ Earth Sci 64:1653-1666. doi:10.1007/s12665-009-0409-6.

Liu J, Saito Y, Kong X, Wang H, Xiang L, Wen C, Nakashima R (2010) Sedimentary record of environmental evolution off the Yangtze River estuary. East China Sea, during the last ~ 13,000 years, with special reference to the influence of the Yellow River delta

during the last 600 years. Quaternary Sci. Rev. 29:2424-2438.

Liu JP, Xu KH, Li AC, Milliman J-D, Velozzi D-M, Xiao SB, Yang ZS (2007) Flux and fate of Yangtze River sediment delivered to the East China Sea. Geomorphology 85:208-224.

Luo L, Qi J-F, Zhang M-Z, Wang K, Han Y-Z (2014) Detrital zircon U-Pb ages of Late Triassic-Late Jurassic deposits in the western and northern Sichuan Basin margin: constraints on the foreland basin provenance and tectonic implications. Int J Earth Sci (Geol Rundsch) 103:1553-1568. doi:10.1007/s00531-014-1032-7.

Ma Y, Zhang S, Guo T, Zhu G, Cai X, Li M (2008) Petroleum geology of the Puguang sour gas field in the Sichuan Basin, SW China. Mar Pet Geol 25:357-370. doi:10.1016/j.marpetgeo.2008.01.010.

Maher BA, Thompson R (2012) Oxygen isotopes from Chinese caves: records not of monsoon rainfall but of circulation regime. J. Quaternary Sci. 27(6):615-624.

Mao CP, Chen J, Yuan XY, Yang ZF, Balsam W, Ji JF (2010) Seasonal variation in the mineralogy of the suspended particulate matter of the lower Changjiang River at Nanjing, China. Clay and Clay Minerals 58(5):691-706. doi:10.1346/CCMN.2010.0580508.

Mao CP, Chen J, Yuan XY, Yang ZF, Ji JF (2011) Seasonal variations in the Sr-Nd isotopic compositions of suspended particulate matter in the lower Changjiang River: Provenance

and erosion constraints. Chin Sci Bull 56:2371-2378. doi: 10.1007/s11434-011-4589-6.

Meng Q-R, Zhang G-W (2000) Geologic framework and tectonic evolution of the Qinling orogen, central China. Tectonophysics 323:183-196. doi:10.1016/S0040-1951(00)00106-2.

Murata KJ, Norman MB (1976) An index of crystallinity of quartz. Am J Sci 276:1120-1130.

Nagashima K, Tada R, Tani A, Toyoda S, Sun Y, Isozaki Y (2007) Contribution of aeolian dust in Japan Sea sediments estimated from ESR signal intensity and crystallinity of quartz. Geochem Geophys Geosyst 8:Q02Q04. doi:10.1029/2006GC001364.

Nagashima K, Tada R, Toyoda S (2013) Westerly jet-East Asian summer monsoon connection during the Holocene. Geochem. Geophs. Geosyst. 14:5041-4053.

Nakagawa T, Suigetsu_2006_Project_Members (2014) High-precision sampling of laminated

Qin J-F, Lai S-C, Grapes R, Diwu C, Ju Y-J, Li Y-F (2010) Origin of Late Triassic high-Mg adakitic granitoid rocks from the Dongjiangkou area, Qinling orogen, central China: Implications for subduction of continental crust. Lithos 120:347-367. doi:10.1016/j.lithos.2010.08.022.

Rea DK, Janecek TR (1981) 25. Mass-Accumulation Rates of the Non-Authigenic

Inorganic Crystalline (Eolian) Component of Deep-Sea Sediments from the Western Mid-Pacific Mountains, Deep Sea Drilling Project Site 463. Initial Reports of the Deep Sea Drilling Project 62:653-659. doi:10.2973/dsdp.proc.62.125.1981.

Reid AJ, Folwer AP, Phillips D, Wilson CJL (2005b) Thermochronology of the Yidun Arc, central eastern Tibetan Plateau: constraints from 40Ar/39Ar K-feldspar and apatite fission track data. J Asian Earth Sci 25:915-935. doi:10.1016/j.jseaes.2004.09.002.

Reid AJ, Wilson CJL, Liu S (2005a) Structural evidence for the Permo-Triassic tectonic evolution of the Yidun Arc, eastern Tibetan plateau. J Struct Geol 27(1):119-137. doi:10.1016/j.jsg.2004.06.011.

Roger F, Jolivet M, Malavieille J (2008) Tectonic evolution of the Triassic fold belts of Tibet. C. R. Geoscience 340:180-189. doi:10.1016/j.crte.2007.10.014.

Sampe T, Xie SP (2010) Large-Scale Dynamics of the Meiyu-Baiu Rainband: Environmental Forcing by the Westerly Jet. J. Clim. 23:113-134.

Schiemann R, Luthi D, Schar C (2009) Seasonality and Interannual Variability of the Westerly Jet in the Tibetan Plateau Region. J. Clim. 22:2940-2957. doi:10.1175/2008JCLI2625.1.

sediments: Strategies from Lake Suigetsu. PAGES magazine 22:12-13.

Shankmann D, Keim BD, Song J (2006) FLOOD FREQUENCY IN CHINA'S POYANG

LAKE REGION: TRENDS AND TELECONNECTIONS. Int. J. Climatol. 26:1255-1266.

Shen C, Wang WC, Hao Z, Gong W (2007) Exceptional drought event over eastern China during the last five centuries. Clim. Change. 85:453-471.

Song B, Li Z, Saito Y, Okuno J, Li Z, Lu A, Hua D, Li J, Li Y, Nakashima R (2013) Initiation of the Changjiang (Yangtze) delta and its response to the mid-Holocene sea level change. Palaeogeogr. Palaeoclimatol. Palaeoecol. 388:81-97.

Sugisaki S, Buylaert J-P, Murray A, Tada R, Zheng H, Wang K, Saito S, Chao L, Li Shiyi, Irino T (2015) OSL dating of fine-grained quartz from Holocene Yangtze delta sediments. Quat. Geochronol. 30:226-232.

Sun Y, Tada R, Chen J, Chen H, Toyoda S, Tani A, Isozak Y, Nagashima K, Hasegawa H, Ji J (2007) Distinguishing the sources of Asian dust based on electron spin resonance signal intensity and crystallinity of quartz. Atmos Environ 41:8537-8548. doi:10.1016/j.atmosenv.2007.07.014.

Tada R, Sato S, Irino T, Matsui H, Kennett JP (2000) Millennial-scale compositional variations in late Quaternary sediments at site 1017, southern California, Proc. Ocean Drill. Program Sci. Results 167:277-296. doi:10.2973/odp.proc.sr.167.222.2000.

Tada R, Zheng H, Clift PD, (2016) Evolution and variability of the Asian monsoon and its potential linkage with uplift of the Himalaya and Tibetan Plateau. Progr Earth Planet

Sci 3:4. doi: 10.1186/s40645-016-0080-y.

Teraoka Y, Okamura K (2003) Geological map of East Asia. Geological Survey of Japan, AIST.

Teraoka Y, Okamura K (2007) Geological map of Central Asia. Geological Survey of Japan, AIST.

Toyoda S (1992) Production and decay characteristics of paramagnetic defects in quartz: applications to ESR dating. Ph.D. thesis, Osaka University, Toyonaka, Osaka, Japan.

Toyoda S, Hattori W (2000) Formation and decay of the E1' center and of its precursor. Appl Radiat Isot 52:1351-1356.

Toyoda S, Naruse T (2002) Eolian dust from the Asian deserts to the Japanese islands since the Last Glacial Maximum: the basis for ESR method. Transactions, Jpn Geomorphol Union 23:811-820.

USGS (2004) Shuttle Radar Topography Mission, 3 Arc Second , Version 2.1, Global Land Cover Facility, University of Maryland, College Park, Maryland, February 2000.

Wang B, Lin H (2002) Rainy Season of the Asian-Pacific Summer Monsoon. J clim 15(4):386-398. doi:10.1175/1520-0442(2002)015<0386:RSOTAP>2.0.CO;2.

Wang B, Wu Z, Li J, Liu J, Chang CP, Ding Y, Wu G (2008) How to Measure the Strength of the East Asian Summer Monsoon. J. Clim. 21:4449-4463. doi:

10.1175/2008JCLI2183.1.

Wang HJ, Sun JQ, Chen HP, Zhu YL, Zhang Y, Jiang DB, Lang XM, Fan K, Yu ET, Yang S (2012a) Extreme Climate in China: Facts, Simulation and Projection. Meteorol. Z. 21(3):379-304. doi: 10.1127/0941-2948/2012/0330.

Wang MJ, Zheng H, Xie X, Fan DD, Yang SY, Zhao QH, Wang K (2010b) A 600-year flood history in the Yangtze River drainage: Comparison between a subaqueous delta and historical records. Chinese Sci. Bull. 56(2):188-195.

Wang X, Ma H, Li R, Song Z, Wu J (2012b) Seasonal fluxes and source variation of organic carbon transported by two major Chinese Rivers: The Yellow River and Changjiang (Yangtze) River. Global Biogeochem. Cycles 26:GB2025.

Wang X, Metcalfe I, Jian P, He L, Wang C (2000) The Jinshajiang-Ailaoshan Suture Zone, China: tectonostratigraphy, age and evolution. J Asian Earth Sci 18(6):675-690. doi:10.1016/S1367-9120(00)00039-0.

Wang X-L, Zhou J-C, Griffin WL, Wang R-C, Qiu J-S, O'Reilly SY, Xu X, Liu X-M, Wang X-L (2007a) Detrital zircon geochronology of Precambrian basement sequences in the Jiangnan orogen: Dating the assembly of the Yangtze and Cathaysia Blocks. Precambrian Res 159:117-131. doi:10.1016/j.precamres.2007.06.005.

Wang Y, Cheng H, Edwards L, He Y, Kong X, An Z, Wu J, Kelly M-J, Dykoski C-A, Li

X (2005) The Holocene Asian Monsoon: Links to Solar Changes and North Atlantic Climate. Science 308:854-857. doi:10.1126/science.1106296.

Wang Y, Fan W, Zhang G, Zhang Y (2013) Phanerozoic tectonics of the South China Block: Key observations and controversies. Gondwana Res 23:1273-1305. doi:10.1016/j.gr.2012.02.019.

Wang Y, Zhanf F, Fan W, Zhang G, Chen S, Cawood PA, Zhang A (2010a) Tectonic setting of the South China Block in the early Paleozoic: Resolving intracontinental and ocean closure models from detrital zircon U-Pb geochronology. Tectonics 29:TC6020. doi:10.1029/2010TC002750.

Wang Z-Y, Li Y, He Y (2007b) Sediment budget of the Yangtze River. Water Resour Res 43:W04401. doi:10.1029/2006WR005012.

Wu W, Xu S, Yang J, Yin H, Tao X (2009) Sr fluxes and isotopic compositions in the headwaters of the Yangtze River, Tongtian River and Jinsha River originating from the Qinghai-Tibet Plateau. Chem Geol 260:63-72. doi:10.1016/j.chemgeo.2008.12.007.

Xia L, Li X, Ma Z, Xu X, Xia Z (2011) Cenozoic volcanism and tectonic evolution of the Tibetan plateau. Gondwana Res 19:850-866. doi:10.1016/j.gr.2010.09.005.

Xu K, Milliman JD, Xu H (2010) Temporal trend of precipitation and runoff in major Chinese Rivers since 1951. Global Planet Change 73:219-232.

doi:10.1016/j.gloplacha.2010.07.002.

Xu T, Wang G, Shi X, Wang X, Yao Z, Yang G, Fang X, Qiao S, Liu S, Wang X, Zhao Q (2016) Sequence stratigraphy of the subaqueous Changjiang (Yangtze River) delta since the Last Glacial Maximum. Sed. Geol. 331:132-147.

Yang S-L, Milliman JD, Xu K-H, Deng B, Zhang XX, Luo XX (2014) Downstream sedimentary and geomorphic impacts of the Three Gorges Dam on the Yangtze River. Earth Sci Rev 138:469-486. doi: 10.1016/j.earscirev.2014.07.006.

Yang S-L, Zhang J, Xu XJ (2007) Influence of the Three Gorges Dam on downstream delivery of sediment and its environmental implications, Yangtze River. Geophys Res Lett 34:L10401. doi:10.1029/2007GL029472.

Yang S-L, Zhao Q-Y, Belkin IM (2002) Temporal variation in the sediment load of the Yangtze river and the influences of human activities. J Hydrol 263:56-71. doi:10.1016/S0022-1694(02)00028-8.

Yang Z, Wang H, Saito Y, Milliman JD, Xu K, Qiao S, Shi G (2006) Dam impacts on the Changjiang (Yangtze) River sediment discharge to the sea: The past 55 years and after Three Gorges Dam. Water Resour Res 42:W004407. doi:10.1029/2005WR003970.

Yi L, Yu H, Ge J, Lai Z, Xu X, Qin L, Peng S (2012) Reconstructions of annual summer precipitation and temperature in north-central China since 1470 AD based on

drought/flood index and tree-ring records. Clim. Change 110:469-498.

Yin A, Harrison TM (2000) Geologic evolution of the Himalayan-Tibetan orogen. Annu. Rev. Earth Planet. Sci. 2000. 28:211-80. doi:10.1146/annurev.earth.28.1.211

Yin H, Liu G, Pi J, Chen G, Li C (2007) On the river-lake relationship of the middle Yangtze reaches. Geomorphology 85:197-207. doi:10.1016/j.geomorph.2006.03.017.

Zhang J, Chen F, Holmes JA, Li H, Guo X, Wang J, Li S, Lu Y, Zhao Y, Qiang M (2011) Holocene monsoon climate documented by oxygen and carbon isotopes from lake sediments and peat bogs in China: a review and synthesis. Quaternary Sci. Rev. 30:1973-1987. doi:10.1016/j.quascirev.2011.04.023.

Zhang Q, Gemmer M, Chan J (2008b) Climate changes and flood/drought risk in the Yangtze Delta, China, during the past millennium. Quaternary Int. 176-177:62-69.

Zhang Q, Liu C, Yu C, Xu Y, Jiang T (2006) Observed trends of annual maximum water level and streamflow during past 130 years in the Yangtze River basin, China. J. Hydrol. 324:255-265.

Zhang Q, Xu C-Y, Zhang Z, Chen YD, Liu C-L, Lin H (2008a) Spatial and temporal variability of precipitation maxima during 1960-2005 in the Yangtze River basin and possible association with large-scale circulation. J Hydrol 353:215-227. doi:10.1016/j.jhydrol.2007.11.023.

Zhang Y, Huang CC, Pang J, Zha X, Zhou Y, Yin S, Wang J (2012) Comparative study of the modern flood slackwater deposits in the upper reaches of Hanjiang and Weihe River Valleys, China. Quat Int 282:184-191. doi:doi:10.1016/j.quaint.2012.03.056.

Zhou L, Liu J, Saito Y, Zhang Z, Chu H, Hu G (2014) Coastal erosionasamajorsedimentsuppliertocontinentalshelves: examplefromtheabandonedOldHuanghe(YellowRiver)delta. Continental Shelf Res. 82:43-59. doi:10.1016/j.csr.2014.03.015.

Zhou XJ, Zhao P, Liu G, Zhou TJ (2011) Characteristics of decadal-centennial-scale changes in East Asian summer monsoon circulation and precipitation during the Medieval Warm Period and Little Ice Age and in the present day. Chinese Sci. Bull. 56(28-29):3003-3011. doi: 10.1007/s11434-011-4651-4.

Zong Y, Chen X (2000) The 1998 Flood on the Yangtze, China. Nat Hazards 22:165-184. doi:10.1023/A:1008119805106.

Table 1.1 Ranges of ESR and CI values for each tributary in the fine-silt fraction (4-16 μm)

Tributary	**ESR signal intensity**			**CI values**		
	Minimum	Maximum	Average	Minimum	Maximum	Average
Jinshajiang	0.00	3.23	1.39	8.31	8.79	8.66
Minjiang	0.00	5.26	2.14	8.83	8.67	8.57
Jialingjiang	1.46	10.9	5.96	8.59	8.67	8.63
Wujiang	13.4	15.5	14.6	8.71	8.81	8.81
Dongting Lake	11.3	23.4	15.9	8.87	8.68	8.37
Hanjiang	8.76	9.45	9.10	8.27	8.44	8.35
Poyang Lake	12.2	12.2	12.2	8.58	8.58	8.58

Table 1.2 Predicted and analyzed ESR signal intensity of the mainstream below the junction with tributaries

Tributary	**ESR signal intensity**	
	Predicted	Analyzed
Minjiang	1.34	1.49
Jialingjiang	2.23	3.88
Wujiang	4.27	7.92
Poyang Lake	5.19	3.74

Table 1.3 Predicted and analyzed ESR and CI values along the mainstream in the fine-silt fraction (4-16 μm)

Location	**Predicted**						**Analyzed**	
	ESR signal intensity			CI values			ESR	CI
	Minimum	Maximum	Average	Minimum	Maximum	Average		
Above MJ (Jinshajiang)	0.0	3.2	1.8	8.3	8.8	8.7	1.9	8.7
Below MJ / above JLJ	0.0	3.5	1.9	8.3	8.8	8.6	1.5	7.9
Below JLJ / above WJ	0.3	4.8	2.6	8.4	8.7	8.6	3.9	8.6
Below WJ / TGD input	0.9	5.3	3.1	8.4	8.8	8.7	-	-
Upper area of TGD	0.9	5.3	3.1	8.4	8.8	8.7	4.2	8.7
TGD output	0.9	5.3	3.1	8.4	8.8	8.7	1.8	8.8
Below DTL	2.8	9.1	5.6	8.5	8.7	8.7	9.1	8.7
Above HJ	2.6	8.9	5.3	8.5	8.7	8.7	-	-
Below HJ	3.1	8.9	5.6	8.5	8.7	8.7	7.7	8.7
Above PYL	3.0	9.0	5.6	8.5	8.7	8.6	4.0	8.2
Below PYL	4.0	9.7	6.5	8.5	8.7	8.6	3.8	8.7
Rivermouth	4.0	9.7	6.5	8.5	8.7	8.6	4.4	8.5

Note: MJ: Minjiang; JLJ: Jialingjiang; WJ: Wujiang; TGD: Three Gorges Dam; DTL: Dongting Lake; HJ: Hanjiang; PYL: Poyang Lake

Table 2.1 Drilling depth and composite depth of each core of YD13

Hole	Core	Drilling depth (m)		Offset (m)	Composite depth (m)	
		Top	Bottom		Top	Bottom
1	1	0.00	0.85	1.3	1.30	2.15
1	2	1.00	2.14	1.18	2.18	3.32
1	3	2.20	3.12	1.32	3.52	4.44
1	4	3.20	4.27	1.32	4.52	5.59
1	5	4.40	5.34	1.32	5.72	6.66
1	5.1	4.40	5.34	2.26	6.66	7.60
1	6	5.40	6.19	2.26	7.66	8.45
1	7	6.30	7.30	2.26	8.56	9.56
1	8	7.40	8.11	2.26	9.66	10.37
1	9	8.20	9.09	2.26	10.46	11.35
1	10	9.20	9.64	2.26	11.46	11.9
2	1	0.00	1.10	0.54	0.54	1.64
2	2	1.20	2.30	0.42	1.62	2.72
2	3	2.40	3.20	0.28	2.68	3.48
2	4	3.30	4.230	0.18	3.48	4.41
2	5	4.30	5.40	0.08	4.38	5.48
2	6	5.50	5.96	0.48	5.98	6.44
2	7	6.00	7.13	0.48	6.48	7.61
2	8	7.20	7.78	1.96	9.16	9.74
2	9	7.80	8.49	2.20	10.00	10.69
2	10	8.60	9.60	2.51	11.11	12.11
G2	1	0.00	1.38	0.00	0.00	1.38

Table 2.2 Shell fossils and their radiocarbon ages in YD13

Sample ID	Composite Depth (m)	Libby age (ky)	Error (yr)	Calibrated age (yr BP)		Condition	Type	Species	Habitat
				Median	Range				
YD13 H1C2 17cm	2.35	1815	24	1455	1529-1380				
YD13 H1C2 105cm	3.23	2390	30	2161	2258-2064	Whole	Snail		
YD13 H1C2 110cm	3.28	1631	27	1282	1345-1219	Fragment			
YD13 H2C2 101cm	2.63	2040	30	1721	1807-1634	Whole	Snail		
YD13 H2C4 42cm	3.9	2190	30	1898	1980-1816	Fragment	Snail		
YD13 H2C5 39cm	4.77	2356	34	2090	2191-1989	Whole	Snail	Zeuxis succinctus	Inner bay
YD13 H1C5 81cm	6.53	2570	30	2378	2470-2286	Whole	Bivalve		
YD13 H2C7 96cm	7.44	2617	28	2418	2516-2320	Whole	Snail	Zeuxis castus	Sandy to muddy
YD13 H2C7 102cm	7.5	2480	30	2241	2321-2160	Whole	Snail	NA	
YD13 H2C7 108cm	7.56	2487	36	2245	2330-2160	Whole	Bivalve	Arcosis interplicata	Inner bay

YD13 H1C9 56cm	11.02	4705	31	5093	5207-4978	Whole	Snail	Pristiterebra pumilio	Inner bay
YD13 H2C10 48.5cm	11.595	5740	30	6248	6315-6180	Fragment			
YD13 G2 2cm	0.02	460	20	193	271-115	Fragment	Bivalve	NA	
YD13 H1C9 40cm	10.86	NA	NA	NA	NA	Whole	Snail	Conoidea	NA
YD13 G2 122.5-125cm	1.237	NA	NA	NA	NA	Whole	Snail	Sucaphopoda	NA
YD13 H1C3 9cm	3.61	NA	NA	NA	NA	Whole	Snail	Zeuxis succinctus	Inner bay

Table 2.3 Radiocarbon ages of foraminifera in YD13

Sample ID	Composite Depth (m)	Libby age (ky)	Error (yr)	Calibrated age (yr BP)	
				Median	Range
YD13-1-5 86-88cm	6.59	6470	30	7443	7387-7499
YD13-1-6 26cm	7.92	7120	30	8004	7936-8072
YD13-1-7 2-6cm	8.6	7650	40	8529	8453-8605
YD13-1-7 70-74cm	9.28	7750	30	8588	8517-8658

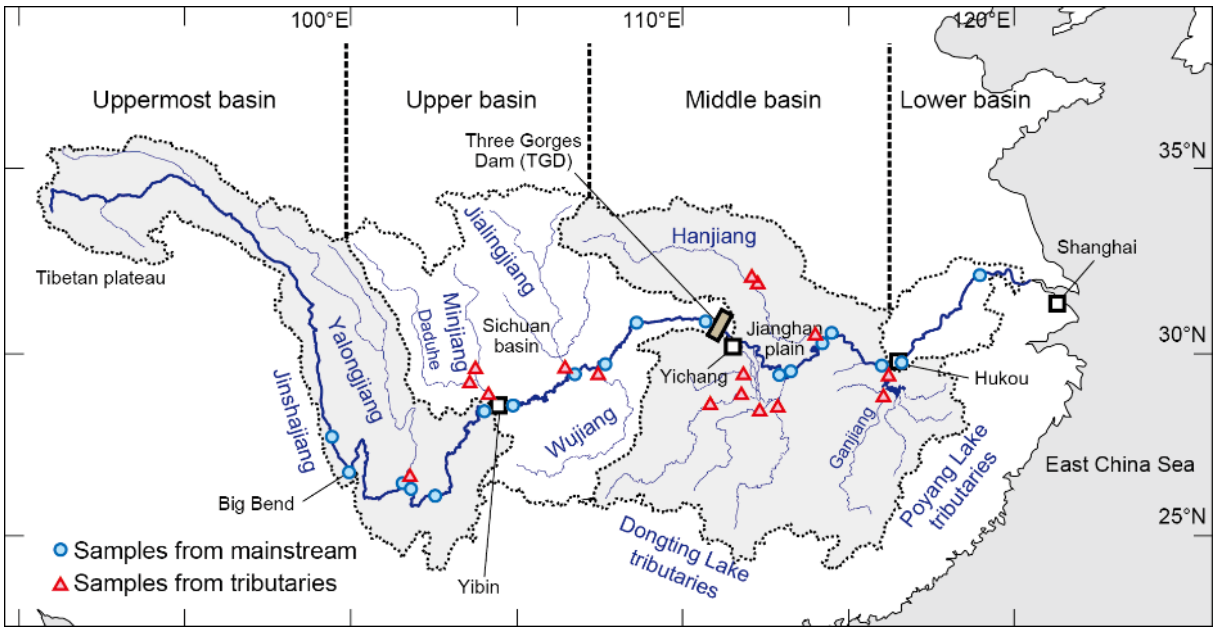

Figure 1.1. A map of the Yangtze River basin and the sampling sites in this study. Also shown is definition of the uppermost, upper, middle, and lower parts of the mainstream and their drainage basins.

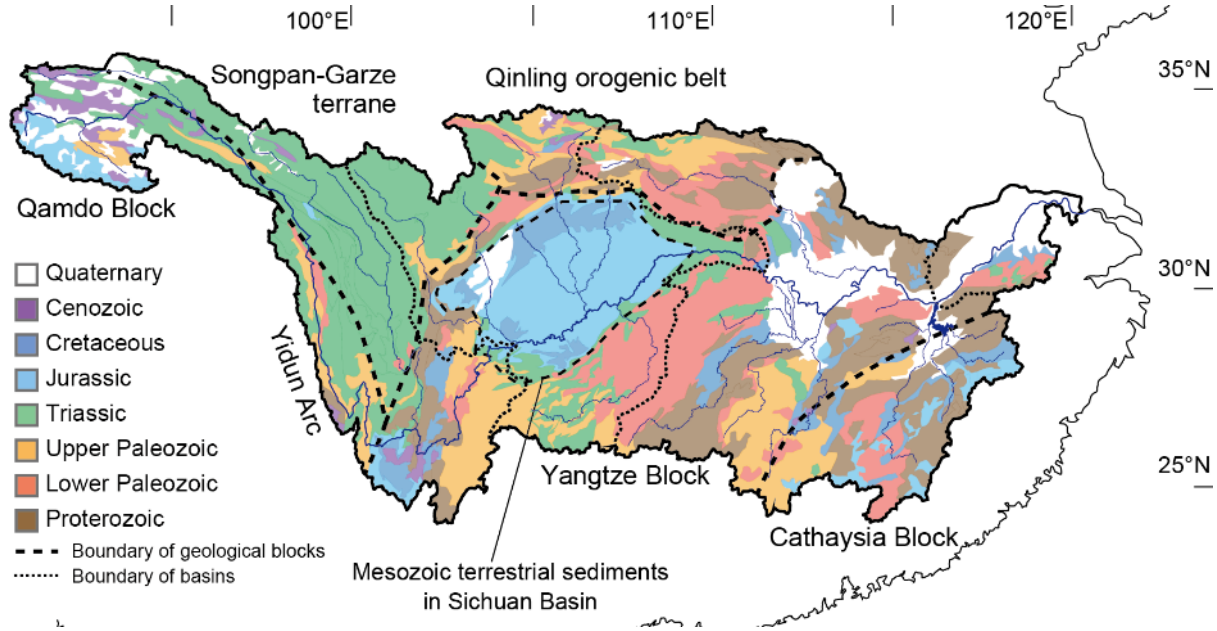

Figure 1.2. A map showing ages of bedrocks in the Yangtze drainage basin. After Teraoka and Okumura (2003, 2007).

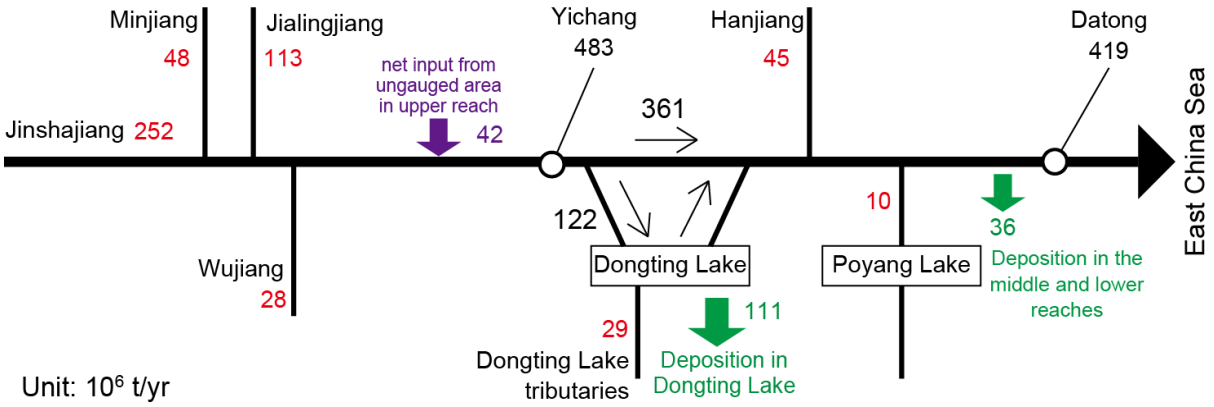

Figure 1.3. Average annual sediment budget in Yangtze drainage basin during 1950-2002 before TGD construction. Based on Dai et al. (2005), Hu et al. (2009), and Yang et al. (2006). Green arrows show deposition in the mainstream and lakes. Purple arrows show sediment inputs from the ungauged area.

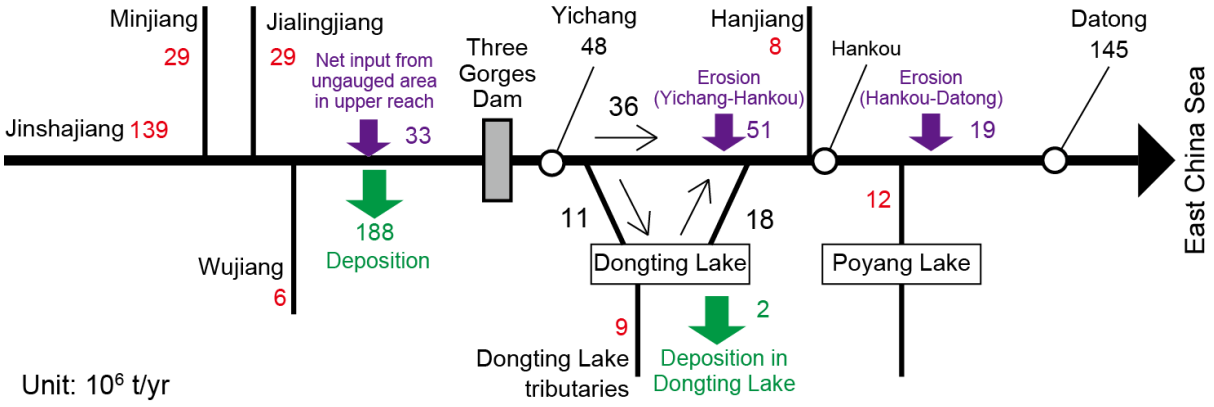

Figure 1.4. Average annual sediment budget in Yangtze drainage basin during 2003-2012 after TGD construction. Based on Yang et al. (2014). Green arrows show deposition in the mainstream and lakes. Purple arrows show sediment inputs from the ungauged area.

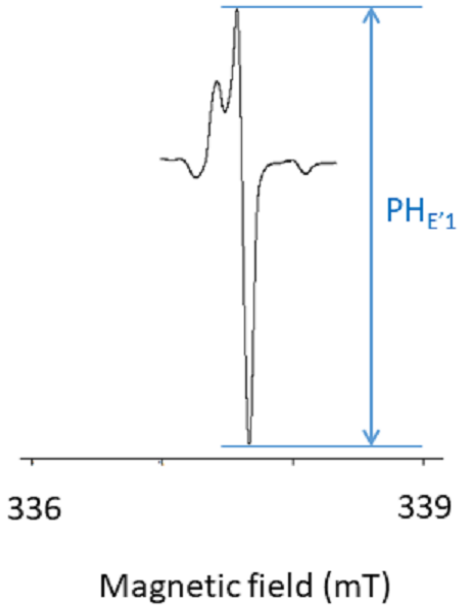

Figure 1.5(a) A typical peak of E1' center of quartz acquired by the ESR spectrometer.

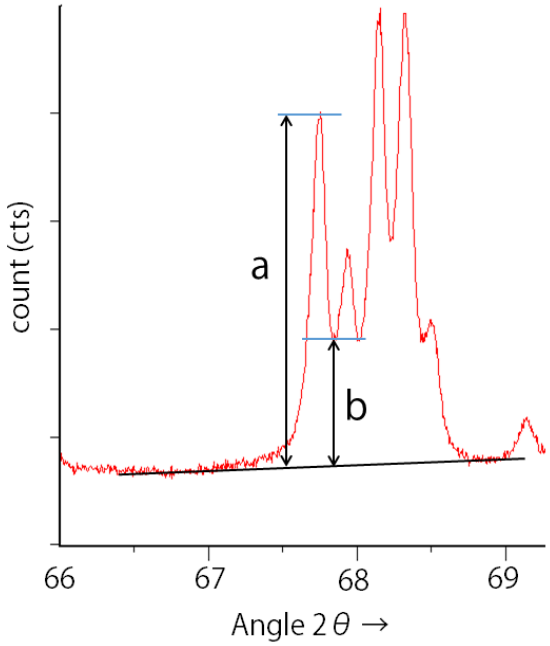

$$CI = (a-b) / a * F$$

Figure 1.5(b) A typical XRD profile of quartz (2θ=66-69˚) and the formula for calculating CI.

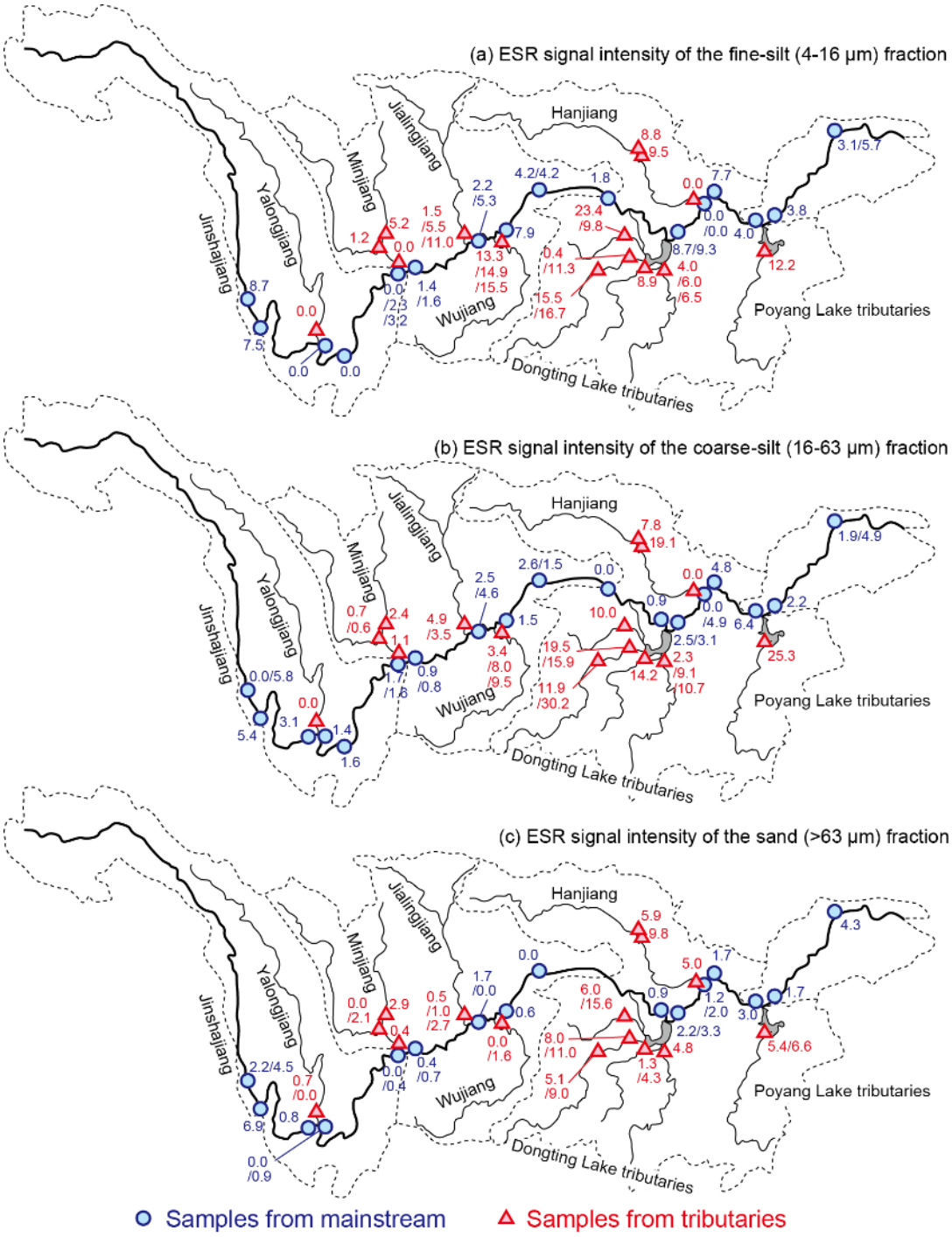

Figure 1.6. Geographical distribution of Electron spin resonance (ESR) signal intensity of quartz in riverbed samples. (a) the sand (>63 μm) fraction; (b) the coarse-silt (16-63μm) fraction; and (c) the fine-silt (4-16 μm) fraction. "/" indicates the values of different samples collected from places in close proximity.

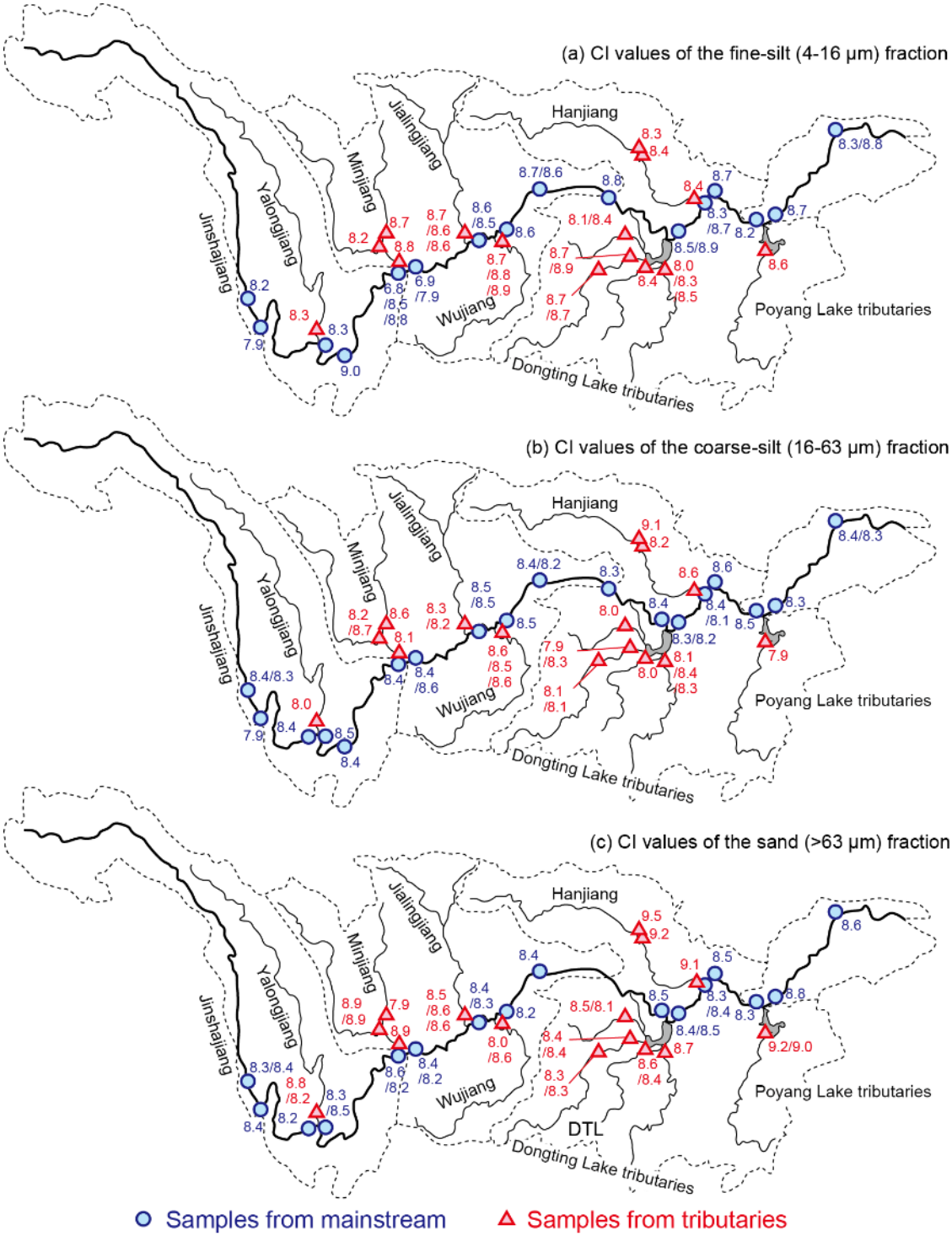

Figure 1.7. Geographical distribution of crystallinity index (CI) signal intensity of quartz in riverbed samples. (a) the sand (>63 μm) fraction; (b) the coarse-silt (16-63μm) fraction; and (c) the fine-silt (4-16 μm) fraction. "/" indicates the values of different samples collected from places in close proximity.

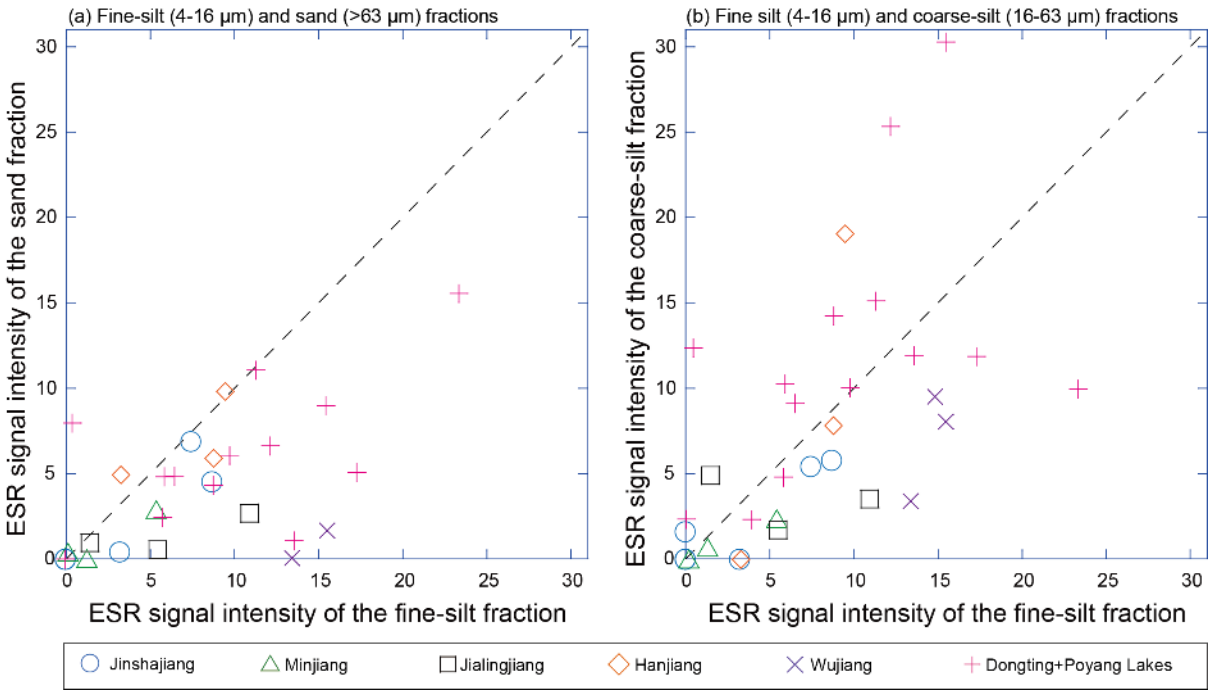

Figure 1.8. Comparison of electron spin resonance (ESR) signal intensity among three size fractions of riverbed samples collected in this study. (a) fine-silt versus sand fractions; (b) fine-silt versus coarse-silt fractions.

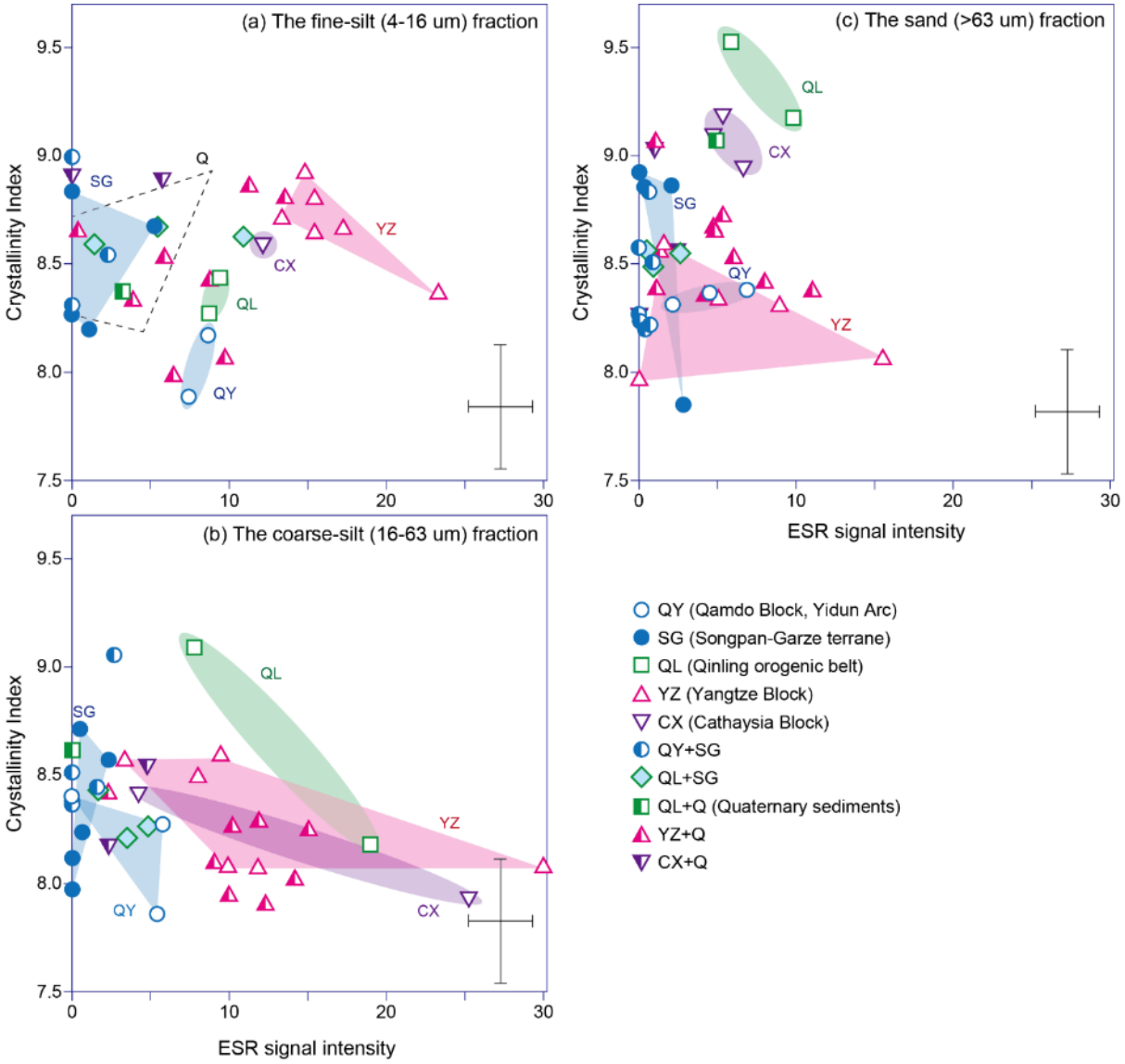

Figure 1.9. ESR-CI plot for riverbed sediments from each geological blocks within the Yangtze drainage basin. (a) the fine-silt (4-16 μm) fraction; (b) the coarse-silt (16-63μm) fraction; and (c) the sand (>63 μm) fraction. QY: Qamdo Block and Yidun Arc; SG: Songpan-Garze Terrane; QL: Qinling Orogenic Belt; YZ: Yangtze Block; CX: Cathaysia Block; Q: Quaternary sediments around the middle-lower parts of the mainstream.

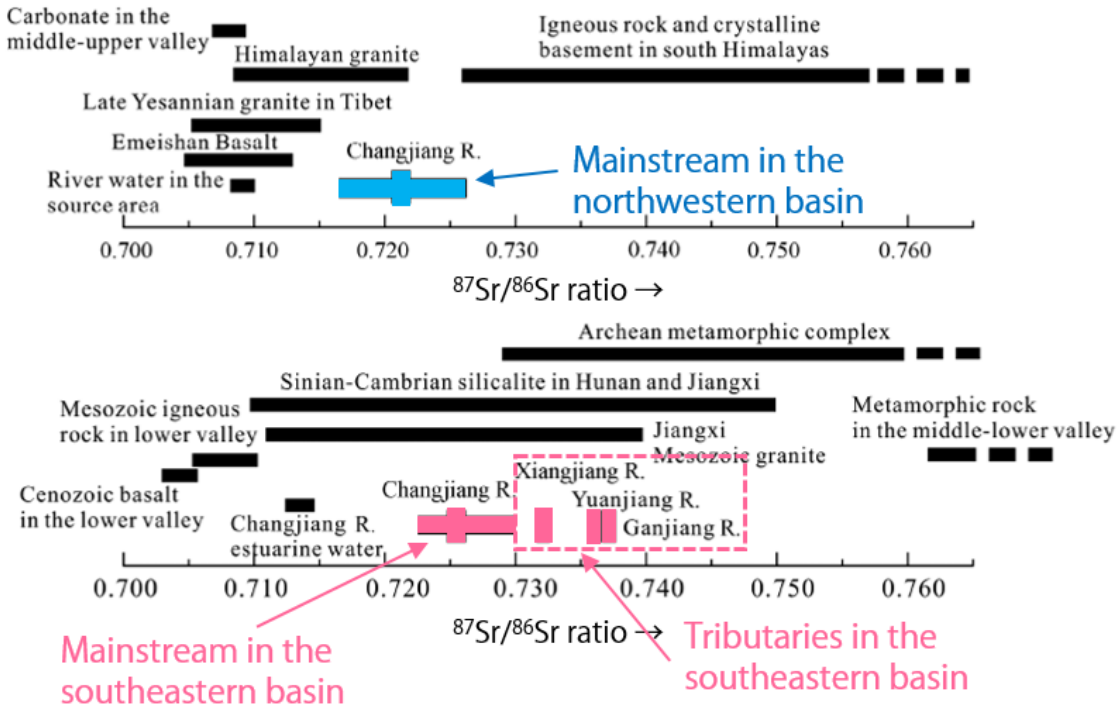

Figure 1.10. 87Sr/86Sr ratio in the Yangtze riverbed sediments and SPM after Yang et al. (2007) compared to the ratio in the bedrocks.

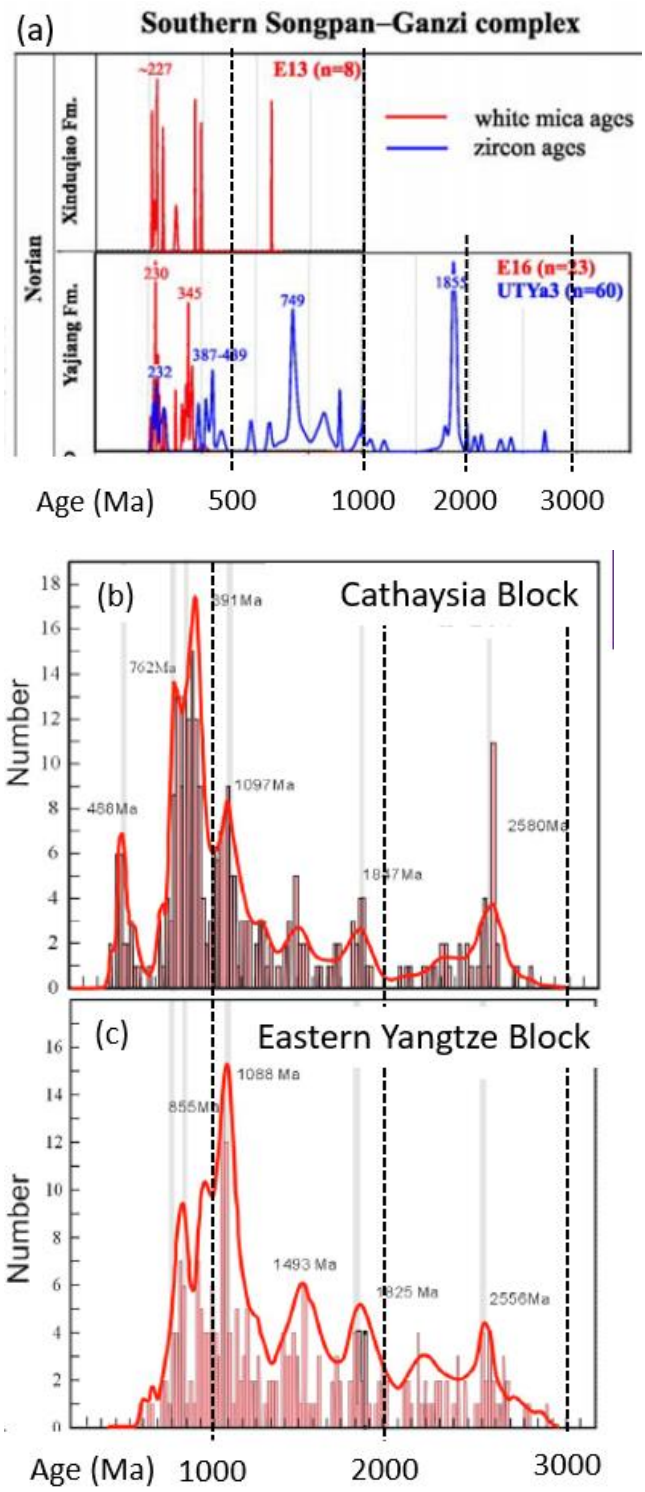

Figure 1.11 Zircon and mica ages acquired within the Yangtze River Basin. (a) Mica and zircon ages of the Songpan-Garze Terrane in the upper to uppermost Yangtze Basin (after Enkelmann et al., 2007). Zircon ages of (b) the Cathaysia Block and (c) the eastern Yangtze Block in the middle Yangtze Basin (after Wang et al., 2010).

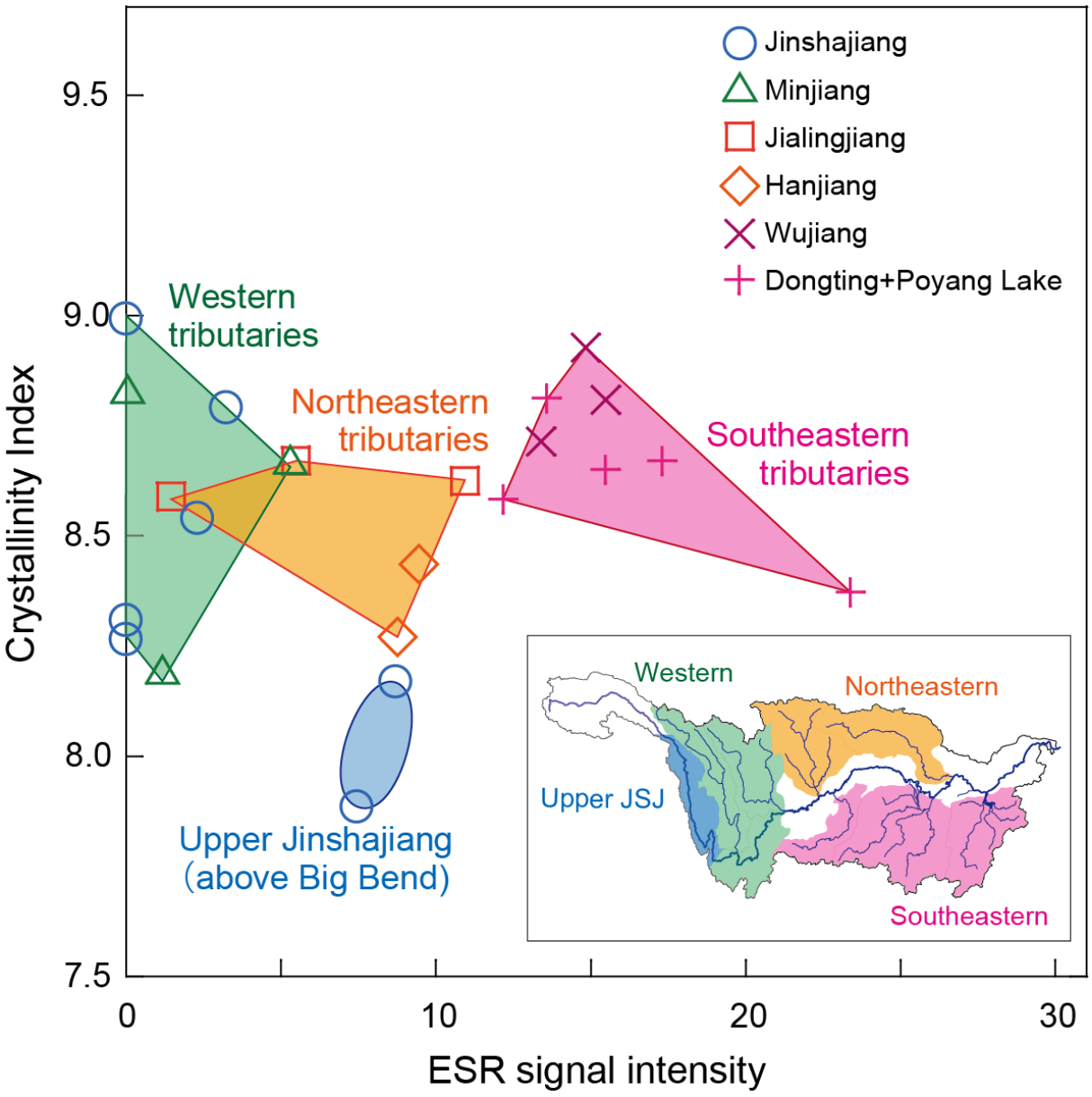

Figure 1.12. ESR-CI plot of quartz in the fine-silt fraction of riverbed samples from the major tributaries.

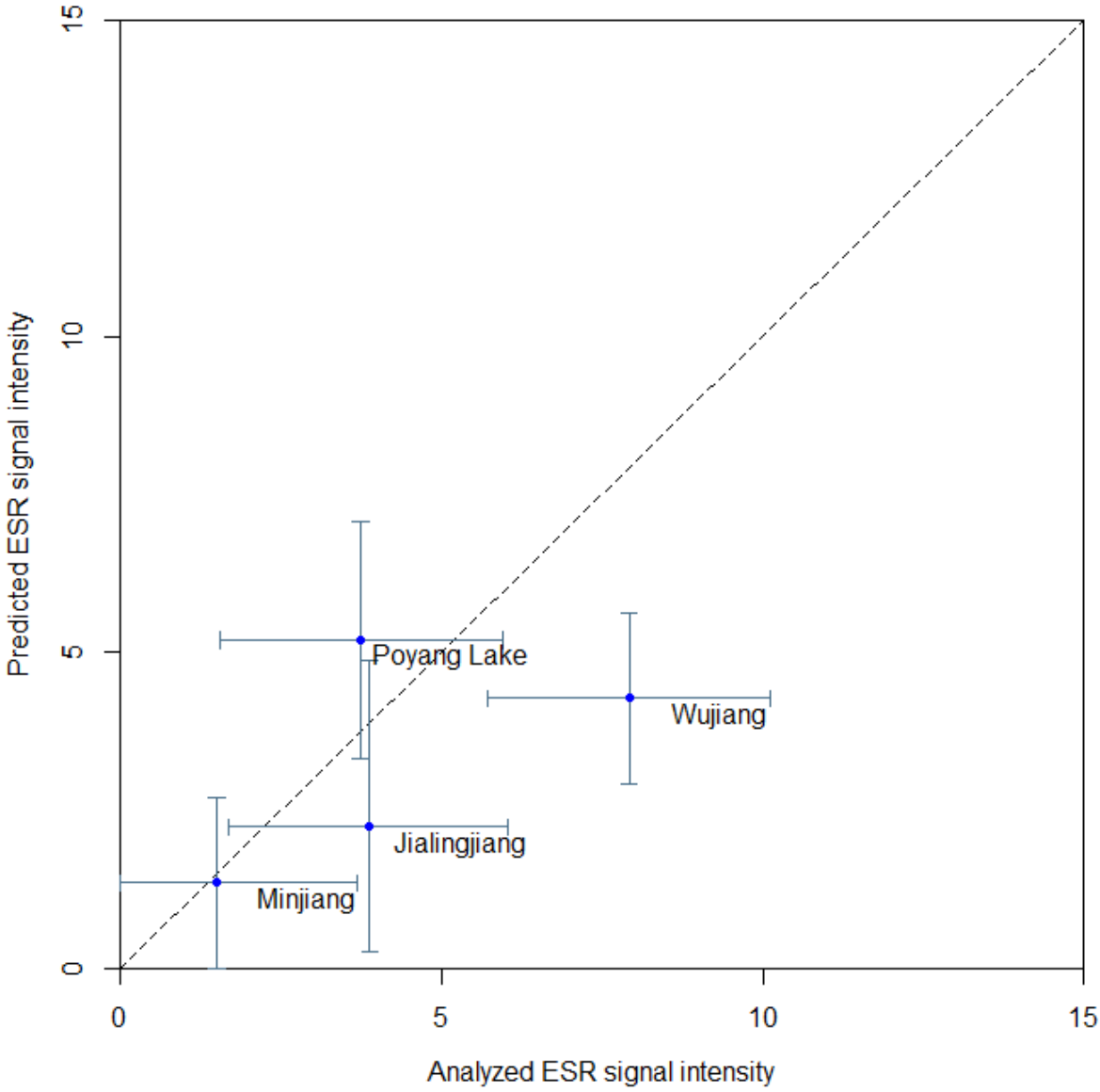

Figure 1.13. Predicted and analyzed ESR signal intensity of quartz below the junction with the tributaries.

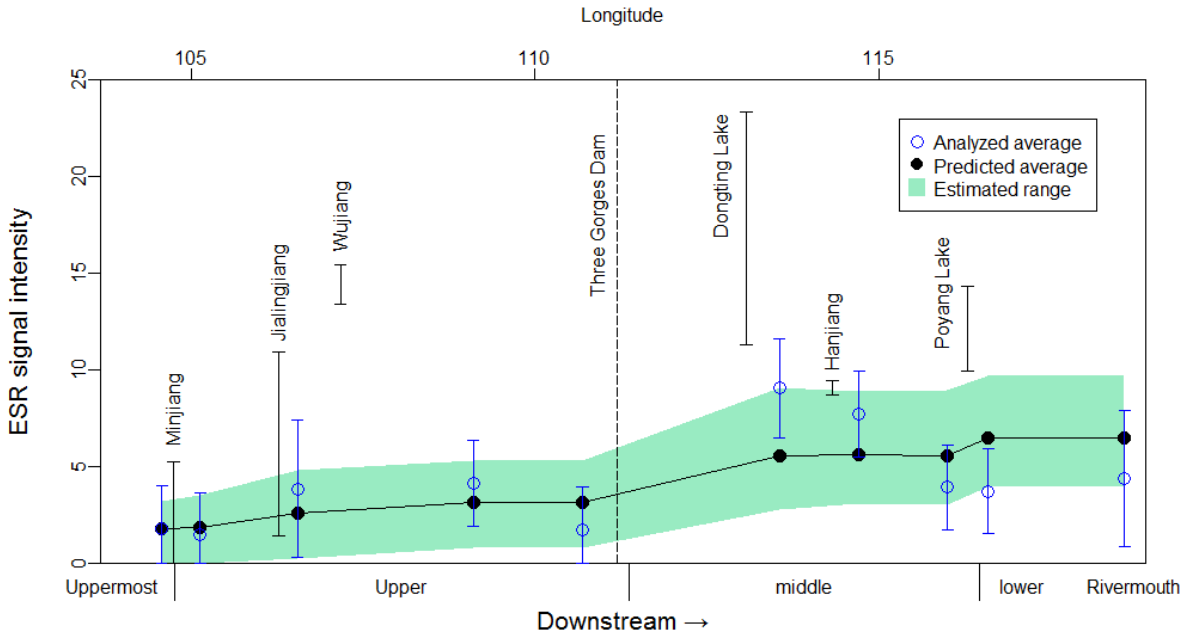

Figure 1.14. Comparison of predicted and analyzed ESR signal intensity of quartz in fine-silt fraction along mainstream. Green area indicates the range of the predicted ESR signal intensity. The solid circles indicate the average of the predicted ESR signal intensity along the mainstream, and the green shaded area indicates the range of the predicted ESR signal intensity, whereas the blue open circles indicate the analyzed ESR signal intensity of the fine-silt fractions at the sites along the mainstream. The samples assumed to be exceptions in the explanation for Figure 10 are omitted in Figure 11, namely a sample collected below the junction with the Wujiang and a sample collected above the junction with the Hanjiang.

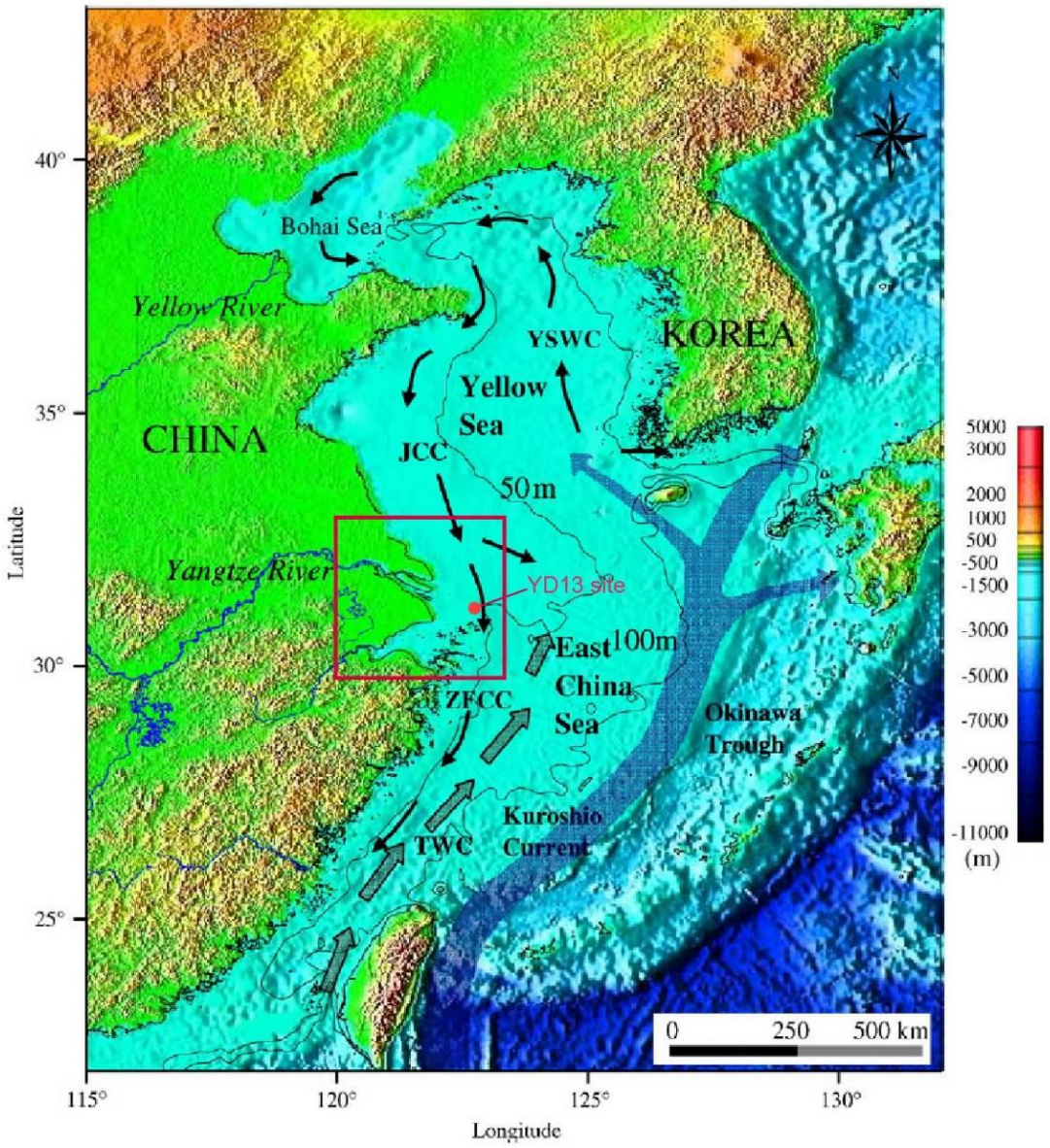

Figure 2.1 Bathymetry and surface currents in the East China Sea (modified from Liu et al., 2007) and the studied site. JCC: Jiangsu Coastal Current; TWC (Taiwan Warm Current); YSWC (Yellow Sea Warm Current); ZFCC (Zhejiang–Fujiang Coastal Current).

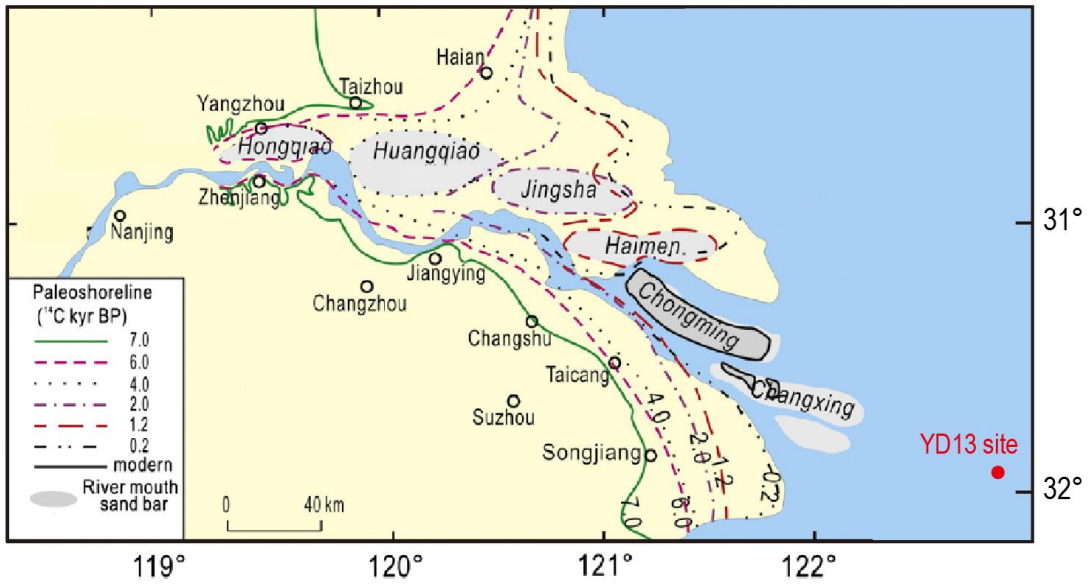

Figure 2.2 Progradation of the subaerial Yangtze delta during the last 7 ky (modified from Song et al., 2013).

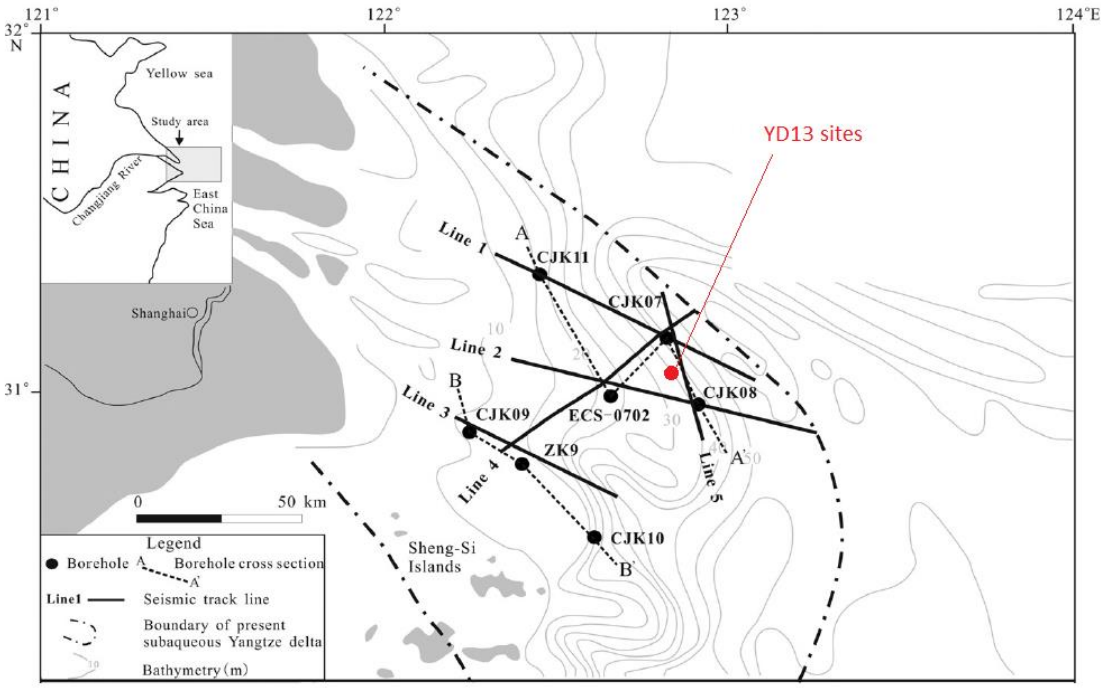

Figure 2.3 Map of seismic transects and sediment cores around the subaqueous Yangtze Delta (modified from Xu et al., 2016)

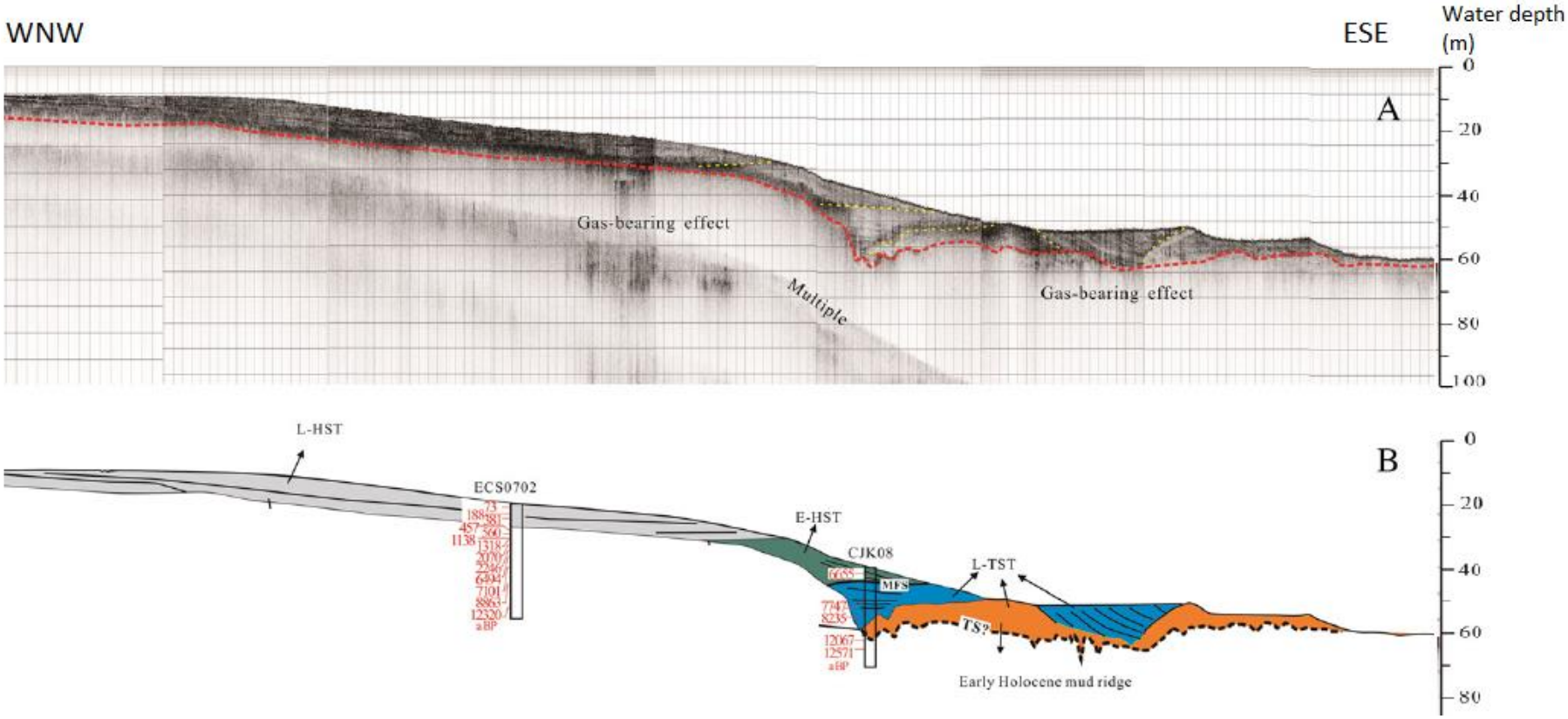
WNW
ESE
Water depth (m)
0
20
40
60
80
100
A
Gas-bearing effect
Multiple
Gas-bearing effect
B
L-HST
ECS0702
E-HST
CJK08
L-TST
MFS
TS?
Early Holocene mud ridge
aBP

Figure 2.4 Seismic profile and its interpretation along lines in Figure 2.3 (modified from Xu et al., 2016). (a) Line 2 in Figure 2.3, (b) correlation between system tract and YD13 lithological units based on the shell-based age. L-TST: Late transgressive system tract; E-HST: Early highstand system tract; L-HST: Late highstand system tract; TS: Transgressive surface; MFS: Maximum flooding surface.

(b)

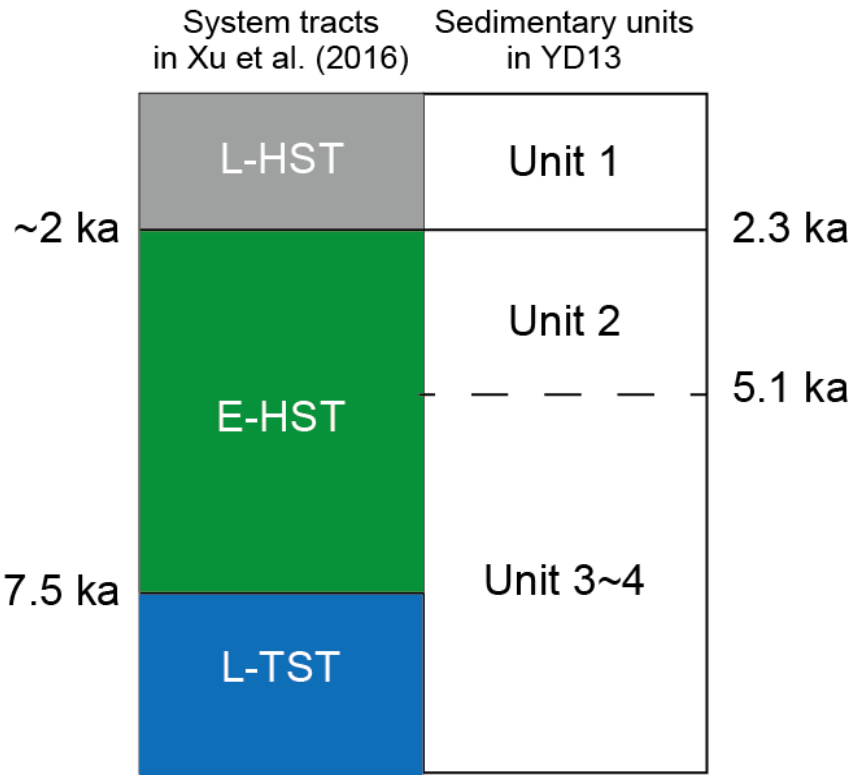

Figure 2.4 (continue)

(a)

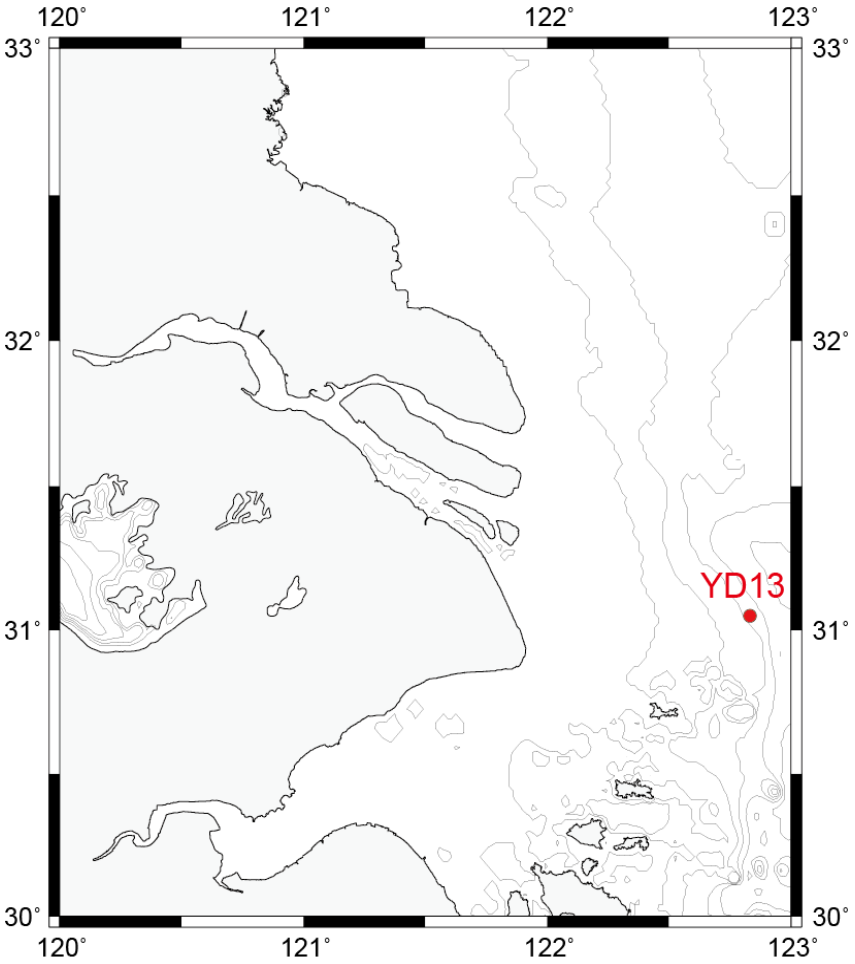

(b)

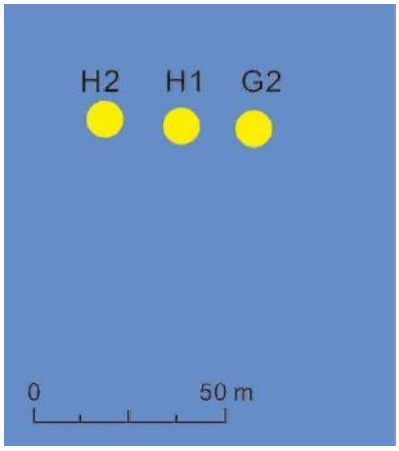

Figure 2.5 (a) YD13 sites and (b) detailed position of Hole 1, Hole 2, and G2.

(a) Hole 1

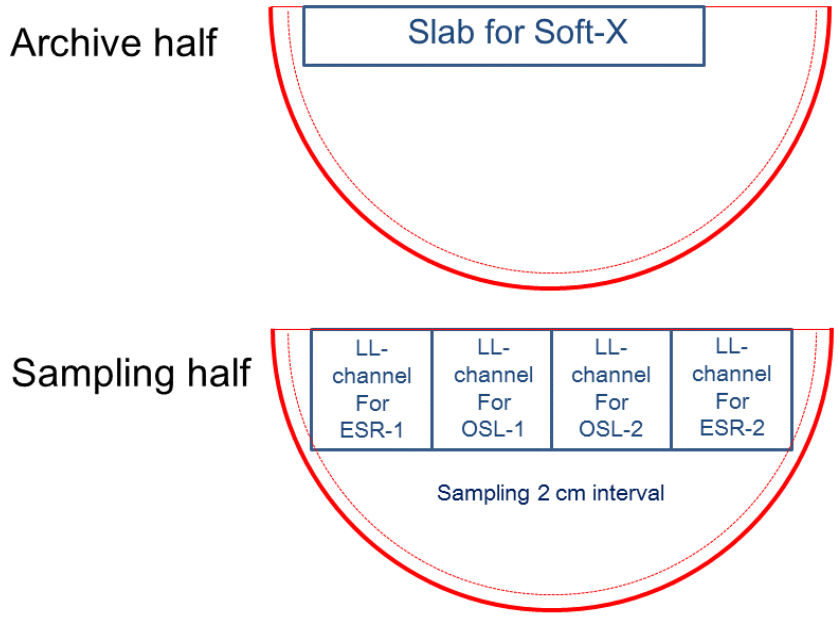

(b) Hole 2

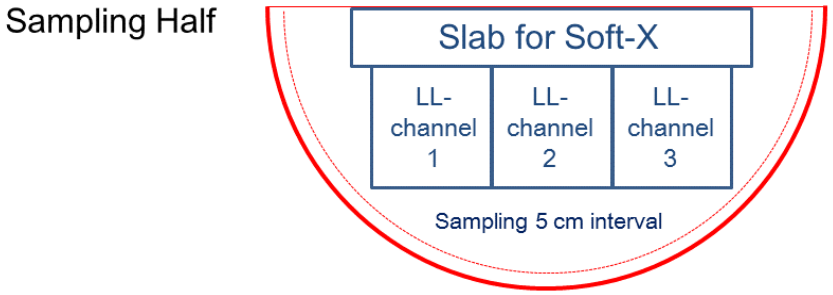

(c) G2

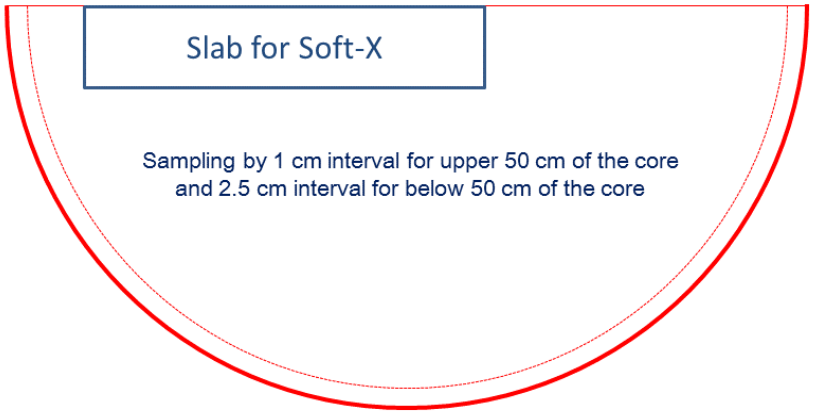

Figure 2.6 Sampling plan for YD13 (a) Hole 1, (b) Hole 2, and (c) G2. Archive half of Hole 2 were not sampled. Two half of G2 were sampled by the same method and interval.

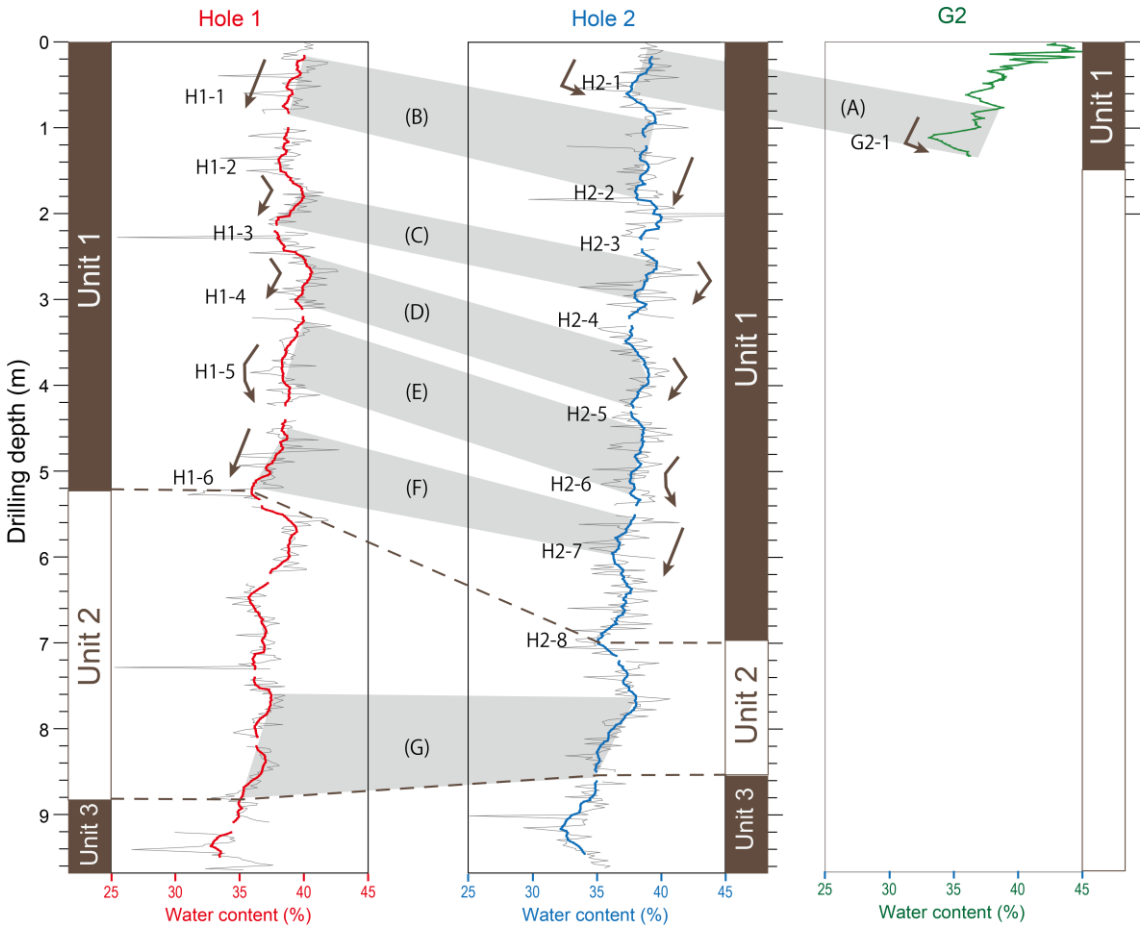

Figure 2.7 Water content in Hole 1, Hole 2, and G2 of YD13 with respect to the drilling depth and the meter-scale correlation (A)~(G) among three holes.

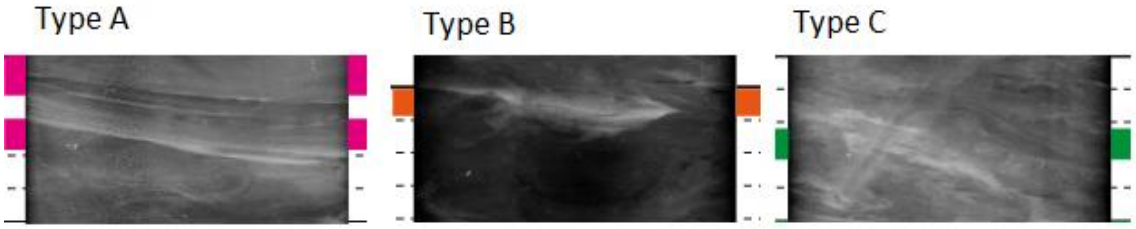

Figure 2.8 Soft-X radiographs of typical event layers for Type A, Type B, and Type C.

(a)

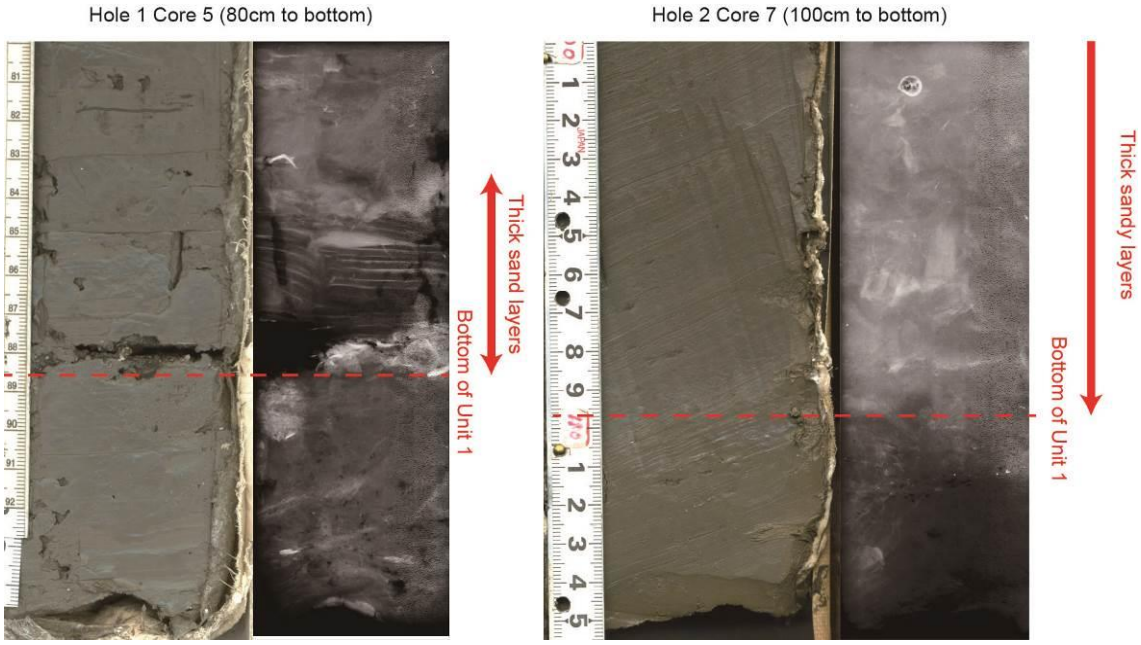

Figure 2.9 Scanned images and Soft-X ray radiographs of the basal sand layer of Unit 1 at Hole 1 and Hole 2.

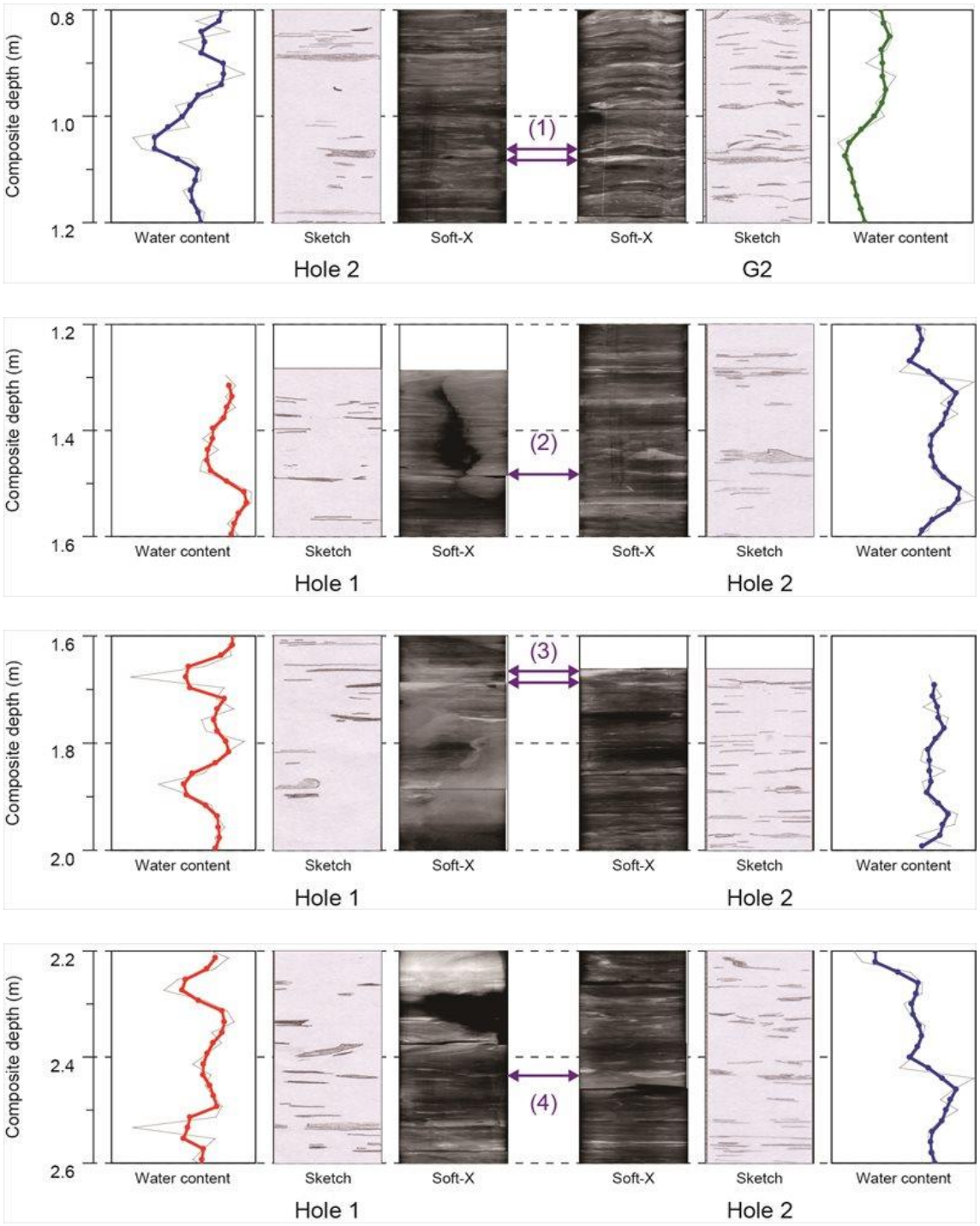

Figure 2.10 Soft-X ray radiograph, sketch, and water content for the layers used for the correlation among Hole 1, Hole 2, and G2.

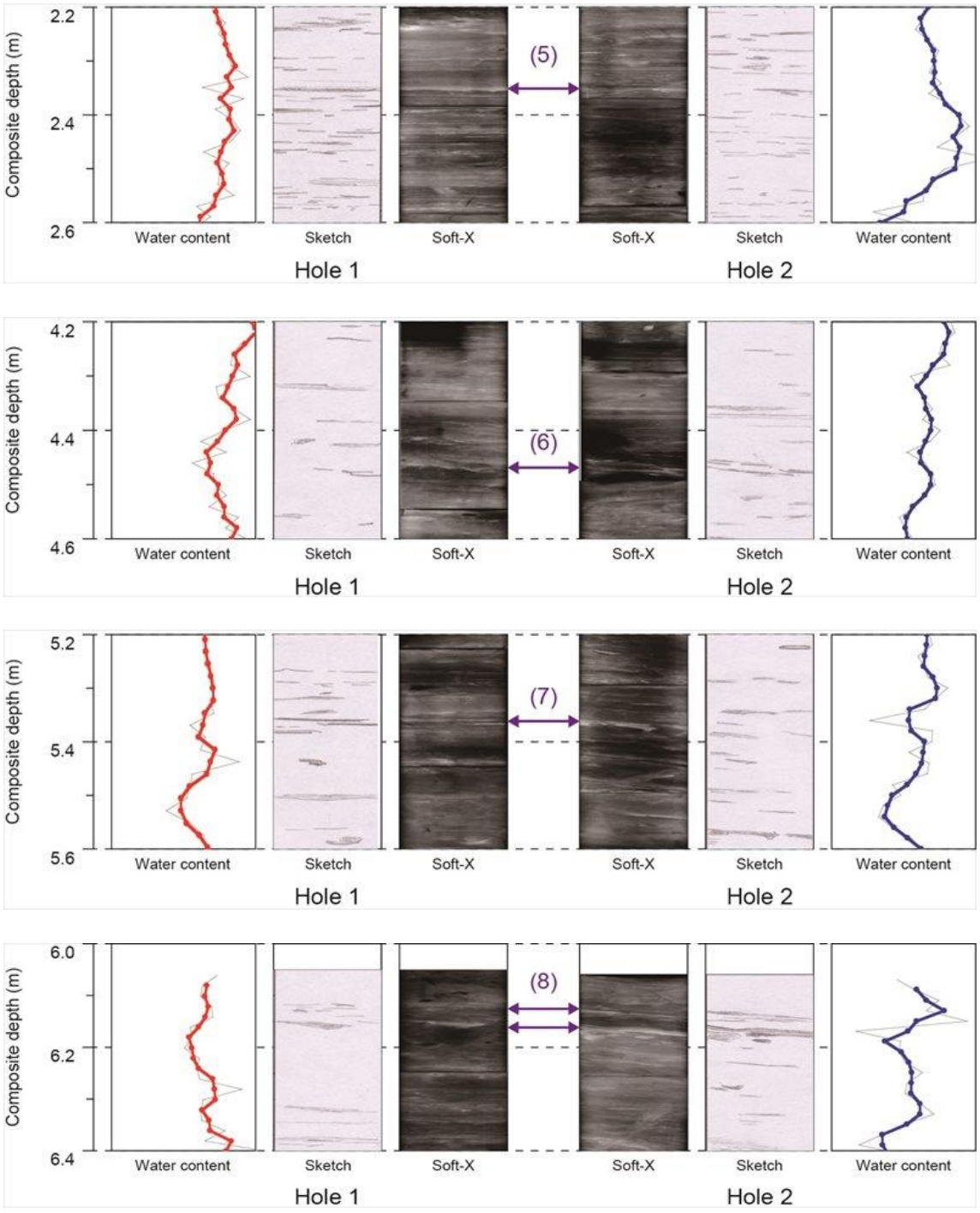

Figure 2.10 (continue)

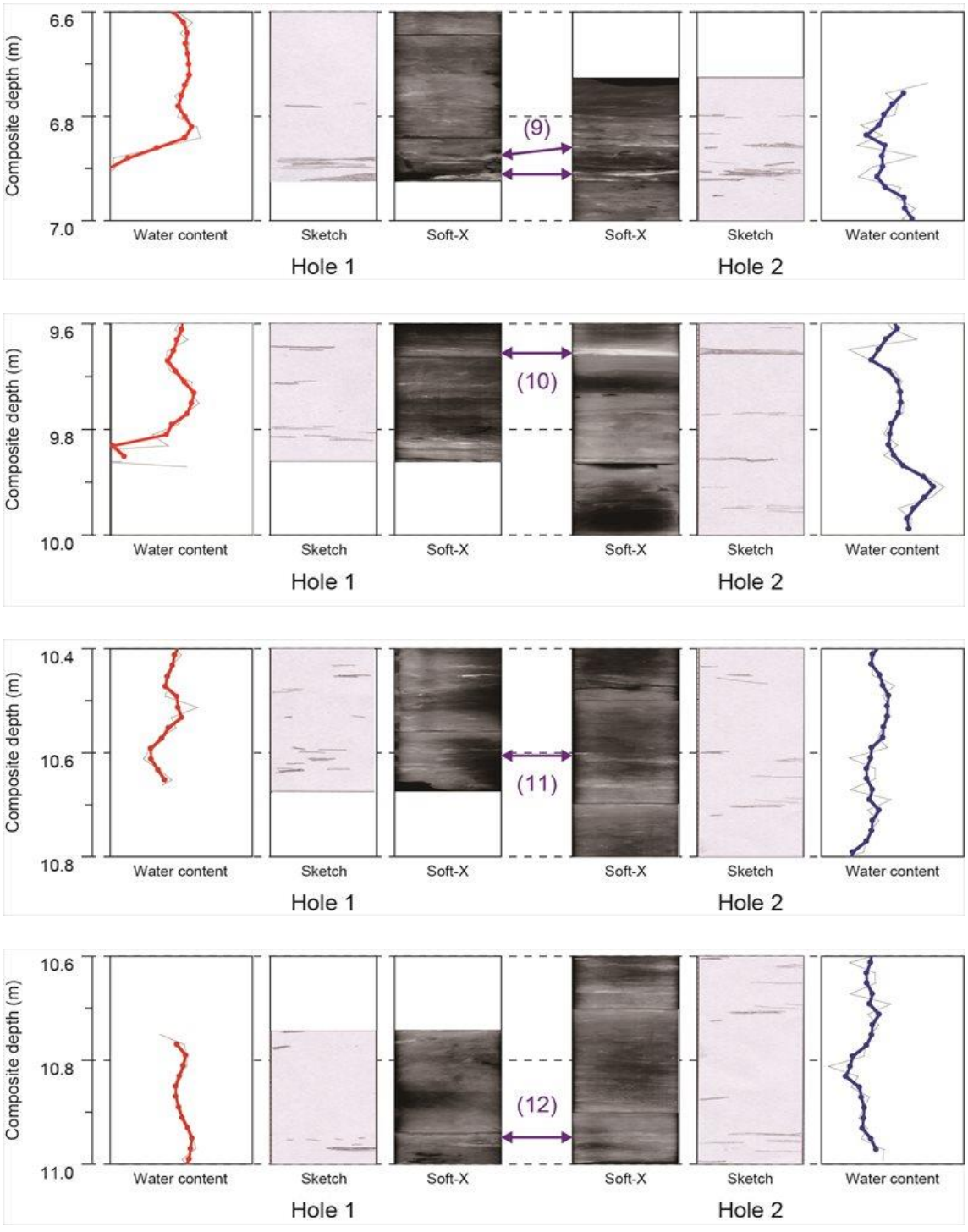

Figure 2.10 (continue)

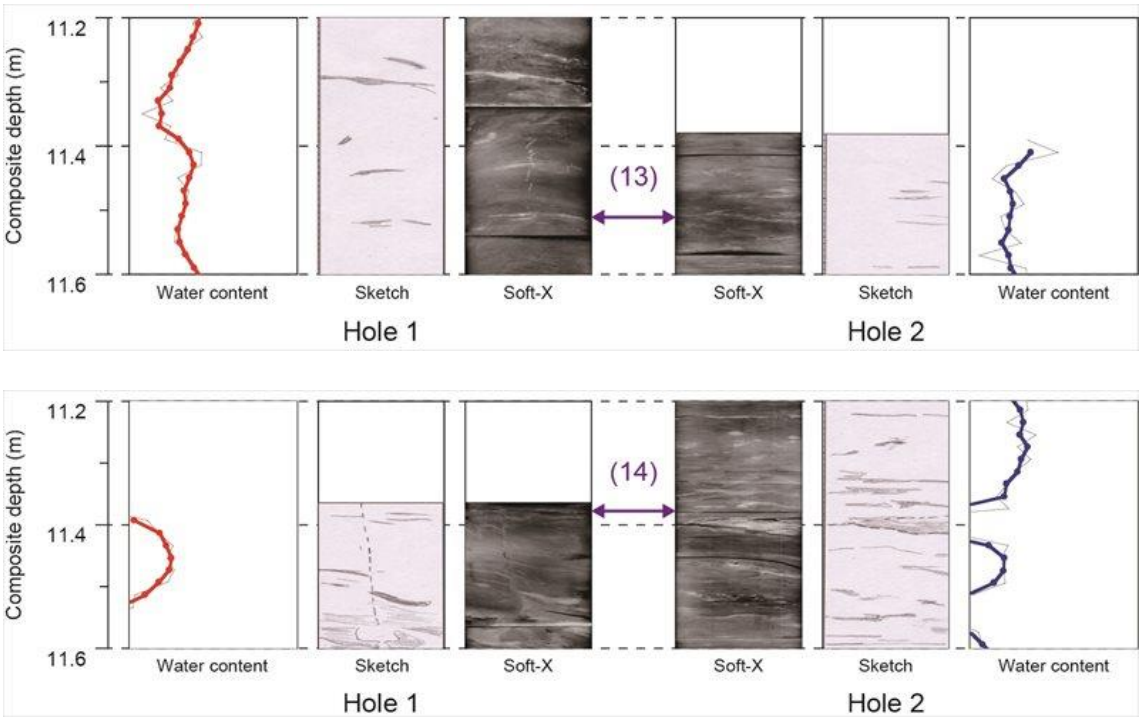

Figure 2.10 (continue)

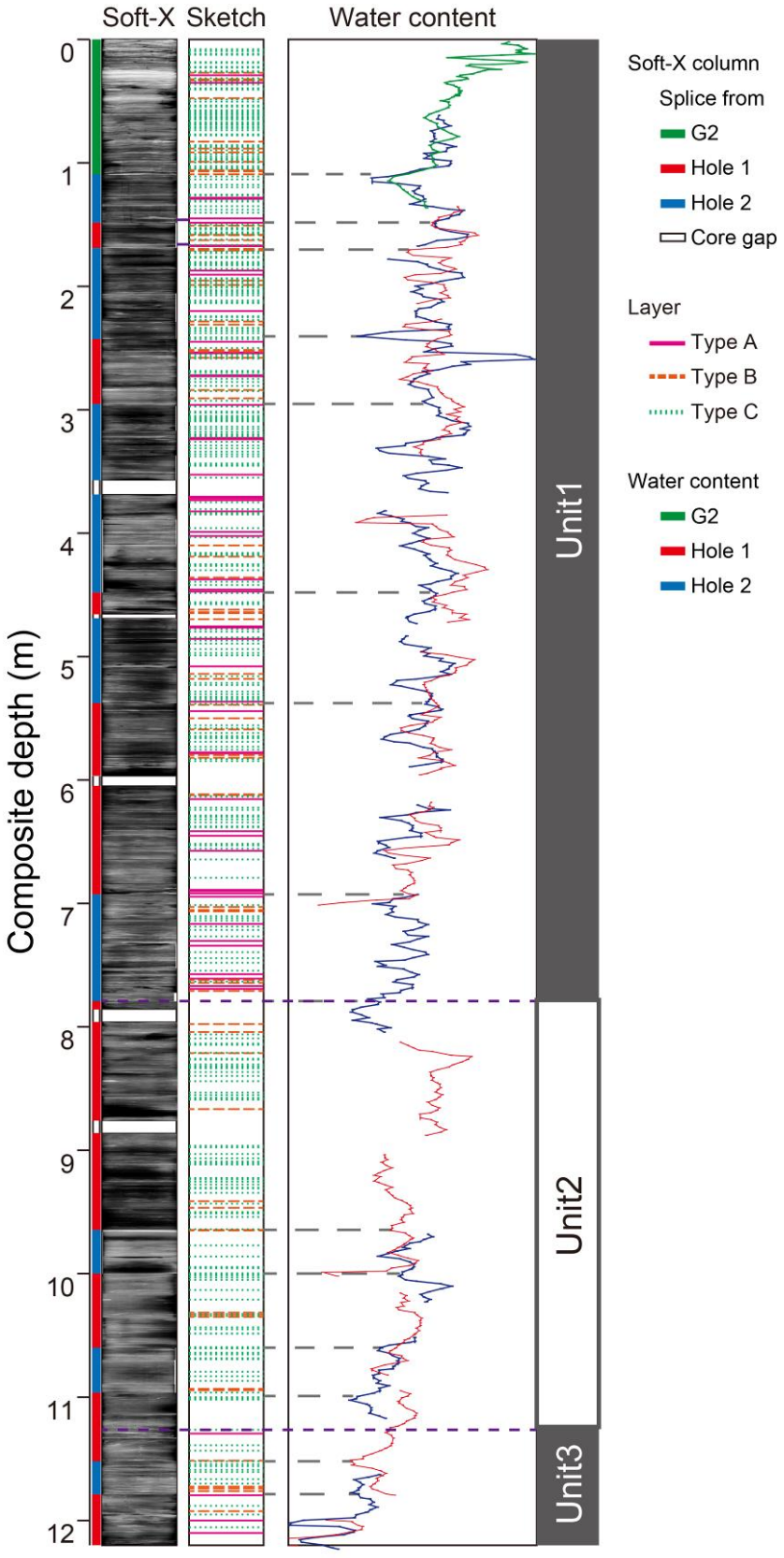

Figure 2.11 Composite column of YD13 sediments.

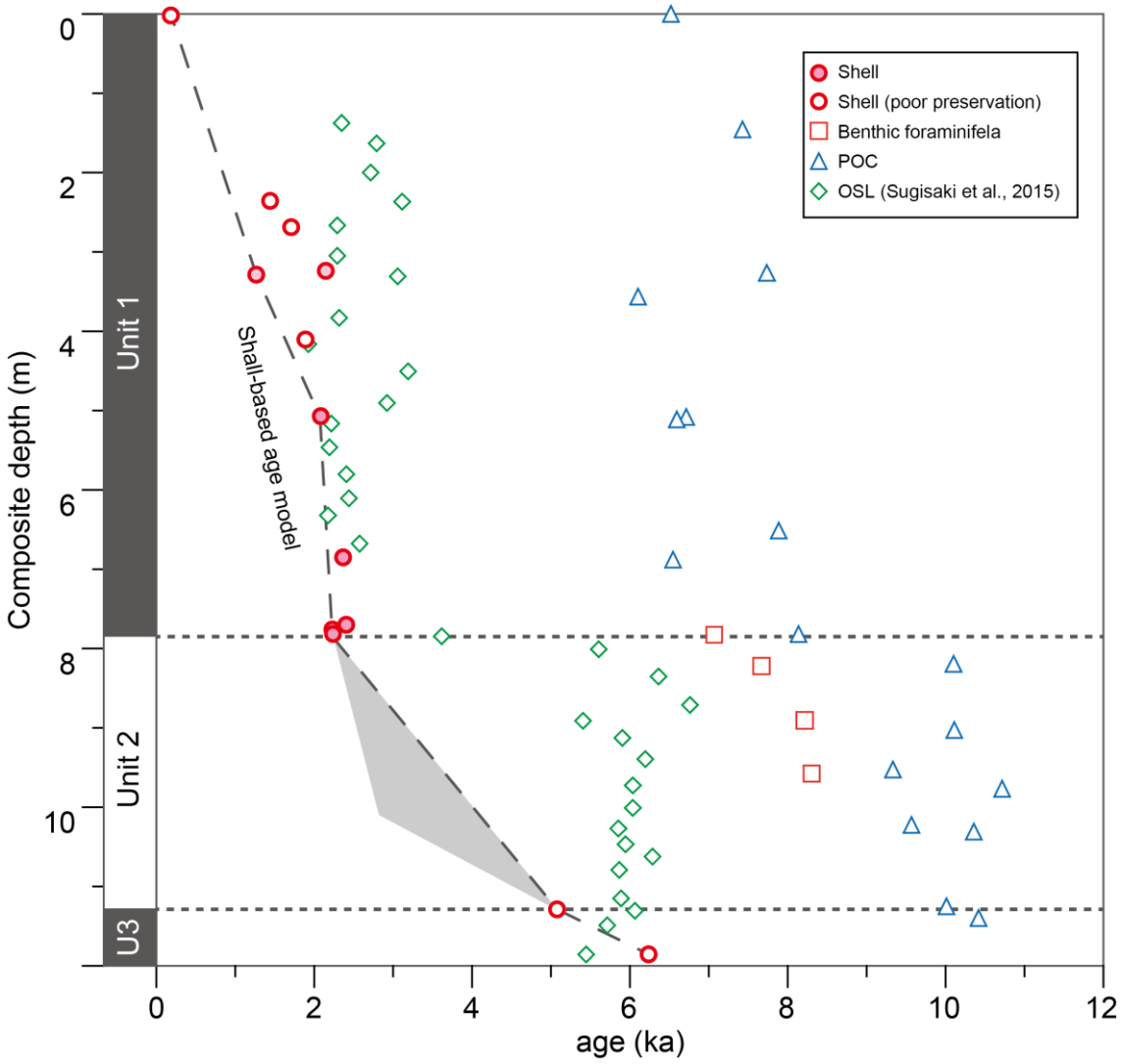

Figure 2.12 Radiocarbon ages of shell fossils, benthic foraminifera, and POC and the shell-based age model of YD13. The grey shade indicates the uncertainness of the shell-based age model in Unit 2.

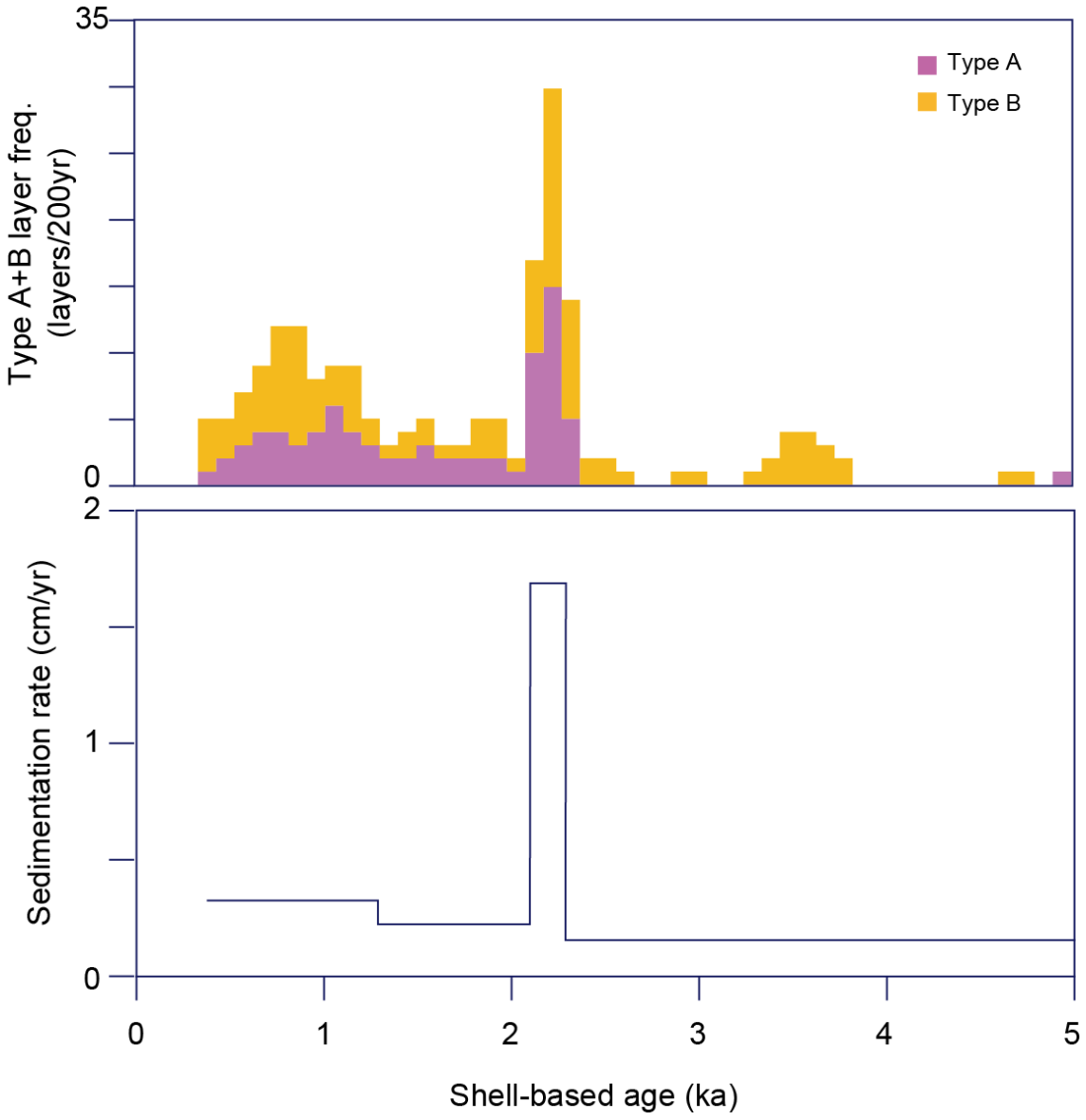

Figure 2.13 (a) Sedimentation rate and (b) frequency of the Type A plus B layers in YD13 sediments during the last 5 ka

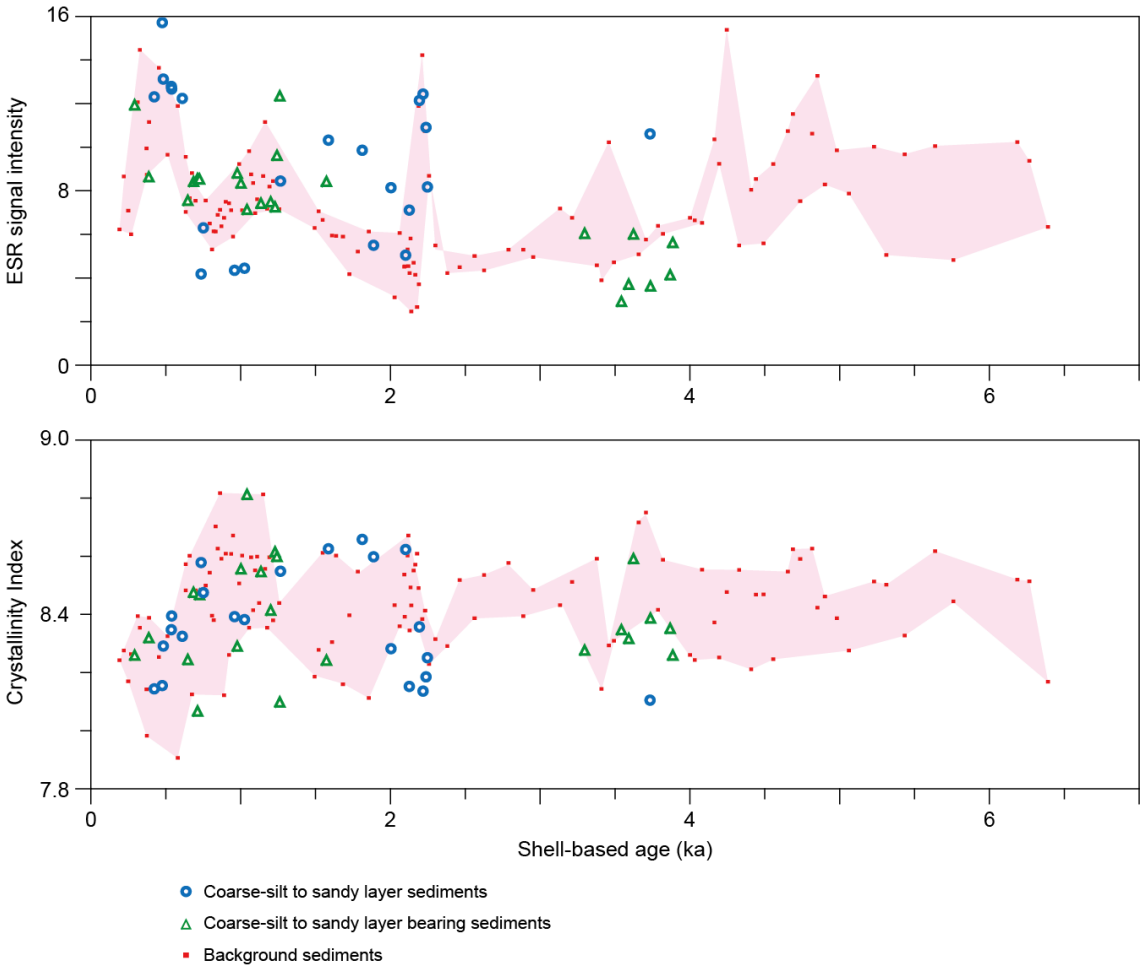

Figure 2.14 (a) ESR signal intensity and (b) CI in YD13 during the last 7 ka. Each sample (2cm interval) are categorized based on whether they include Type A or Type B layers. Samples which are exclusively composed of Type A or Type B layers are categorized as “Coarse-silt to sandy layer sediments”. Samples which include any Type A or Type B layer are categorized as “Coarse-silt to sandy layer bearing sediments”. Samples which do not include neither Type A nor Type B layers are categorized as “Background sediments”.

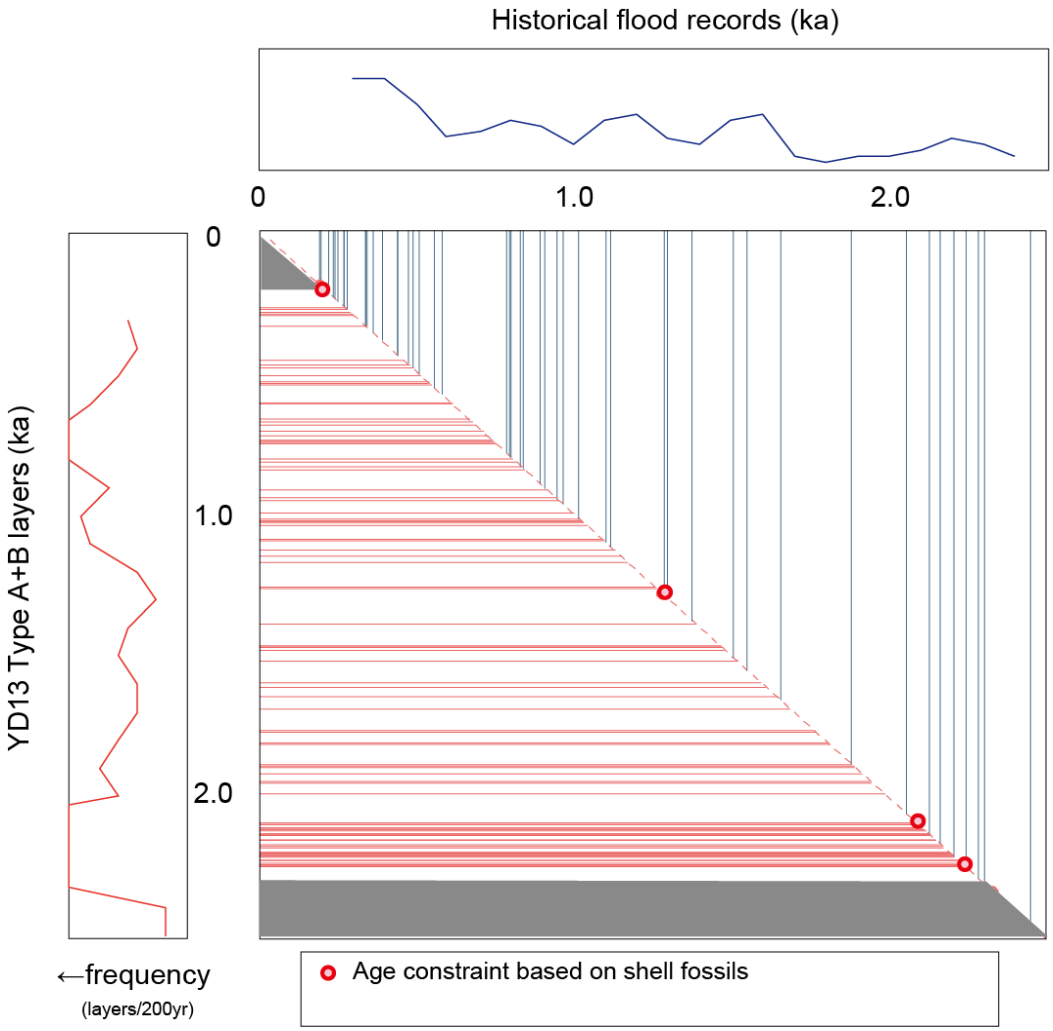

Figure 2.15 Comparison of the historical floods record and the occurrence of the Type A plus Type B layers in Unit1

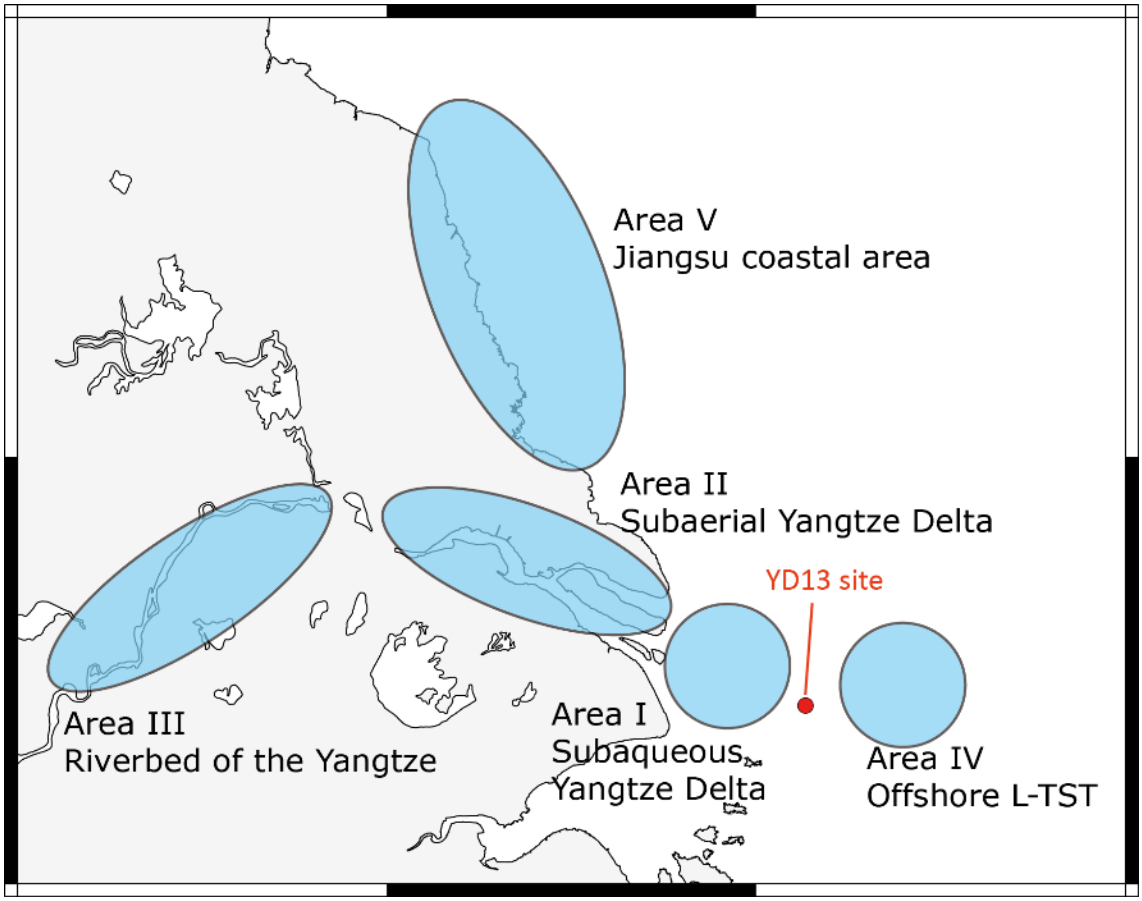

Figure 2.16 Potential origin of the reworked material in Unit 1

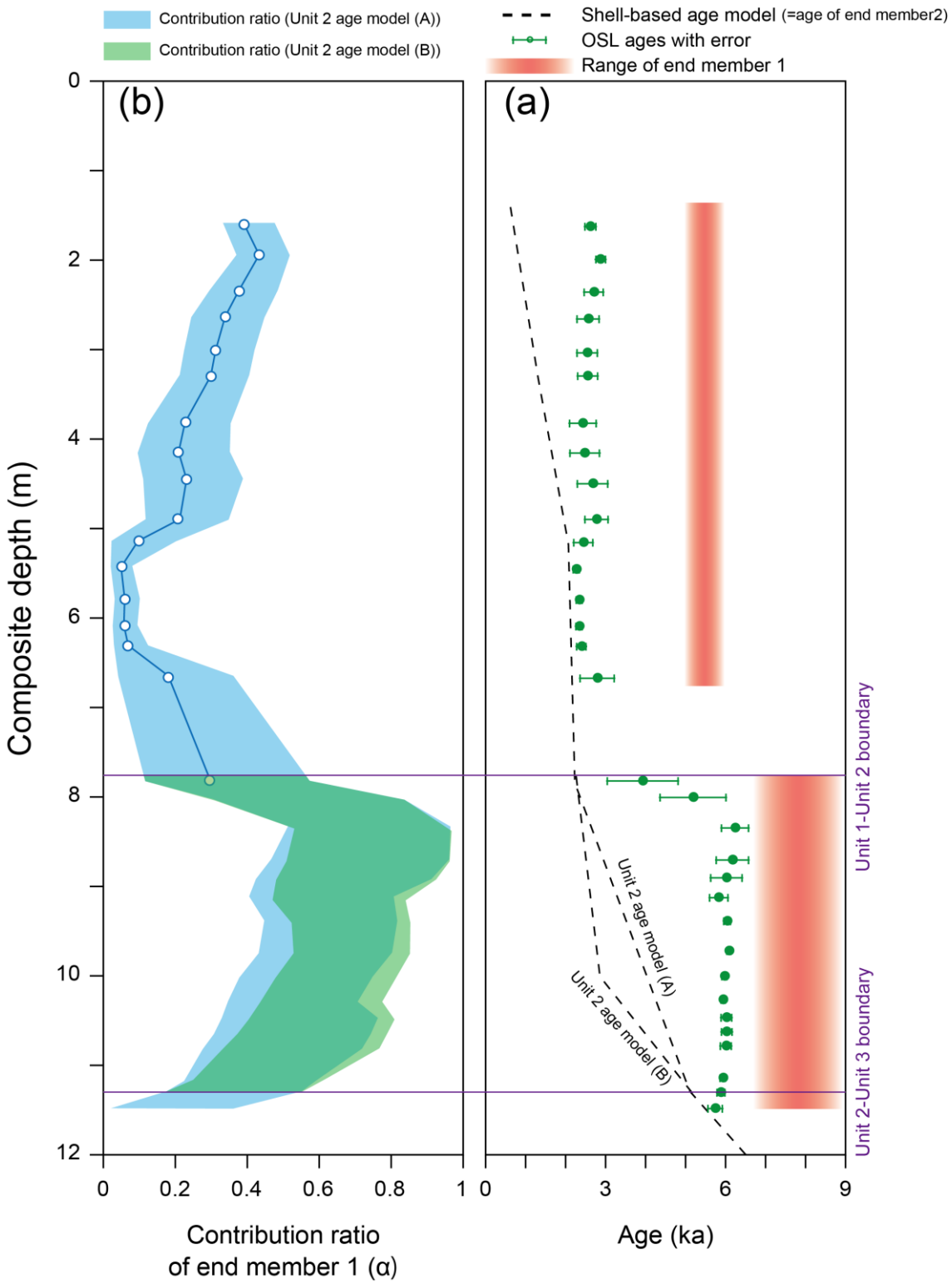

Figure 2.17 (a) Contribution ratio of end member 1 (old end member) in Unit 1 and Unit 2 against the composite depth. (b) The shell-based age model with uncertainness (A and B in Unit2), the OSL ages of quartz, and the ages and uncertainness of the end member 1 against the composite depth.

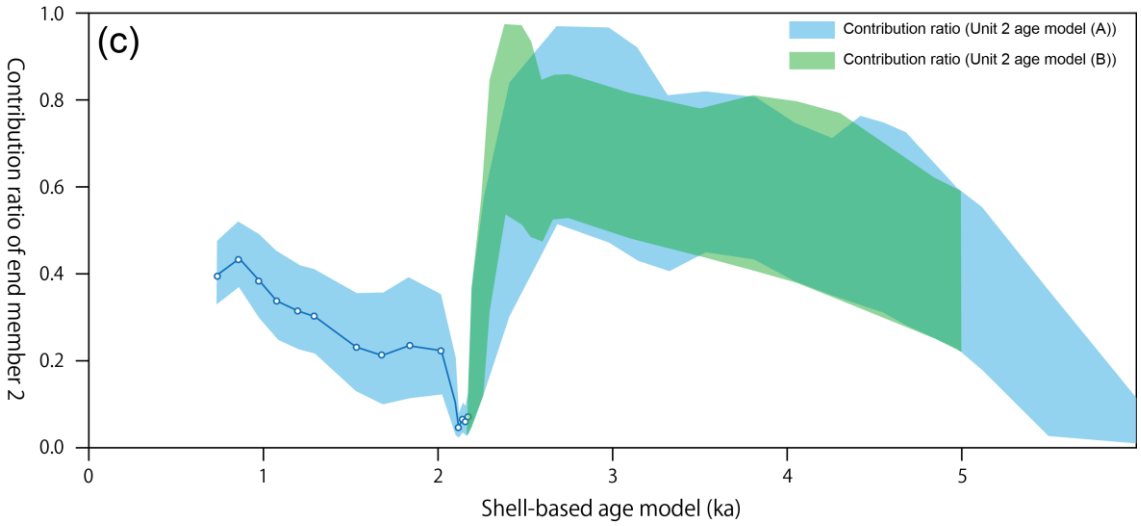

Figure 2.17 (c). Contribution ratio of end member 1 (old end member) in Unit 1 and Unit 2 against the shell-base age model (A) and (B) shown in Figure 2.17 (b).

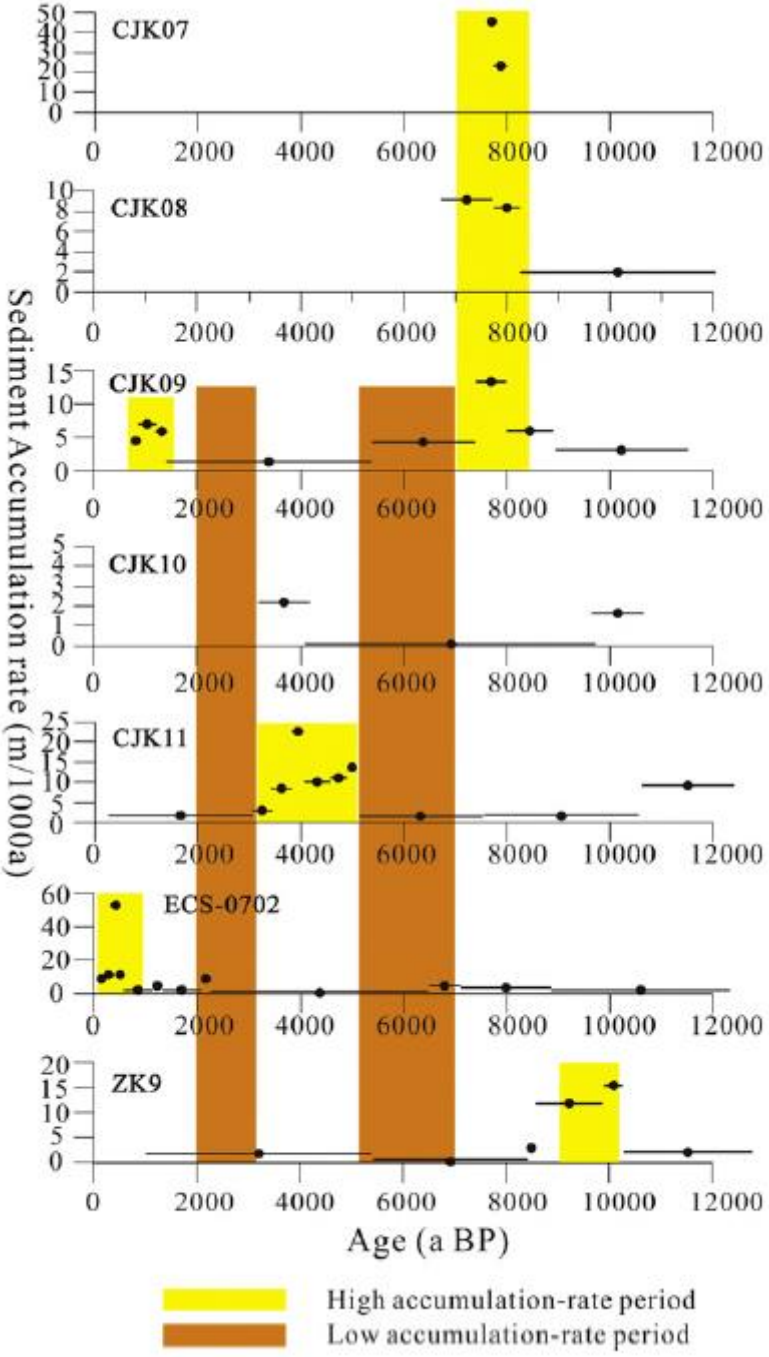

Figure 2.18 Compile of Sedimentation rate of the sediment cores around the subaqueous Yangtze Delta by Xu et al. (2016). The position of each hole are shown in Figure 2.2.

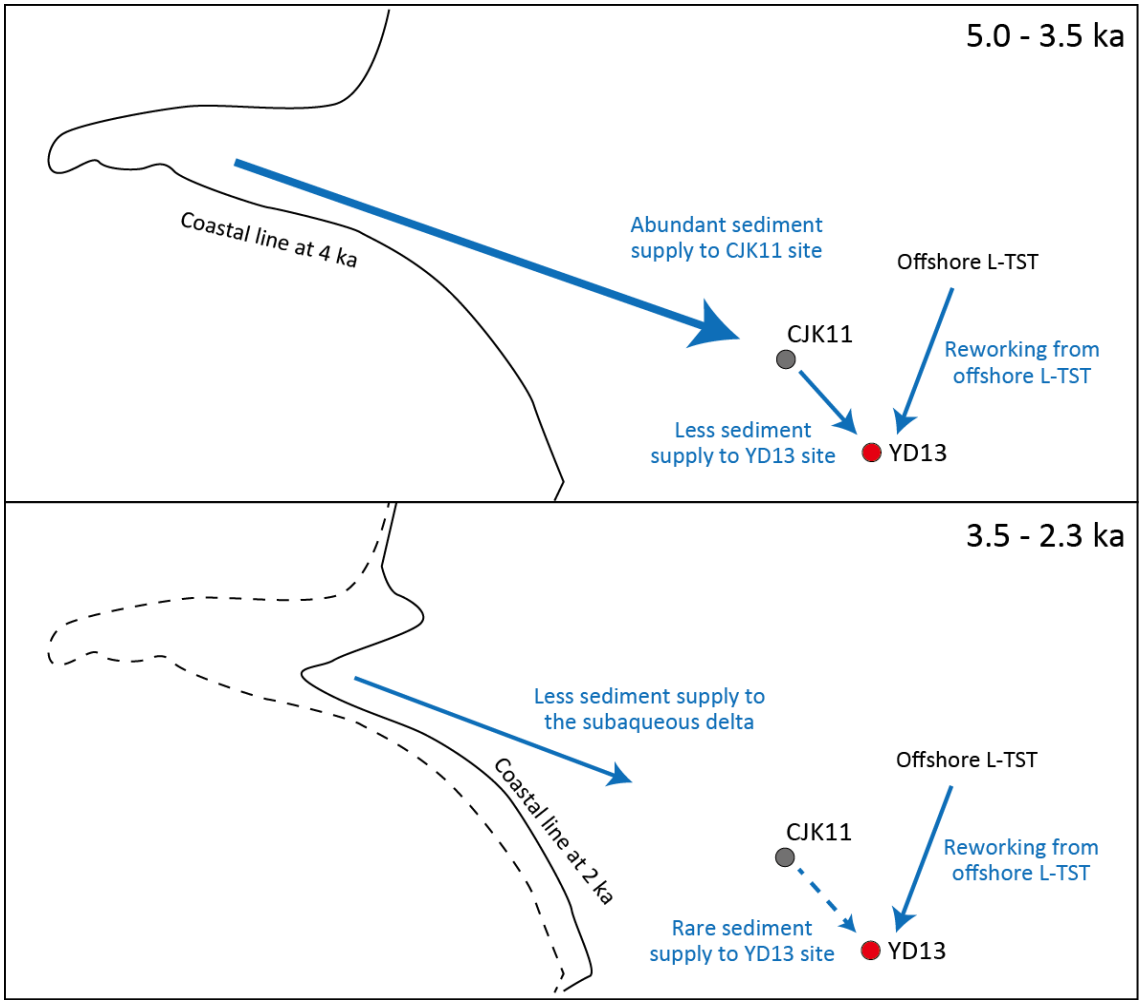

Figure 2.19a
Conceptual schema for the change of the contribution ratio in Unit 2 of YD13

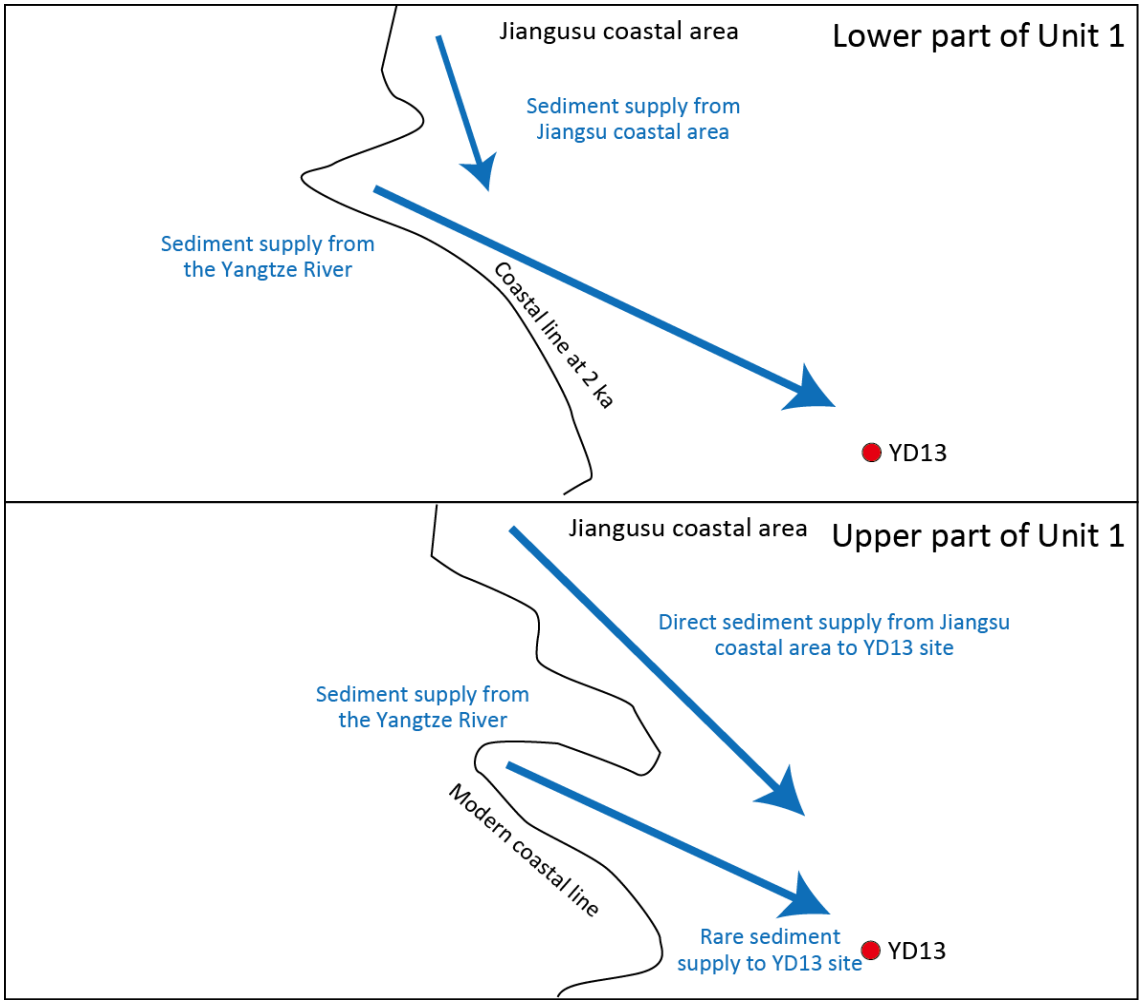

Figure 2.19b
Conceptual schema for the change of the contribution ratio in Unit 1 of YD13

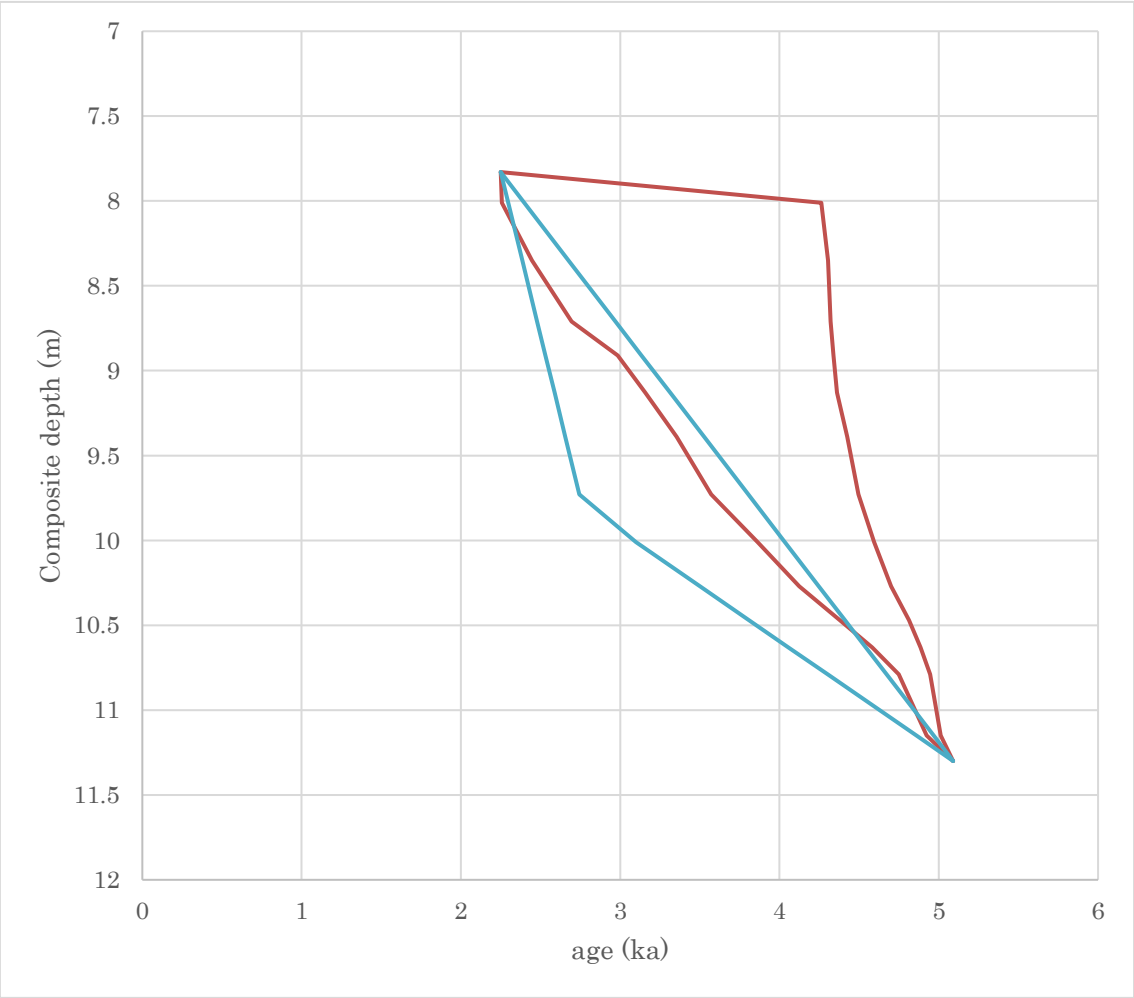

Figure 2.20. Estimated age model based on the reconstructed contribution from the reworked materials. Blue line shows the estimated uncertainness of the age model based on the trend of the sedimentation rate. Red line shows the estimated uncertainness of the age model based on the contribution ratio of the reworked materials. The depositional ages of Unit 2 is estimated as the common range of two age area.

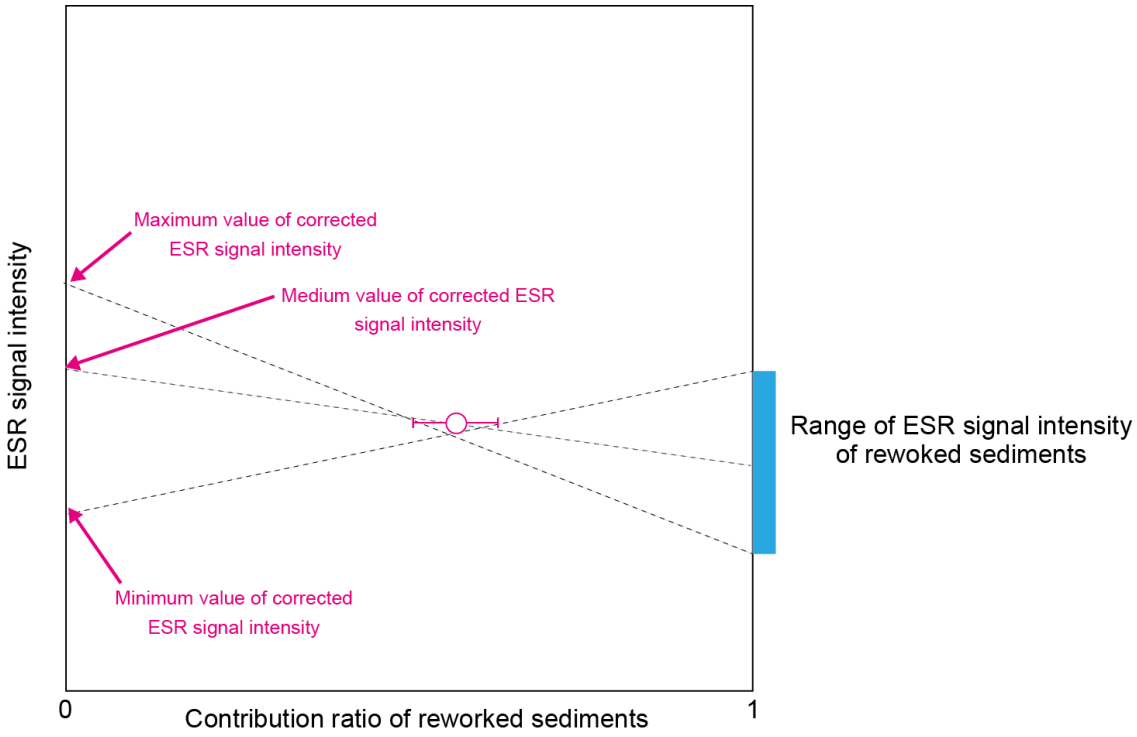

Figure 2.21
Concept for removing the effect of the reworked sediments from the ESR signal intensity of samples in Unit 1 and 2

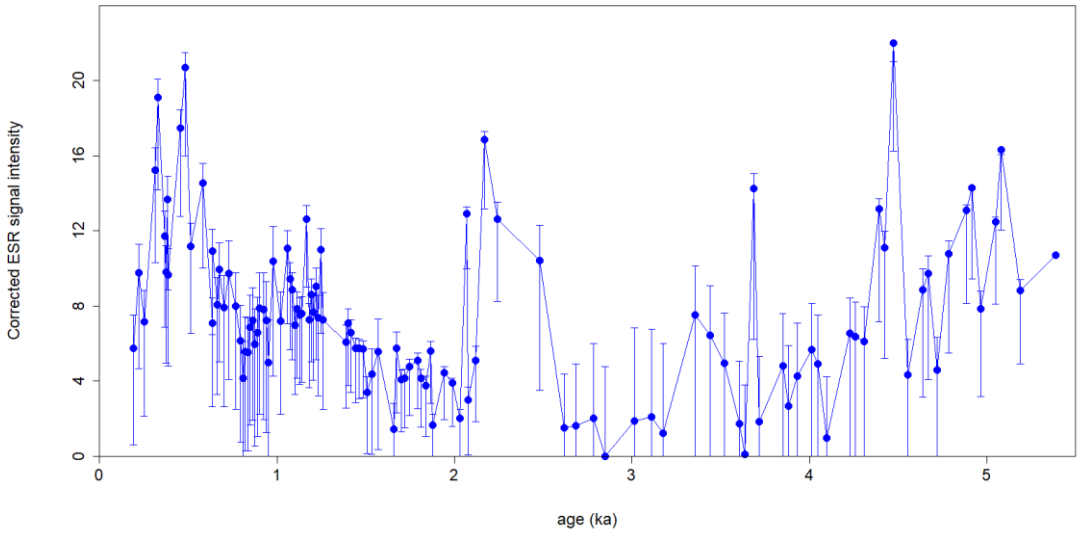

Figure 2.22 (a)
Corrected ESR signal intensity of the background sediments with error during the last 5.5 ka.

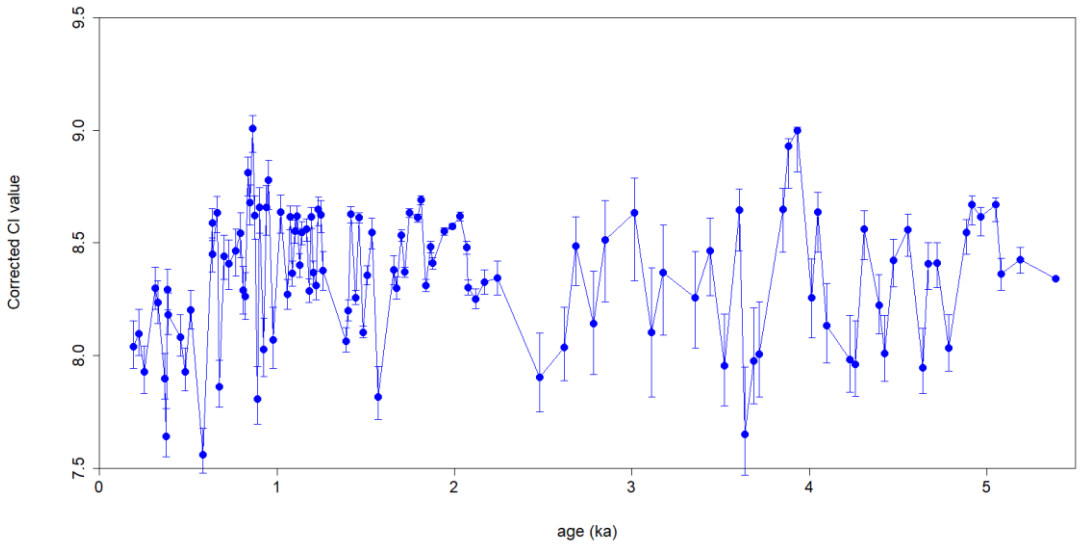

Figure 2.23 (b)
Corrected ESR signal intensity of the background sediments with error during the last 5.5 ka.

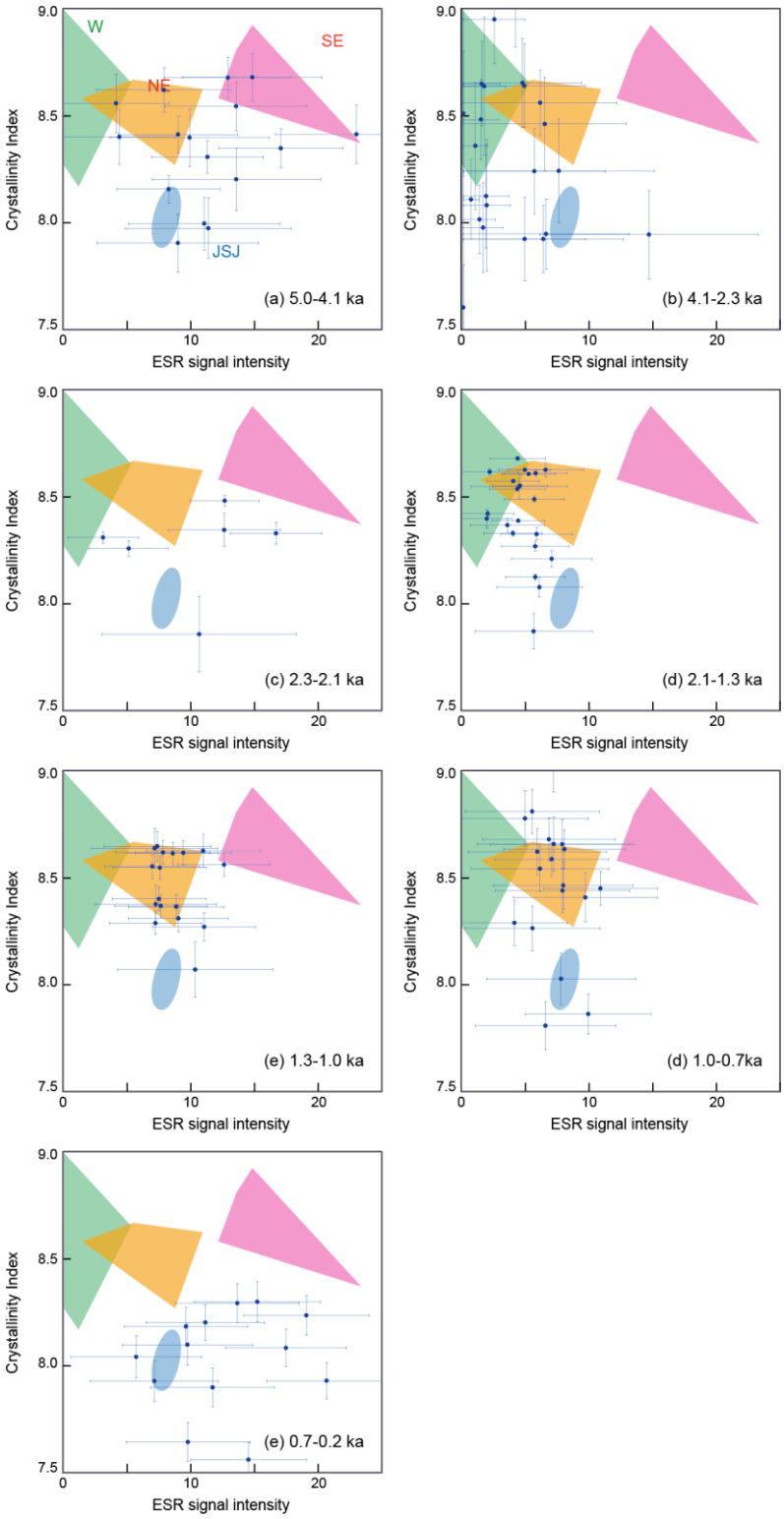

Figure 2.24 Provenance change of quartz in the YD13 sediments during the last 5 ky.

W: Western tributaries; NE: Northeastern tributaries; JSJ: upper Jinshajiang; SE: Southeastern tributaries.

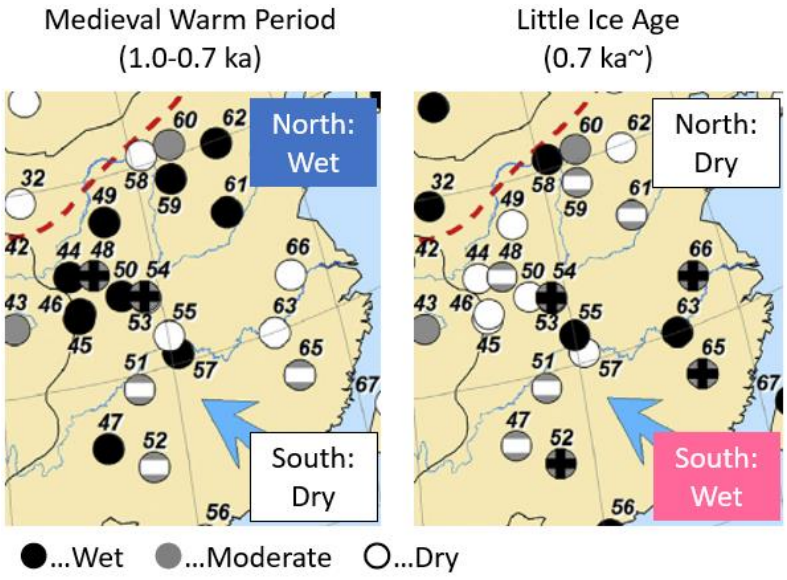

Figure 2.25. Reconstructed wet/dry changes in the eastern Asia during the last 1 ky based on the various paleo-climate indices (after Chen et al., 2015).

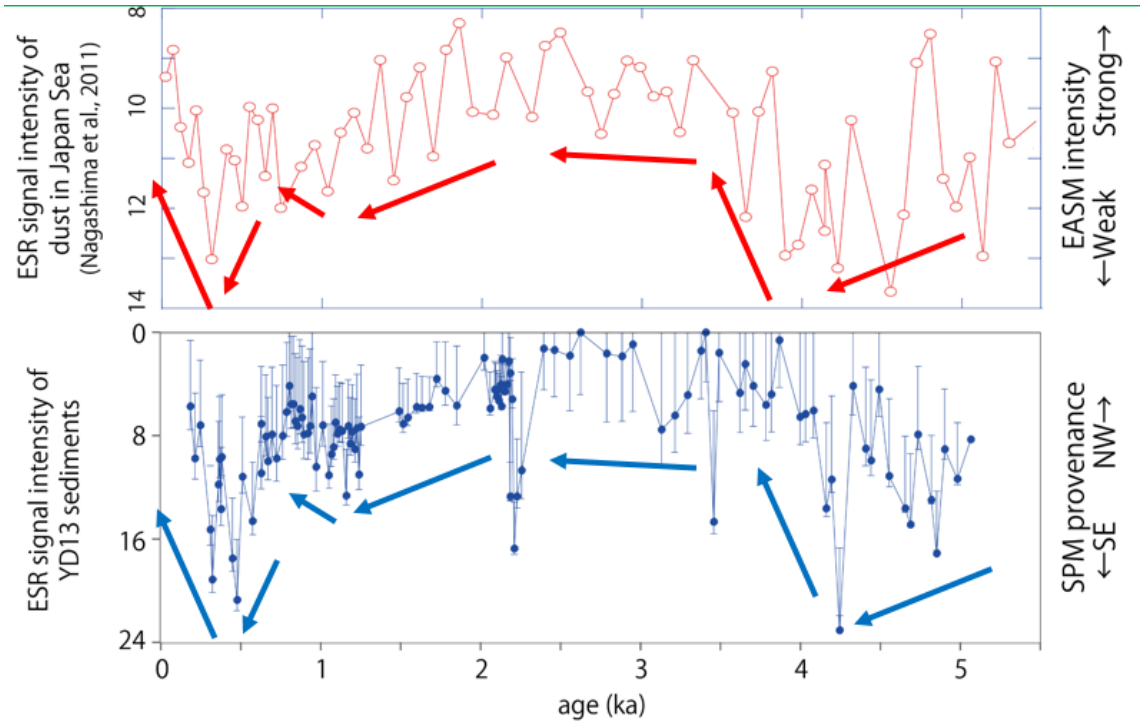

Figure 2.26 Comparison of the EASM intensity reconstructed from the westerly jet movement (Nagashima et al., 2013) and the changes in SPM provenance in the Yangtze River reconstructed from YD13 core in this study.

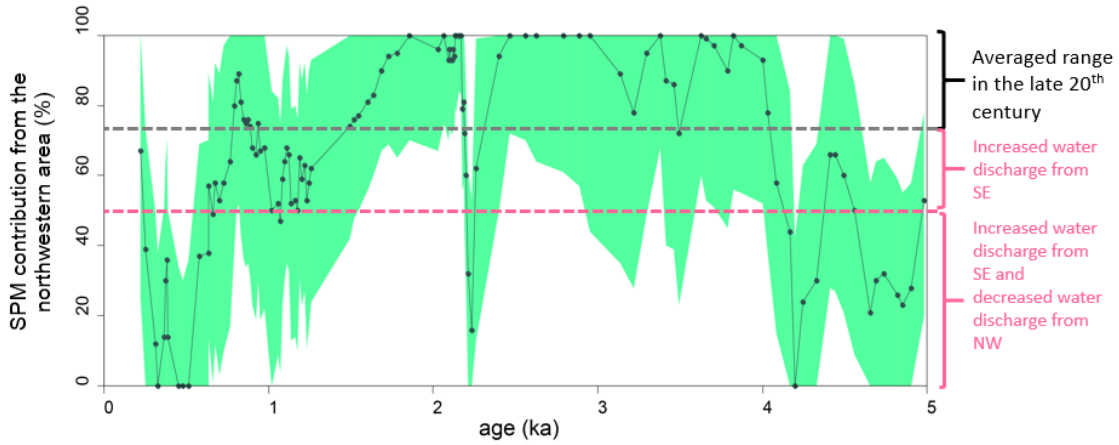

Figure 2.27. Reconstructed contribution from the northwestern area of the Yangtze Basin in the YD13 core during the last 5 ky.

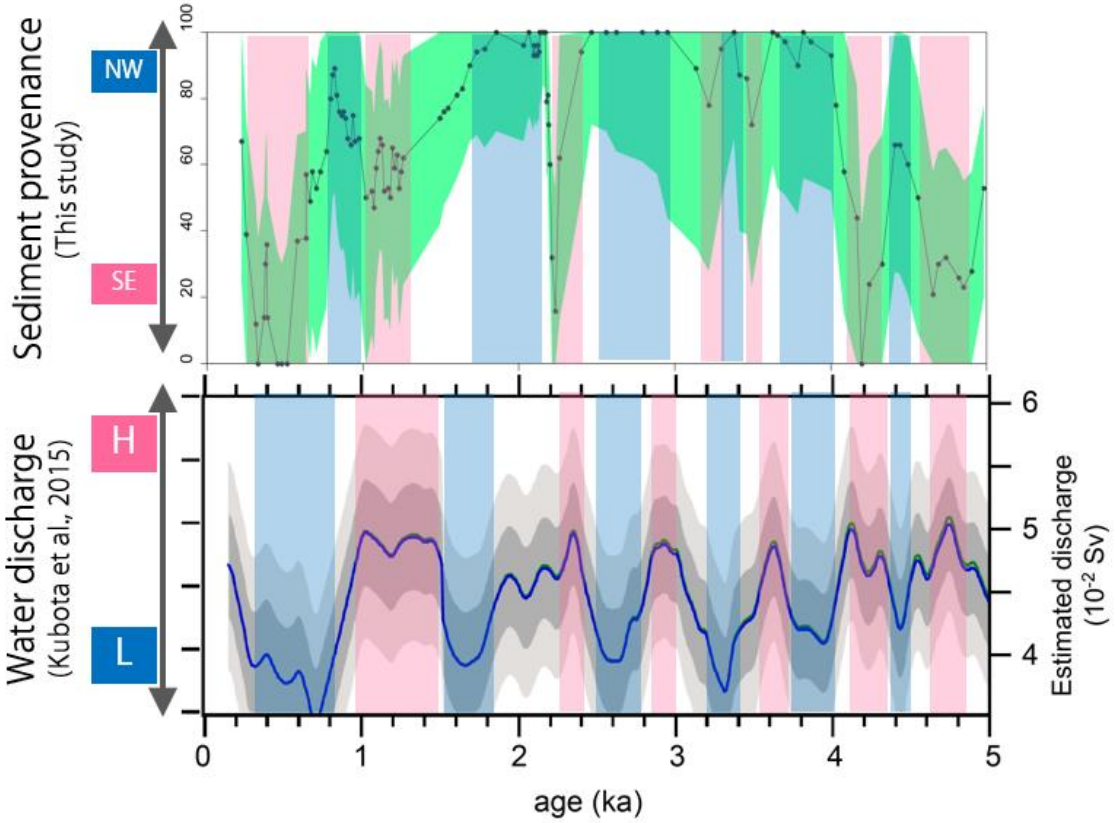

Figure 2.28 (a) Contribution from the northwestern basin during 5.1 ka in YD13 sediments in this study. (b) Estimated water discharge from the Yangtze River by Kubota et al. (2015).

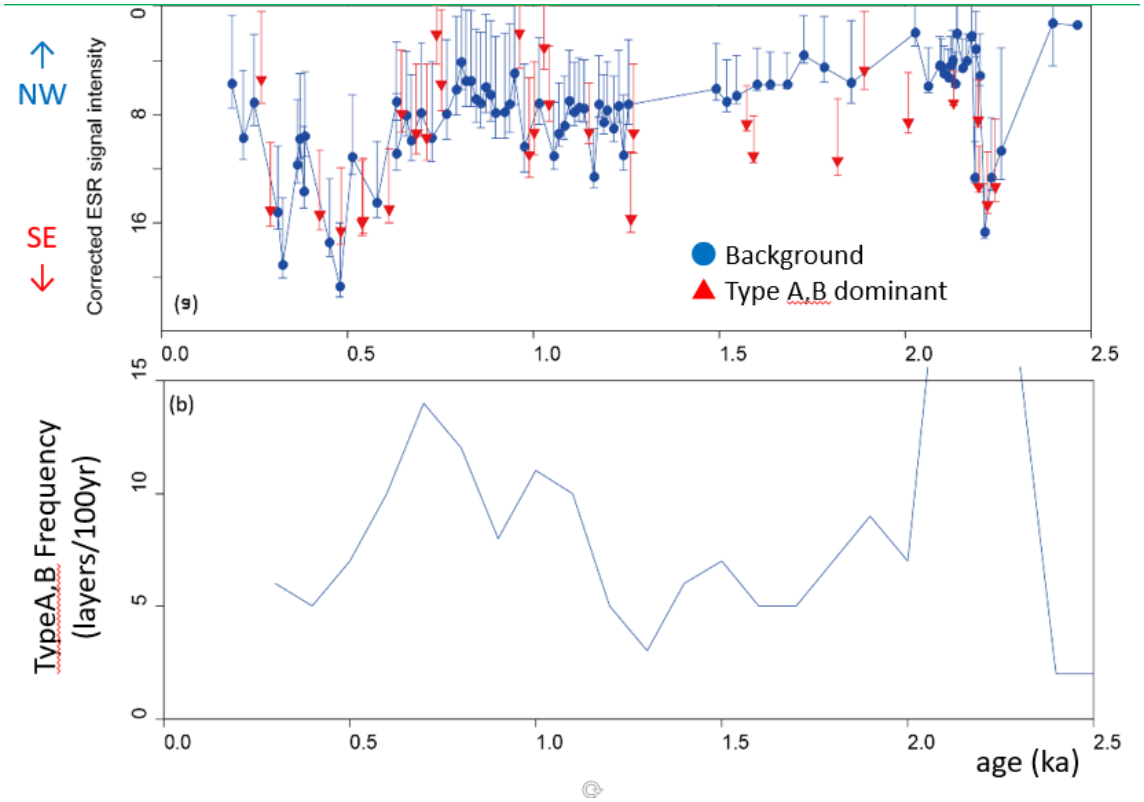

Figure 2.29. (a) ESR signal intensity of the background sediments and the Type A and B dominant sediments. (b) Type A and B layer frequency during the last 2.5 ky.